Studies of DNA Dynamics in Slit-like Nanochannel Confinement

by

Anthony Balducci

B.S. Chemical Engineering, Carnegie-Mellon University (2003),

Submitted to the Department of Chemical Engineering
in partial fulfillment of the requirements for the degree of

Doctor of Philosophy in Chemical Engineering

at the

MASSACHUSETTS INSTITUTE OF TECHNOLOGY

August 2008

Author _____
Department of Chemical Engineering
August 7, 2008

Certified by _____
Patrick S. Doyle
Associate Professor of Chemical Engineering
Thesis Supervisor

Accepted by _____
William M. Deen
Chairman, Department Committee on Graduate Students

Studies of DNA Dynamics in Slit-like Nanochannel Confinement

by
Anthony Balducci

Submitted to the Department of Chemical Engineering
on August 7, 2008, in partial fulfillment of the
requirements for the degree of
Doctor of Philosophy in Chemical Engineering

Abstract

The ability to visually observe single DNA molecules has greatly improved our understanding of polymer physics, from gel electrophoresis to the rheology of dilute (and even concentrated) polymer solutions. The use of DNA in these general studies, though, resulted in a depth of specific knowledge concerning a particular polymer of major interest in biology. Researchers have taken advantage of this wealth of knowledge to develop new, faster, cheaper, and more direct methods of extracting the information, at a coarse level, embedded in the sequence of basepairs along the DNA backbone. Further development, though, is now limited by the ability to control and manipulate the position and conformation of single DNA molecules.

It was recognized long ago that confinement of polymer molecules in geometries with dimensions on the order of the polymer size would greatly affect the physical behavior of that polymer. These physical changes were later hypothesized to be of use to control single molecules of DNA. However, until recently, the confinement theories and their use stood untested due to a lack of techniques to reliably and controllably construct micro- (and nano-) devices with such small feature sizes. It is the focus of this thesis to investigate these confinement effects in an ideal, nanofabricated geometry and their use in the manipulation and control of single DNA molecules.

In this thesis, we present a series of single-molecule visualization studies aimed at elucidating polymer behavior in confinement and methods of possible use in the manipulation and control of the polymer conformation. In particular, confinement in a slit was shown, both experimentally and through scaling analysis, to diminish long length scale polymer-induced solvent flow sufficiently enough to render those effects negligible in the behavior of the confined molecule. We also demonstrate that confinement also alters the diffusion and relaxation time of the DNA, and we compare their dependence on channel height and molecular weight to existing theories. De Gennes' blob theory is found to describe the molecular weight scalings quite well, but predictions of the scalings with channel height are plagued by an oversimplified description of short length scale polymer-solvent interaction used in the theory. Thus, empirical knowledge is needed to adequately predict the scaling of DNA transport coefficients in confinement.

We also investigate aspects of polymer deformation in confinement. We observe, for the first time, two slow modes of polymer relaxation. The two modes are found to govern polymer behavior based on the polymer's extension, a phenomenon unique to confinement in polymer physics. A simple, physical model is developed to explain the origin of the two governing time scales, to explain their scaling with channel height and molecular weight, and to predict the extension at which the exchange between the two timescales occurs. We also examine the effects of these two

characteristic time constants on the steady-state stretch of molecules in confinement. We find that the second-longest relaxation time determines the deformation rate needed to unravel the coil, unlike bulk polymer deformation. Interestingly, details of this unraveling change significantly in confinement, highlighting the need for further work in this area.

In larger channels, we demonstrate that microfabrication techniques in the form of an obstacle array with dimensions smaller than the polymer size can aid polymer stretching. While a polymer will often fold or kink during stretching, we find the use of a collision event to "precondition" the polymer conformation for stretching makes these folds and kinks less likely, and therefore, stretching occur more rapidly. The efficiency of the device depends strongly on the probability of a collision event, and results from single molecule/single post experiments are used to demonstrate the capability of a second-generation device.

The impact of this thesis will be two-fold. Our fundamental results have and will continue to serve as a basis of comparison and a springboard for more complicated studies of confined polymer physics. These studies provide detailed information on DNA transport coefficients in geometries widely utilized in microfabricated devices. We also directly display the effects of confinement on DNA manipulation. Non-equilibrium polymer dynamics are found to be highly nontrivial, exemplified by the importance of a new timescale of polymer motion. Importantly, it is this new timescale that is of concern for applications such as gene mapping where large scale polymer deformation is required. Lastly, we demonstrate the success of a unit-operation-like approach to the design of polymer manipulation devices.

Thesis Supervisor: Patrick S. Doyle
Title: Associate Professor of Chemical Engineering

Acknowledgments

To me, a PhD thesis is primarily a learning experience. There may be research goals, experimental protocols, and other acquisitions along the way, but the primary goal is to become stronger intellectually. It takes significant effort to learn how to think, and it is not something which is easily taught. I have many thanks for Pat for the push that I sometimes very much begrudgingly received, the patience to push me further, and the perseverance to get me to (sometimes) unclutter my head enough to do productive research.

I thank my wife Anna for the support through these five years. She has given more than I could ask for and I cannot express here my gratitude. She has kept me sane, a gift unto itself, by forcing me to focus on the larger and more important issues in both research and outside life alike.

I thank my family for the support and the ability to get away from it all sometimes for weekends at a time. Their understanding has made some of the sacrifices made so much easier. They have kept me grounded with the constant reminder that there is a wealth of knowledge and entire worlds beyond the sheltered one in which I have lived. They have kept me grounded with the constant reminder of how absurd the world in which I exist actually is.

I also must extend my thanks to members of the Doyle group and more generally MIT, without whom this work could not have been completed. Towards the research end: I thank Greg Randall for his time and patience in teaching me all of the tricks and techniques of working with DNA and microscopy; Patrick Underhill for numerous theoretical discussions; Chih-Chen Hsieh for showing me what focus, patience, grace, and an eye for detail really are; Jing Tang for learning the tricks and

techniques, making them better, and his contributions in the design and concept of the cross-slot channel; and Daniel Trahan for making me realize just how much I don't understand. Many thanks to Ramin and Dan for making being cooped up in the basement office not such a bad thing after all. Thank you very much for all of the questions you've asked me, especially Jason, Daniel, Rilla and Panda, which made me think and ponder things I wouldn't have thought about otherwise and lead to discussions form which I learned as much as I may have taught (or at least I'd like to think that I had taught). Thank you very much for your friendships and making the environment around here a great one to work in. A special thanks to Dan P. for numerous discussions and distractions, and especially for being a great sounding board for my hair-brained and whacky ideas, most of which got the completely credible "that can't possibly work" response.

I also thank Mr. Pan Mao for many hours of fabrication and teaching me the fabrication techniques used in this work. Without his hard work, the slit-like nanochannel would not exist. Without his patience and on-call help in the fabrication facility, I would not be able to make them.

Table of Contents

List of Figures

List of Tables

CHAPTER 1

Introduction

1.1 Motivation

1.1.1 Gene mapping

It is well known that the wealth of information required for the day to day, and sometimes the hour by hour, existence of life is embedded in the basepair sequence of DNA molecules contained in each cell. Accordingly, a lot of research has taken place to determine the *sequence* of these basepairs of a representative human (the human genome project) [1] and other mammalian species (monkey, dog, cat, mouse, etc.) [2] to find the active pieces of genetic material. The accumulated knowledge has been extremely beneficial and has had impact on current thinking in terms of similarity between species, evolution, and human migration, and, at a more detailed level, the role of specific sequences of DNA (primers, exons, introns) in the DNA to RNA translation process. In fact, the acquired detailed information of small number of human genetic sequences has highlighted the importance of a less-detailed level of information from a larger population. While sequencing a large number of individuals is technically feasible, time and financial restraints require a coarser view of the genome.

Acquiring this coarser level of information is termed DNA or gene *mapping* where the location of genes (large segements of DNA basepairs with a known function) relative to one another is of interest. This level of information is sufficient for identification, national defense, and some medical applications [3], and, in general, is more useful for individual comparisons than the use of the full sequence. As we will see below, with sufficiently sensitive tags, it may be possible to determine

mutations of single DNA basepairs (SNP's) which are known to be the cause of certain types of cancer and genetic disease.

There are two methods used currently to map DNA. The first and older technology, which is used in the bulk of mapping experiments, is an indirect mapping method. An emerging technology, termed "direct linear analysis" promises faster, cheaper, and perhaps more robust analyses in terms of possible targets than the indirect methods.

Indirect Analysis

Indirect analyses use a two-step approach to mapping DNA. First the DNA is digested with a number of restriction enzymes. These enzymes cut the DNA into fragments depending on the local sequence of DNA. These fragments are then amplified in number. The pieces of DNA are then separated by size, the locations where the enzymes cut along the original DNA backbone are determined, and a "map" of these locations is developed. The difficulty in this procedure lies in the separation, as separations for large DNA are difficult. The details will be explored later, but for now let us simply state that the the free-solution mobility of DNA is independent of the DNA length. Hence, DNA separations require some sort of sieving mechanism, many of which have recently been explored, to add size dependence into the separation mechanism.

The most widely-used method is to electrophorese DNA through a cross-linked polymer gel. There the DNA mobility becomes size dependent as the DNA is forced to reptate through the pores of the gel. This method, while yielding resolutions of a basepair for small DNA molecules, is prohibitively slow for molecules with the larger molecular weights of interest. More recent studies have used DNA electrophoresis through polymer solutions (not gels) where collisions occur between the DNA and polymers to create an "entangled" body, the overall mobility of which is dependent on the length of the DNA [4, 5, 6]. Other studies have used synthetic "parachutes" attached to the DNA to add size dependence [7]. Microfabrication has allowed the construction of "artificial gels" where pores can be controllably constructed in the material in an attempt to replicate the reptation behavior. Early studies [8, 9] using posts to make pores found that the DNA has a tendency to hook around posts, a mechanism which in itself adds size dependence [10, 11, 12, 13]. Studies then investigated the use of posts [14, 15] and post arrays [16, 17] of varying geometries and forms, including field-assembled colloidal structures as separation matrices [18, 19, 20, 21] and mixing ideas from pulsed-field electrophoresis and microfabricated geometries [22]. Studies using confinement have also shown length based separations. Nanochannels have also been used, both straight channels [23] and channels with step changes in cross-section [24, 25, 26], to separate DNA as well. The over-riding theme of this set of research is to create micro and nano structures with a more open framework to allow separation of larger DNA faster, which corresponds to the ability to map genes more quickly. However, increasing the speed of the separation decreases the resolution and limits the overall usefulness of the technique. As we will see, direct analysis bypasses these issues since it does not require a length-based separation.

Direct Analysis

Direct analysis attempts to read off the location of genes relative to one another by directly observing single molecules of DNA. Whereas indirect analysis is by nature a multi-molecular process, direct analysis only uses multiple molecules for statistical purposes. The method relies on an ability

to "tag" specific sequences of DNA, "tag" meaning to make measurably different than neighboring sequences, usually by attaching a fluorescent molecule. There has been significant work using proteins [27] and DNA [28] conjugated to small molecule dyes and the attachment of the complex to different locations on the DNA backbone. Currently, direct analysis is becoming a common tool to "close" genome sequences, that is, put together, in order, all the bits and pieces of information gathered in multiple sequencing experiments [29]. With sufficiently sensitive tags and knowledge of the specific location of the a gene of interest (applicable, say, for the testing of some cancers) it may be possible to determine the presence of a single nucleotide polymorphism (SNP) from the binary on/off position of the tag. The remaining challenge, and the one germane to the current thesis, is to controllably conform the DNA from the otherwise randomly coiled conformation at equilibrium so as to measure the linear distance between tagged locations (or the time elapsed during advection past a detector) to the number of basepairs between the tags. Interest in this technique has inspired investigations into methods of conformation control of single molecules.

Fig. 1.1: *Schematic of the linearization requirement inherent in direct gene mapping methods. "Tags" adsorbed to specific genes are represented by the colored shapes, the order and distance between which is known when the molecule is stretched.*

Direct linear analysis was first described by Schwartz and coworkers [30]. That study stretched DNA in molten agarose using a flow, allowed the agarose to gel and freeze the conformation of DNA, and then observed the specific locations where restriction enzymes cut the DNA. Since that study, a plethora of studies have stretched DNA in a variety of methods. Several studies have tethered the ends of DNA molecules to surfaces and/or beads and used optical tweezers [31, 32], magnetic tweezers [33, 34], flows [35, 36], or electric fields [37, 38] to stretch DNA. While the control over one molecule's extension is very precise, especially in the tweezer experiments, the attachment of a single bead to a single DNA end is time consuming and difficult. Other studies have "combed" (directionally adsorbed) DNA onto a treated [28, 39] or untreated [40, 41] surface using a receding meniscus and observed the location of tags with fluorescence microscopy. While large numbers of DNA can be stretched and attached to a surface in this manner, the throughput of the device becomes very dependent on the scanning rate and the creation of many treated surfaces to analyze multiple samples can be expensive and wasteful. Also, surface defects can become very important in the adsorption process and the amount of stretch incurred has been found to be important to control, as overstretching DNA [42] incurs lower enzymatic (often used in the tagging process) activity [43]. Other investigators have used confinement of DNA in tubular or square nanochannels to extend the DNA into a more linear conformation [44, 45, 46]. While this technique has much promise, the small channels are often difficult and expensive to fabricate as well as very sensitive to surface defects.

Extensional flows and/or fields, created in a contraction [47, 48, 49, 50] or stagnation point devices [51, 52], linearize (stretch) DNA. Here, the extensional forces applied to the polymer chain

by the (flow) fields are opposed by the entropic elasticity of the chain. The involvement of the entropic elasticity roots the problem in fundamental polymer physics, a complication, which, as we will see below, may provide handles to control aspects of the polymer extension. Since the applied fields play the active role in stretching the DNA (i.e. surfaces need not be involved) these devices can be much larger, and therefore cheaper and more robust. Flowing solutions over a detector also simplifies greatly the scale-up problem for higher throughput. Also, the information gleaned about polymer stretching in these devices can be used in a much more general way to provide insight into general polymer behavior in flows.

One important aspect of this behavior is described by a concept known as molecular individualism [53]. While we leave a large portion of the explanation to later chapters, at a very basic level molecular individualism explains the large distribution of polymer behavior as being a result of the randomness of the initial configuration of the polymer. In terms of polymer stretching, where applications dictate a *uniform* end result, molecular individualism presents a unique challenge for high-throughput, flow-through devices.

To summarize the two types of gene mapping: indirect analysis, in essence, uses a size-based separation to extract information from the DNA backbone whereas direct analysis takes a single molecule and "reads" off the information. While indirect analysis has been shown effective, the benefits of direct analysis, being faster in that the number of time-intensive steps in DNA manipulation are reduced, and cheaper are clear. However, in the methods of mapping that provide higher throughput (the dynamic methods), the effectiveness of future devices lies mainly in our ability to understand better and possibly design devices which can alter the fundamental polymer physics.

1.1.2 Fundamental polymer physics in confinement

Microfluidics and micro-mechanical systems have played a large role in recent biological, chemical and pharmaceutical research [54]. The usefulness of microfluidics lies in the small length scales involved in the devices, which, aside from allowing the use of extremely small volumes of expensive samples, make different physical effects important than what we experience on the macroscale. Surface and boundary effects as well as viscous forces become much more important, allowing the use of capillary and electrokinetic forces to drive flows and Stokes' equations to describe those flows. Interactions between the fluid and the surface can effect the performance of devices significantly, and fluxes through surfaces (membranes or channel walls) can create significant flows. More relevant to this thesis, however, is the fact that micro- (and nano-) devices can now be constructed with features and more importantly *dimensions* on the order of the size of a *single molecule* of DNA. Since the trend in microfluidics has basically followed that of silicon computer chip processing, that is ever-decreasing size, the practical use of channels with in this size range is foreseeable.

It has long been theorized that confinement of polymers in geometries with dimensions on the order of and smaller than the typical equilibrium polymer size results in changes to the polymers behavior. This topic will be discussed thoroughly in the following chapters, but naively we can expect the shape of the polymer to change. We can also naively extend the results of studies performed with colloids to hypothesize that the polymer dynamics will slow down in confinement. However, the fact that polymers can change their shape (with incurred increases in free energy) complicates matters, especially when one considers polymer deformation in confinement. While theory has provided us with guides for the dependence of changes in diffusivity, relaxation time and polymer size with increases in confinement; no complete and/or direct test of these theories was

performed prior to the work presented here. This knowledge, due to its generality and applicability to practical sizes of DNA and channels used in microfluidic processing, will be important for design of future devices. Specifically, knowledge of fundamental polymer physics may aid future studies dealing with the problem of DNA stretching, or even simply flowing, in confinement.

1.2 Objectives and Overview of Results

The goal of the following research is to develop a sound fundamental foundation for the use of confinement in DNA lab-on-chip processing. As such, we will focus on the dynamics of DNA molecules in slit confinement in particular, both when the DNA molecule is at equilibrium and when its conformation has been significantly perturbed. We also investigate the use of microfabrication to ameliorate the molecular individualism effect.

With the above in mind, this thesis will present the following progression of experiments:

- Investigation of polymer physics at equilibrium in slit confinement
- Investigation of polymer relaxation and deformation in slit confinement
- Investigation of preconformation by microfabricated geometries

In chapter 2 we present a background of unconfined polymer physics, polymer deformation, confinement theories, and electrokinetic theory to provide the foundation upon which we build our experimental results. Chapter 3 details experimental results of diffusion in confinement. The focus in this chapter is a proof, both mathematical (at a scaling level) and experimental, that hydrodynamic interactions do not affect large-scale polymer behavior in confinement. Chapter 4 presents the results of a consecutive experiment incorporating experimental advances to allow the investigation of the polymer relaxation time τ, the diffusivity D, and the size of the molecule R_g with channel height and molecular weight. Here, a complete comparison to standing confinement theory is provided, and detailed information on the small length scale hydrodynamic interactions is extracted. Chapter 5 presents the first detailed experimental results of the effects of confinement on a chain relaxing form an extended state to equilibrium. Two slow modes of relaxation, not only one as in bulk, are found to be active in different extension regimes. Chapter 6 investigates the converse problem: polymer stretching and deformation in confinement. Chapter 7 investigates the dynamics of polymer electrophoresis and stretching in a microfabricated device incorporating a "preconditioning" step to make the initial polymer conformation more uniform, and therefore allow a more uniform polymer stretching. Chapter 8 presents commentary of the effects of this research on the field, as well as future directions for research concerning deformation and confinement.

CHAPTER 2

Background Science

The goal of this chapter is to familiarize the reader with several concepts that are explored and/or extended later in this thesis. Specifically, we will introduce:

- 2.1 The chemistry of the DNA molecule and our point of view of DNA as a model for semi-flexible polymers
- 2.2 Modeling polymers and their shape at equilibrium
- 2.3 Modeling polymers and how they move at equilibrium
- 2.4 Introduction to pertinent confinement theories
- 2.5 Electrokinetic effects (moving DNA with electric fields)

2.1 DNA is a Polymer

A polymer, by general definition, is a molecule made up of a smaller chemical repeat unit. DNA, therefore, being entirely made up of the four nucleotides (Adenosine, Cytosine, Guanine, and Tyrosine; A, C, G, and T) is a polymer. While the fact that these nucleotides have a sequence along the molecule makes DNA very interesting from a biological point of view, we view DNA in terms of physical properties that are for the most part not affected by the particular sequence.

This duality of DNA as a molecule of major interest and as a model physical polymer allow us to extract both pertinent information concerning DNA stretching and mapping in particular, but also information concerning polymer physics in general, from a single experiment.

The chemical structure of DNA is unique among synthetic polymers. Each double-stranded DNA is actually two distinct polymers wrapped around one another in the famous double helix, each nucleotide base in one strand pairing with (hydrogen bonding to) a corresponding base (A to T and G to C) in the other strand (hence the term "basepairs"=[bp]). The doubling of polymer backbones significantly increases the stiffness of the DNA relative to industrial polymers. This stiffness is characterized by the persistence length, a characteristic length scale over which the polymer appears to be locally straight, which varies from O(nm) for industrial polymers like polystyrene to O(100nm) for DNA. As discussed below, an increased persistence length corresponds to a larger random coil size ($R_{g,bulk}$, discussed below). For DNA, this coil size is large enough to be routinely observable with optical microscopy, but the DNA is small enough to exhibit significant thermal motion. Also, since DNA molecules are made by organisms to carry information, each DNA molecule made by the same organism contains the same number of basepairs. The contour length (L_c) (and therefore molecular weight (M_w), since DNA is linear) consistency is important in our studies since we are particularly interested in the effects of molecular weight on the polymer behavior. We should also note here that DNA is strongly charged: each basepair can carry a negative charge. However, for reasons we will encounter below, in the highly salted buffers (and natural environment of DNA), the electrostatic potential due to these charges decays over very small length scales and does not significantly contribute to the stiffness or dynamics of the DNA. However, the fact that DNA is charged provides us with "handles" for transport and stretching of single molecules with electric fields.

The following sections will give a more quantitative description of polymer shape and dynamical behavior.

2.2 Polymer Equilibrium Conformation

In this section we will focus on the equilibrium conformation of linear polymers. In essence, we aim to find how the information about the small length scale conformations induced by the chemical structure effects the large length scale size of the molecule. We consider here a single polymer in a sea of solvent. The focus of this section is to describe and/or derive the length scales of the polymer important at equilibrium, namely the polymer persistence length, contour length, equilibrium coil size, and equilibrium end to end distance.

2.2.1 The ideal polymer conformation

The analysis below follows closely that of Rubenstein and Colby [55] chapters 2 and 3, and Flory [56] chapters 1 through 4. The simplest model of a polymer is a series of $n-1$ rigid rods (modeling the chemical bonds) connected at joints in which we incorporate information about the chemistry. Moreover, for now we assume that the polymer does not self-interact, that is rods and joints can pass through one another. If we let the bond vector starting at atom i and going to atom $i+1$ be $\boldsymbol{r}_i$, then the end-to-end vector of the chain is given by

$$\boldsymbol{R} = \sum_{i=1}^{n} \boldsymbol{r}_i. \tag{2.1}$$

The first moment of the end-to-end vector is related to the isotropy of the polymer. Since there is no source of anisotropy (i.e. correlations between bonds or forces on the polymer), $\langle \boldsymbol{R} \rangle = \mathbf{0}$. However, the second moment gives us some indication of the average dimension of the polymer coil. We can write this second moment as:

$$\langle R^2 \rangle = \langle \boldsymbol{R} \cdot \boldsymbol{R} \rangle = \left\langle \left(\sum_{i=1}^{n} \boldsymbol{r}_i \right) \cdot \left(\sum_{j=1}^{n} \boldsymbol{r}_j \right) \right\rangle = \sum_{i=1}^{n} \sum_{j=1}^{n} \langle \boldsymbol{r}_i \cdot \boldsymbol{r}_j \rangle = l^2 \sum_{i=1}^{n} \sum_{j=1}^{n} \langle \cos \theta_{ij} \rangle \tag{2.2}$$

where $l = |r_i|$ and θ_{ij} is the angle between bonds i and j. We now use relations of the angles between successive segments along the backbone to incorporate information about the small-scale chemical structure.

For instance, if we are dealing with a very flexible polymer where there is no relation between even successive bonds (which is aphysical) along the backbone, then $\cos \theta_{ij} = \delta_{ij}$ where δ_{ij} is the Kronicker delta. The resulting squared end-to-end distance is

$$\langle R^2 \rangle = nl^2. \tag{2.3}$$

Note the dependence on the molecular weight (through n) and the characteristic bond length l is the same as for a random walk (RW) with step size l and number of steps n.

Now, we assume that the angle between successive bonds is fixed in one dimension, but the $i+1^{th}$ bond is allowed to rotate along the i^{th} bond axis. Now there are strong correlations between adjacent bonds, but these correlations decay as the distance between bonds grows.

$$(cos\theta)^{|i-j|} = exp\left\{ |i-j| \ln (\cos \theta) \right\} = exp\left\{ -\frac{|i-j|}{s_p} \right\} \tag{2.4}$$

where

$$s_p = -\frac{1}{\ln \cos \theta} \tag{2.5}$$

is the characteristic number of segments that the chain persists in one direction. Therefore, the persistence length introduced above can be written as $L_p = ls_p$.

We write Equation 2.2 as

$$\sum_{i=1}^{n} \sum_{j=1}^{n} \langle \boldsymbol{r}_i \cdot \boldsymbol{r}_j \rangle = \sum_{i=1}^{n} \sum_{j=1}^{n} \left[r_i^2 \delta_{ij} + l^2 \left(cos\theta \right)^{|i-j|} \left(1 - \delta_{ij} \right) \right] \tag{2.6}$$

and we note that the correlations between bond vectors embodied in the second term act to increase the size of the chain. Due to the exponential decay of the correlations between angles, we can approximate the second term in equation 2.6 as $2n\frac{cos\theta}{1-cos\theta}$ and the average squared end to end distance becomes

$$\langle R^2 \rangle = nl^2 \frac{1 + \cos \theta}{1 - \cos \theta} \tag{2.7}$$

The dependence on n and l is retained, and the coil size increases simply by a factor known as the Flory characteristic ratio

$$C_\infty = \frac{1+\cos\theta}{1-\cos\theta}. \tag{2.8}$$

In fact, it can be shown for any "short range" interaction, that is, one that dies out with distance along the chain so that the sums in equation 2.6 converge, the effect on the end to end distance of the chain is simply to increase by a constant. It is convenient, then, to rescale the chain in terms of N "effective" (Kuhn) monomers of length b such that the end to end distance can be written as $\langle R^2\rangle = Nb^2$ for any flexible polymer. We note that the contour length (the total length of the polymer) is constant $L_c = Nb$. We can then write

$$N = \frac{L_c^2}{C_\infty n l^2} \tag{2.9}$$

$$b = \frac{C_\infty n l^2}{L_c} \tag{2.10}$$

such that

$$\langle R^2\rangle = Nb^2 \tag{2.11}$$

provided the chain is large enough and the chemical structure and effects are taken into account in the Kuhn monomer. The above is an example of coarse graining, that is, focusing on larger length scale effects (here the size of the chain) by accounting for smaller length scale effects (here the chemical structure) by grouping them into digestible (and mathematically feasible) chunks.

DNA, however, is not a flexible polymer due to the fact that there are two polymer backbones which add a considerable degree of stiffness. As such, we model such stiff polymers with a very small bond angle $\cos\theta \approx 1 - \frac{\theta^2}{2}$ and the persistence length becomes

$$L_p = l s_p = -l\frac{1}{\ln(\cos\theta)} \approx l\frac{2}{\theta^2} \tag{2.12}$$

where the approximation $\ln(1-x) \approx -x$ for x small was used. Using equation 2.8, the Flory ratio is

$$C_\infty = \frac{1+\cos\theta}{1-\cos\theta} \approx \frac{4}{\theta^2} \tag{2.13}$$

and the Kuhn length is then

$$b = \frac{C_\infty n l^2}{nl\cos(\theta/2)} \approx l\frac{4}{\theta^2} = 2L_p \tag{2.14}$$

twice the persistence length. The worm-like chain (WLC) model is defined at the limit of $l \to 0$ and $\theta \to 0$ at constant L_p and L_c. At this limit, one can imagine the polymer chain to be a continuous rod with a bending potential (the starting point for statistical mechanical models of stiff polymers).

Moving to this continuous limit, the squared end to end distance of the WLC can be written as

$$\langle R^2\rangle = \int_0^{L_c}\int_0^{L_c} exp\left(-\frac{|i-j|l}{L_p}\right) di\, dj = 2L_pL_c - 2L_p^2\left(1 - exp\left(-\frac{L_c}{L_p}\right)\right) \tag{2.15}$$

In the limit of long chains relative to the persistence length (applicable to the work presented here), the first term dominates and we are left with $\langle R^2 \rangle \approx 2L_pL_c = bL_c = Nb^2$ and we recover the flexible chain scalings.

We should note here that most experimental methods cannot distinguish the ends of the chain from the many chemically identical interior monomers. Even with the ability to visualize a single polymer, the ends of the chain cannot be discerned from the random coil of the polymer. Therefore, it would be beneficial to describe a parameter that quantifies the "cloud" of monomers visible to most experimental techniques. The radius of gyration $R_{g,bulk}$ (we use the subscript "bulk" to denote that the chain is outside of any confining geometry; we will drop the subscript when the polymer is confined in channels) is defined as as the first moment of the distribution of monomers around its center of mass, a characteristic size of the monomer "cloud." The center of mass of the polymer is simply the average location of all the monomers in the chain

$$\boldsymbol{R}_{com} = \frac{1}{N}\sum_{j=1}^{N} \boldsymbol{R}_j \tag{2.16}$$

where $\boldsymbol{R}_i$ is the position of the i^{th} Kuhn monomer. The radius of gyration is given by

$$R_{g,bulk}^2 = \frac{1}{N}\sum_{i=1}^{N}(\boldsymbol{R}_i - \boldsymbol{R}_{com})^2 = \frac{1}{N^2}\sum_{i=1}^{N}\sum_{j=1}^{N}\langle(\boldsymbol{R}_i - \boldsymbol{R}_j)^2\rangle = \frac{\langle R^2\rangle}{6}. \tag{2.17}$$

Thus, the radius of gyration and the end to end distance of a linear chain are proportional.

By analogy with a random walk, we can extract the probability of finding the end to end vector at a position $\boldsymbol{R}$:

$$P(N, \boldsymbol{R}) = \left(\frac{3}{2\pi N b^2}\right) exp\left(-\frac{3\boldsymbol{R}^2}{2Nb^2}\right) \tag{2.18}$$

The probability distribution function gives us information as to how many configurations of the chain have a certain end to end distance, therefore giving information about the dependence of the entropy ($S = k_b \ln \Omega$, k_b is Boltzmann's constant and Ω the number of states available to the system) of the chain as a function of end to end distance. The free energy of the system is then $A(N, \boldsymbol{R}) = U(N, \boldsymbol{R}) + TS(N, \boldsymbol{R})$ where U is the internal energy of an ideal chain. Since we, for now, neglect monomer/monomer interactions (i.e. monomers do not feel one another and can pass through one another) U cannot depend on the individual equilibrium conformation of the polymer (i.e. $U = \Im(N)$ only). The only $\boldsymbol{R}$ dependence in the free energy term, then, originated from the exponential term in the probability distribution function.

$$A(N, \boldsymbol{R}) = \frac{3}{2}k_bT\frac{\boldsymbol{R}^2}{Nb^2} + A_0(N) \tag{2.19}$$

The force required to perturb the end to end vector from equilibrium is then calculated as the derivative of the free energy with respect to the end to end distance:

$$\boldsymbol{f} = \frac{\partial A(N, \boldsymbol{R})}{\partial R} = \frac{3k_bT}{Nb^2}\boldsymbol{R}. \tag{2.20}$$

The force-extension behavior near equilibrium, then, for any polymer that can be modeled accu-

rately with a Kuhn segment, is Hookean with a spring constant

$$\kappa_H = \frac{3k_bT}{Nb^2}. \tag{2.21}$$

We stress that this linear force extension regime is strictly valid only very near equilibrium. Recent experiments using DNA molecules either tethered to beads and stretched or allowed to relax freely in solution have found that this linear regime extends to nearly 25 or 30% relative extension. Above this limit, the fact that the polymer has a finite extensibility ($R = |\boldsymbol{R}| < L_c$) causes the force to increase nonlinearly with extension, and the nature of this force singularity depends on the short-range flexibility of the chain as will be discussed below.

2.2.2 Self-avoidance and shape effects

The above section was concerned with the equilibrium conformation of chains that can pass through itself. Since no two monomers can occupy the same space, we know that this model is aphysical. In fact, the monomer will interact both with other monomers along the chain and with solvent molecules. The balance of these interactions will affect the size of the coil, and is taken into account with an excluded volume parameter v (or in Flory theory with Flory's χ parameter). If the interactions between monomer and solvent are more favorable than those between monomers, solvent is drawn into the coil, causing the coil to swell. In this case, the excluded volume is positive and the solvent is termed a "good" solvent for that polymer. If the interactions between monomers are more favorable than those between monomer and solvent, the solvent is repelled from the chain and the chain collapses. In this case, the excluded volume is negative and the solvent quality is poor. In the special case where the interactions exactly cancel one another out, the excluded volume is zero and the scalings for chain size return to those for an ideal chain. These special conditions are termed θ conditions. It should be stressed, though, that a chain under θ conditions is not ideal, that is, polymer segments still cannot pass through one another.

Aqueous solutions, like the buffers used in our experiments, have been found to be very good solvents for DNA [57], thus we will focus our attention to the case where the solvent swells the polymer chain. The following is known as "Flory Theory" and those terms, as discussed below, are synonymous with error cancelation in polymer physics. First, let us inspect the excluded volume parameter v, which attempts to summarize all two-body interactions along the chain. For spherical monomers in the limiting case of very good solvents $v \approx w^3$ where w is the diameter of the monomer. For Kuhn segments, $v \approx b^2 w$ [55]. The number of monomer-monomer interactions in the polymer coil is expected to be $\frac{vN}{R^3}$ (the likelihood of a monomer being in the excluded volume of another monomer) for each monomer. Each interaction gives an interaction with energy approximately k_bT and therefore the free energy gain due to two body interactions is

$$F_{monomer} \approx k_bTv\frac{N^2}{R^3}. \tag{2.22}$$

The energy gain due to the loss in entropy with increasing coil size is given by 2.19. Taking the minimum of the total free energy with extension gives a new average coil dimension:

$$R \approx v^{1/5}b^{2/5}N^{3/5} \tag{2.23}$$

Note that the inclusion of long-range interactions (i.e. long in terms of distance along the chain) changes the scaling of the equilibrium polymer size with molecular weight. In general, it is commonly stated:

$$R \sim N^{\nu_d} \tag{2.24}$$

where ν_d is the Flory-Edwards scaling exponent. By analogy with a self avoiding random walk (SAW) it has been shown to that $\nu_d \approx 3/(d+2)$ where $d \leq 4$ is the dimensionality of the system. Important to later aspects of this work is the aforementioned $\nu_{3d} \approx 3/5$ and the scaling exponent in two dimensions $\nu_{2d} \approx 3/4$.

Also note that we have attained this result through the cancelation of two errors made in the derivation by using the ideal chain results above. The number of monomer to monomer contacts is over-estimated because it was calculated using a chain that can pass through itself, therefore greatly over-estimating the number of contacts (i.e. a real chain spreads itself in more space and has less chance of two monomers seeing one another). Secondly, the entropic force pulling the chain back is overestimated as well, since it too was calculated using the ideal chain. Nevertheless, the exponent has been found to agree with more complicated re-normalization group calculations using multi-body statistical mechanics methods (which yield a more exact $\nu_{3d} = 0.589$) [58].

2.2.3 Force-extension beyond the linear regime

This section will present two levels of analyses describing the force-extension behavior of polymers. We have shown, near equilibrium, that the entropic force is linear with applied extension. We know, however, that the polymer cannot be indefinitely extended and some nonlinearity must develop at high extensions due to the finite extensibility of the polymer. Here we will describe the form of the nonlinearity and provide a scaling analysis to illuminate the mechanism for the dependence of the form of the nonlinearity on the short length scale flexibility of the chain.

First, we consider a scaling analysis of polymer stretching, first introduced by Pincus. We assume that the polymer, stretched to a distance X_{ex} can be viewed as a series of "blobs" with a diameter ξ_T. Within each blob, the polymer conformation is not perturbed by the applied extension. This assumption that polymers deform first at larger length scales is not completely unrealistic as most of the conformational entropy of the chain is gained through small-scale conformational changes [55]. Thus there are $N_{blobs} \sim X_{ex}/\xi_T$ blobs, each of which contain $g \sim N/N_{blobs} \sim \xi_T^2/b^2$ Kuhn monomers. Solving for the size of the blob and g we obtain.

$$\xi_T \sim \frac{Nb^2}{X_{ex}} \sim \frac{b}{X_{ex}/L_c} \tag{2.25}$$

$$g \sim \frac{N^2b^2}{X_{ex}^2} \sim \frac{1}{(X_{ex}/L_c)^2} \tag{2.26}$$

It is important to note that for a given polymer chain (i.e. a given L_p) that the size of a blob is constant with the relative extension of the chain regardless of its molecular weight. Secondly, the length scale of the blob is the length scale at which thermal energy is no longer sufficient to "randomize" the conformation of the chain (a general property of "blobs" across all blob theories). Thus, the formation of each blob requires approximately k_bT of energy and the free energy of the

stretched chain can be calculated as

$$F \approx k_b T N_{blobs} \approx k_b T \frac{X_{ex}}{\xi_T} \approx k_b T \frac{X_{ex}^2}{Nb^2} \tag{2.27}$$

and we regain equation 2.19 to within a constant (as good as we can expect the results of a scaling analysis to be).

We can also start to examine the reasons why a WLC and a flexible chain may not have the same force extension behavior at high extensions, even though the differences between the two chains exist only at small length scales. As we stretch the chain, the important length scale in the lateral directions is the width of the chain or the blob size (not the stretched length). At some point, the blob size will become too small for the chain within the blob to be accurately described by equation 2.11 (i.e. the chain within a blob is not long enough to meet the assumptions in equation 2.11) and the intra-blob chain conformation, its probability distribution function, and therefore its force-extension behavior, become highly dependent on its flexibility on length scales below the Kuhn length.

The nonlinear part of the force-extension behavior can be examined with the use of statistical mechanics, which allows the inclusion of all conformations of the polymer (not just the ones where blob theory accurately describes the conformation). In much the same way as the free energy was calculated previously, the partition function of the constant force ensemble (describing the possible conformational states of the polymer at a given force) is used to calculate the Gibbs free energy which is then differentiated to obtain the force on the chain.

The average extension of a freely jointed chain, given a constant force, is calculated as [58]:

$$\frac{\langle X_{ex} \rangle}{L_c} = \left[\coth\left(\frac{fb}{k_b T}\right) - \frac{k_b T}{fb} \right]. \tag{2.28}$$

The WLC does not permit an analytical solution for the entire nonlinear portion of the force extension behavior, although perturbation analyses can be used to solve for the high and low force limits. A useful interpolation formula, which has been experimentally shown to capture the behavior of DNA quite well [42] was given by Marko and Siggia [59].

$$\frac{fb}{k_b T} = \frac{\langle X_{ex} \rangle}{L_c} + \frac{1}{4} \frac{1}{(1 - \langle X_{ex} \rangle / L_c)^2} - \frac{1}{4} \tag{2.29}$$

2.3 Polymer Dynamics and Hydrodynamics

The goal of this section is to introduce polymer dynamics. First, a very simplified model of polymer motion, the Rouse model, is considered, mostly for its mathematical simplicity but also because we will find it accurate in some cases of confined polymers. We will then briefly discuss a theory taking into account the long-range hydrodynamic interactions in the system.

To model polymers and their large length scale motion (relative to the size of the coil) we view the chain as a series of beads and springs. The beads are centers of interaction with the solvent (i.e. all drag between the polymer and solvent occurs at the beads) and the springs represent the connectivity of the chain. In order for the polymer model to match a real polymer, we must make the spring law match that of the coil and the drag of the chain be represented accurately. For

simplicity here, we assume that each section of polymer modeled as a spring is large enough so that the force extension behavior can be modeled by equation 2.20, although recent work has shown that finer coarse graining can indeed be used with appropriate changes to the spring force law [60, 61]. Also, since the masses we deal with at these microscopic scales are small, we neglect inertia, making the velocity of a bead at any given moment in time depend only on the sum of the forces on that bead and the drag on the bead. We use the Langevin equation to describe the motion of N beads with positions $\boldsymbol{r}_n$:

$$\frac{\partial \boldsymbol{r}_n}{\partial t} = \sum_{m=1}^{N} \boldsymbol{H}_{nm} \cdot (\boldsymbol{f}_m^T + \boldsymbol{f}_m^B + \boldsymbol{f}_m^E) \tag{2.30}$$

where t is time and $\boldsymbol{f}_m^T$, $\boldsymbol{f}_m^B$, and $\boldsymbol{f}_m^E$ denote forces on bead m due to tension in the chain, Brownian motion, and any externally applied force, respectively. $\boldsymbol{H}_{nm}$ is the mobility tensor, which converts forces on bead m to forces on bead n, taking into account hydrodynamic interactions (to be discussed below).

2.3.1 Rouse model

As Equation 2.30 stands, it is highly nonlinear and coupled, the velocity of bead n depends upon the velocities and forces upon all other beads in the system. To make mathematical progress, some simplifying assumptions must be used. The Rouse model assumes an ideal chain and that there are no interactions between beads m and n except through the tension of the chain. As such, the mobility tensor becomes

$$\boldsymbol{H}_{nm} = \frac{\boldsymbol{I}}{\zeta}\delta_{nm} \tag{2.31}$$

where $\boldsymbol{I}$ is the identity tensor and ζ is the drag on each bead (assumed constant over all beads). For now we neglect external forces to observe the dynamics of polymers at rest. The tensile force between beads is consistent with the entropic recoil forces described above for ideal chains 2.20

$$\boldsymbol{f}_m^T = \kappa_{H,bead}(\boldsymbol{r}_m - \boldsymbol{r}_{m+1}) \tag{2.32}$$

where $\kappa_{H,bead} = 3k_bT/b^2$ (note that the spring is for a single pair of beads). Taking the steps between beads to be continuous, the equation of motion for the beads then becomes

$$\zeta\frac{d\boldsymbol{r}_n}{dt} = -\kappa_{H,bead}\frac{\partial^2 \boldsymbol{r}_n}{\partial n^2} + \boldsymbol{f}_n^B \tag{2.33}$$

with the boundary conditions that there is no tension in the chain at the chain endpoints: $\frac{\partial \boldsymbol{r}_i}{\partial n}\,|_{i=0,N} = 0$. The solution to this, now linear, stochastic partial differential equation is made through the use of normal coordinates, converting our previously cartesian coordinates to a coordinate system based around the multiple modes of motion of the chain, much like a Finite Fourier Transform [62]. The diffusivity and relaxation time, dynamical quantities which characterize the diffusion of the center of mass of the chain and its long length scale reorganization, are given by time correlations of the renormalized equation [58]. The longest relaxation time is given by:

$$\tau_1 = \frac{\zeta}{\kappa_H} = \frac{\zeta N^2 b^2}{3\pi k_b T} \tag{2.34}$$

and the diffusivity is given by

$$D = \frac{k_b T}{N\zeta} \tag{2.35}$$

In later sections we will be especially interested in the dependence (scaling) of these quantities with molecular weight (N). We note that the longest relaxation time is the ratio of the drag on the longest mode of motion of the chain and the spring constant of the chain; the timescale, if we were to choose one, of the equation of motion. The diffusivity is the ratio of thermal energy to the drag on the chain. Predictably, the drag on the chain increases linearly with molecular weight, a direct consequence of the assumptions used on $\boldsymbol{H}_{nm}$, namely, that each bead only contributes its own drag to that of the polymer.

It should also be noted that the Rouse model describes these long length scale motions even if there are local interactions among the beads, as long as the interactions decay away at some length scale smaller than that of the coil [58]. One can evaluate this statement with a simple thought experiment. If at a given level of coarse graining there are interactions among the beads, simply re-coarse grain the chain at a length scale larger than that of the interaction. The new chain then can be modeled with non-interacting beads, and the long length-scale motion (which should be accurately described with both levels of coarse graining) is easily seen to be in agreement with Rouse theory.

2.3.2 Zimm model

The Rouse model does not describe the dynamics of dilute polymers in bulk well. This is due to the fact that hydrodynamic interactions modify the mobility tensor of the chain. Specifically, the flow field in the solvent caused by the motion of one polymer segment affects the motion of nearby polymer segments. Since this interaction is moderated by the solvent, we can approximate its form by solving for the flow field due to a point force (a Stokeslet), yielding a form for $\boldsymbol{H}_{nm}$.

$$\boldsymbol{H}_{nm} = \frac{\boldsymbol{I}}{\zeta}\delta_{nm} + \frac{1}{8\pi\eta|\boldsymbol{r}_{nm}|}\left[\boldsymbol{r}_{nm}\boldsymbol{r}_{nm} + \boldsymbol{I}\right](1-\delta_{nm}) \tag{2.36}$$

where $\boldsymbol{r}_{nm}$ is the vector from bead n to m and η is the viscosity of the solvent. The mobility tensor depends on the distance between beads n and m, which is, in general, dependent on the instantaneous conformation and therefore not known. However, the *equilibrium average* distance between beads n and m is known (see Equation 2.18) and the pre-averaged interaction tensor can be written as:

$$\boldsymbol{H}_{nm,eq} = \int_0^\infty dr 4\pi r^2 \left(\frac{3}{2\pi|n-m|b^2}\right)^{3/2} \exp\left(-\frac{3r^2}{2|n-m|b^2}\right)\frac{\boldsymbol{I}}{6\pi\eta r} = h(n-m)\boldsymbol{I} \tag{2.37}$$

and the Langevin equation becomes

$$\frac{\partial}{\partial t}\boldsymbol{r}_n = \sum_m h(n-m)\left(\kappa_{H,bead}\frac{\partial^2}{\partial m^2}\boldsymbol{r}_m + \boldsymbol{f}_m^B\right) \tag{2.38}$$

a linear, coupled set of equations. A normal modes analysis is again used and the dynamical quantities are calculated from the time correlations. Above we used the conformation of an ideal

chain at equilibrium to pre-average the interaction tensor, however, it can be shown that the use of a real chain will yield similar results with the inclusion of the Flory-Edwards exponent. The relaxation time predicted by the Zimm model is [58]

$$\tau_1 = 0.325\frac{\eta R^3}{k_b T} \tag{2.39}$$

and the diffusivity

$$D = 0.196\frac{k_b T}{\eta R} \tag{2.40}$$

where R is the rms end to end distance. Note that the dynamics of the chain now depend upon its equilibrium size $D \sim M_w^{-\nu}$ and $\tau \sim M_w^{3\nu}$, which is a consequence of the preaveraging. We note that this assumption is quite gross, essentially tossing out all information about individual conformations to capture the long timescale and long length scale behavior of the chain. However, the model predicts experimental behavior extremely well, often in settings far removed from the original purpose of the model.

2.3.3 Polymers in flow and polymer stretching

Many studies have used flow to alter the conformation of single DNA molecules. Studies have focused on shear [63, 64, 65], elongational [51, 52, 66, 67], and mixed flows [68, 69]. Shear flows have a rotational component, which causes DNA molecules to extend and then tumble, resulting in an aperiodic extension-tumble-relaxation mode of motion. Since we are trying to extend molecules, we focus here on DNA dynamics in pure extensional flows and, due to the set up of our microscope (we can observe in-plane motion), planar extensional flows. The velocity field of such flows is given by:

$$v_x = \dot{\epsilon} x \tag{2.41}$$

$$v_y = -\dot{\epsilon} y \tag{2.42}$$

where v_x and v_y is the velocity field in the x and y directions, respectively, and $\dot{\epsilon}$ is the strain rate which describes the strength of the flow. As can be extrapolated from the above derivations, adding a spatially-dependent external forcing term ($\boldsymbol{f}_m^E$) creates significant complexity, especially when hydrodynamic interactions are considered. For illustration here, we take the simplest of all models: a Rouse chain with only two beads and without Brownian fluctuations. The math is simplified further if we use symmetry and consider only half of the dumbbell with the centerpoint tethered (see Figure 2.1). We will use the WLC force-extension behavior in the spring force law to make the results more applicable to DNA stretching.

The external force acting to extend the molecule in the x direction can be written as:

$$\boldsymbol{f}^E = \zeta v_x = \frac{1}{2}\zeta\dot{\epsilon}X_{ex}. \tag{2.43}$$

Setting this equal to the WLC force law (Equation 2.29) yields:

$$\boldsymbol{f}^T = \frac{k_b T}{L_p L_c}\left[\frac{X_{ex}}{L_c} - \frac{1}{4} + \frac{1}{4}\left(1 - \frac{X_{ex}}{L_c}\right)^{-2}\right] = \zeta\dot{\epsilon}\frac{1}{2}\frac{X_{ex}}{L_c} = \boldsymbol{f}^E \tag{2.44}$$

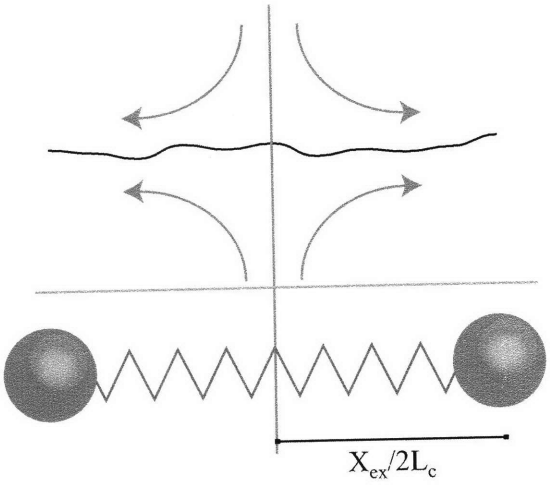

Fig. 2.1: *Schematic of the dumbbell model used in the stretching analysis.*

Grouping the constants together, it is possible to extract the relaxation time (Equation 2.34) and the Deborah number $De \equiv \dot{\epsilon}\tau_1$ naturally drops out of the analysis.

$$3De\frac{X_{ex}}{L_c} = \left[\frac{1}{4}\left(1-\frac{X_{ex}}{L_c}\right)^{-2} - \frac{1}{4} + \frac{X_{ex}}{L_c}\right] \tag{2.45}$$

The De compares the rate of extension to the longest relaxation time of the polymer. At $De > De_{crit}$, the rate of extension exceeds the relaxation rate (in the linear force regime) and the polymer extends significantly until sufficient nonlinearity in the spring force is built up to balance the extensional force. In the absence of HI, $De_{crit} = 0.5$. Larson and Magda [70, 71] have shown $De_{crit} \approx 0.54$ using a Zimm-preaveraging to account for HI, approximately a 10% correction.

The stretching of polymers in flows is a complex physical behavior, since, as we have seen above, polymer dynamics is intimately tied to conformation through hydrodynamic interactions. Additionally, the tension distribution along the stretched polymer is not uniform. The tension is greatest in the center of an untethered stretched polymer and decays to zero at both ends, thus the polymer is most stretched at the center with less stretching towards the polymer ends. Thus, hydrodynamic interactions may vary along the length of the polymer. Several studies have attempted to model polymer deformation in flow using blob theories and assuming different polymer conformations to account for the varying hydrodynamic interactions [72, 73, 74] and the results have been shown to agree with experiments [75]. However, the dumbbell model proposed above describes polymer behavior in extensional flows very well [67], and this model makes available a simple toy system for further thought and experiment in the area. Thus, whenever the dumbbell model adequately describes results, we tend to use it as a basis of comparison.

It should be noted that stretching of extremely long DNA molecules has resulted in conformational hysteresis [76] due to the fact that the drag on the stretched polymer is significantly higher more than the drag on the coiled polymer, meaning that a stretched polymer is easier to stretch

than a coiled polymer [76, 77]. However, the lengths of DNA used in those studies is an order of magnitude greater than that of the DNA used here, and we do not expect or observe hysteretic effects. However, near the critical De, studies have observed increased fluctuations of the coil size. This is due to the fact that the Brownian forces do still contribute to the dynamics, and near the critical De a small change in the total force on the molecule results in a large change in the extension. This effect can also be viewed as a leveling of the extension energy landscape near the critical point, allowing thermal energy to distribute the extension over a wide range. Due to these increased fluctuations, polymers in extensional flows take a long time to reach equilibrium, much like solutions near critical points, and the physics relate to the general behavior of "critical slowing down."

Molecular individualism and preconditioning

The above section dealt with the steady-state stretching of polymers, but the dynamics of polymer stretch are interesting in their own right. The conformation of the polymer can affect the rate of stretch, not only through HI but also in a more topological manner. Termed "molecular individualism," the dynamics of polymer stretching vary widely from molecule to molecule due to the random initial conformation of the polymer. It should not be surprising that the time evolution of the monomers in the chain depend on their initial condition, but the extent to which individual molecules vary is striking. Some molecules have been shown to reach full extension in a strain of 4, while others take an additional 6 units of strain, corresponding to an increase of factor of $e^6 \approx 400$ in the deformation of the solvent. This remarkable increase has been correlated to the formation of kinks and folds in the polymer conformaiton during stretch [51, 52, 78].

This wide variation in polymer behavior prompted attempts to make polymer stretching more predictable, a characteristic that is highly valued with the advent of direct genome mapping. Such efforts (which were mainly done in simulations [78]) focused on making the original polymer conformation more amenable to stretch, or "pre-conditioning" the polymer. It has long been known that concentrated polymeric solutions demonstrate variations base on processing history, i.e. a memory of past forces and flows affect the current dynamics of the polymer. In one point of view, "preconditioning" studies are the single-molecule equivalent, and may be beneficial to understanding these effects in more concentrated solutions.

2.4 Confinement Effects and Confinement Theories

The goal of this section is to introduce the theoretical background for confined polymer chains of interest in the later parts of this thesis. First, the general physical effects of confinement will be discussed, and their repercussions are developed in De Gennes' blob theory (confinement blob theory). In this section we discuss the general applicability of blob theory and leave its derivation to later sections.

2.4.1 Types of confinement and physical effects

Much experimental and theoretical work has been performed on confined polymers in differing types of confinement defined by the geometry of the system. In this work, we are concerned nearly exclusively with polymers confined in slit-like channels where the confining dimension (the channel height) $h < R_{g,bulk}$ and the non confining dimensions (the width of the channel) $w \gg R_{g,bulk}$.

Channels with moderately high aspect ratios have and continue to be a motif in microfluidic systems because of the facility in fabrication (photolithography defines the O(100) μm features) as well as the combined advantages of small-length scales and higher throughput available with increasing aspect ratio.

There are two main consequences of placing polymers in confinement. First, the shape of the polymer changes, which changes the equilibrium distribution of monomers as well as the spring force law (which is shown above to be related to the monomer probability distribution function). Regardless of the solvent quality, polymers in confinement will be compressed in the confined directions and expanded in the unconfined directions. Second, the nature of the hydrodynamic interaction is changed due to the fact that confinement alters the nature of the hydrodynamic interaction tensor (mobility tensor). Most notably, the velocity magnitude decay changes from $1/r$ to $1/r^2$ in slit confinement.

2.4.2 De Gennes' blob theory

De Gennes and coworkers [79, 80, 81] developed a theory accounting for the effects of confinement on polymer conformation and dynamics for channels heights on the order $L_p \ll h \ll R_{g,bulk}$. The theory has four assumptions, one each conformational and dynamical at large and small (relative to the channel height) length scales. the four assumptions are as follows:

1. At short length scales, the polymer does not "feel" the walls so the polymer attains a 3d SAW conformation and

2. the hydrodynamic interactions are as in bulk and the dynamics follow Zimm scalings.

3. At large length scales, the polymer is in intimate contact with the channel walls and attains a 2d SAW conformation and

4. hydrodynamics are screened, so the long-range polymer motion follows Rouse scalings.

These four assumptions are consistent with general blob theories: the force on the polymer affects only the longer polymer length scales (see Figure 2.2), while the polymer at small length scales (within a blob) does not feel the external force. Also, scalings for the polymer free energy can be derived from the number of blobs as was done above, and the four assumptions can be used to derive the conformation and dynamics of polymer systems. The details of blob theory will be introduced as needed in future chapters, but a few important points concerning the applicability of statements 1-4 above will be pointed out here.

First, the assumption that hydrodynamics are screened in slit confinement can be called into question. Liron and Mochon [82] and others have shown that the velocity decay (and therefore the distance dependence of the mobility tensor) goes as $1/r^2$ in confinement. While this is steeper than the $1/r$ decay in bulk, prior to the work presented here there had been no evidence (to our knowledge) proving that a $1/r^2$ decay is sufficient to *screen* interactions. "Screening," in fact, implies exponential decay over a length scale significantly shorter than other length scales present in the physical system, which is clearly not present with an algebraic decay.

Second, the assumptions above do not account for all polymer-wall interactions. Solid objects moving next to walls experience higher drag due to the increased velocity gradient at the object caused by the no slip condition at the boundary'[83]. Also due to the no slip boundary condition,

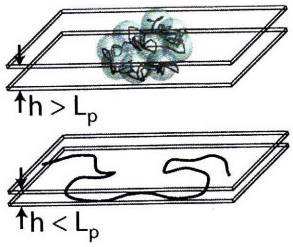

Fig. 2.2: *Schematic of the conformation in confinement for polymers in the blob theory regime (top) and the reflecting chain regime (bottom).*

hydrodynamic interactions change significantly (are more Rouse-like) near solid walls. Neither of these effects are accounted for in de Gennes' theory. In fact, blob theory is most applicable to confined systems that are far away from boundaries; realized when infinitely large polymers are confined in slightly smaller infinitely large channels. Experimentally, the presence of walls is necessary and we should keep these drag effects in mind during analysis of our experimental results.

2.4.3 Odijk theory

At smaller channel heights $h \ll L_p$, the nature of confinement changes drastically and a new theory is required. At these channel heights, the polymer does not have adequate flexibility to double back on itself. As such, the polymer attains a "reflecting chain" conformation (see Figure 2.2), first described in detail by Odijk [84]. Recent experiments have observed a sharp transition in polymer behavior at channel heights $h \approx b$ [85, 86], which is ascribed to the transition to the Odijk regime. Experimental results display a decrease in the relaxation time with increasing confinement and conformation dependencies consistent with the Odijk models. These initial results make a promising comparison to the model, but a complete test is still lacking. As the channels to be studied in this thesis are all greater than the Kuhn length of DNA, we do not expect the Odijk regime to play an important role in the dynamics observed.

2.5 Electrokinetics

In this section we introduce a few practical matters concerning the transport of DNA in confinement. Since the velocity of pressure-driven flows vary as h^3, extremely high pressure gradients are needed to cause appreciable flow in small channels. In this work, we focus on electrokinetic methods of DNA transport, and we introduce relevant concepts here.

2.5.1 Charged surfaces

When a surface is in contact with an ion-carrying solvent, the surface tends to build up an equilibrium charge through interactions with those ions. The surface charge then creates an electrostatic potential in the neighboring solution, which then influences the equilibrium distribution of neigh-

boring ions. We will see in later sections how these surface effects influence DNA and even solvent behavior in microchannels.

The electric field (and ion distribution) near a uniformly charged, smooth surface has been analytically described [62, 87]. From Gauss' law,

$$-\varepsilon\nabla^2\Phi = \rho_e = F\sum_i z_i C_i \tag{2.46}$$

where ε is the permittivity of the solvent, Φ is the electrostatic potential, F is Faraday's constant, ρ_e is the free charge density, and z_i and C_i are the valence and concentration of ionic species i, respectively. If we then assume that the ions in solution obey a Boltzmann distribution (at equilibrium) $C_i = C_{i,\infty}\exp\left(-z_i F\Phi/k_b T\right)$, we can obtain an expression for the potential in solution:

$$\nabla^2\Phi = -\frac{F}{\varepsilon}\sum_i z_i C_{i,\infty}\exp\left(-\frac{z_i F\Phi}{k_b T}\right) \tag{2.47}$$

where $C_{i,\infty}$ is the concentration of ionic species i in bulk (far from the surface). Assuming small potentials (small surface charges), we can expand the exponential as $\exp(x) \approx 1 - x$. If the solution is electroneutral far from the surface, $\sum_i z_i C_{i,\infty} = 0$ and the first term of the expansion vanishes. Taking the linear term of the expansion of Equation 2.47.

$$\nabla^2\Phi = \kappa^2\Phi \tag{2.48}$$

where κ^{-1} is the Debye length

$$\frac{1}{\kappa} = \left(\frac{\varepsilon k_b T}{F^2\sum_i z_i^2 C_{i,\infty}}\right)^{1/2} \tag{2.49}$$

The Debye length (also called the electrostatic screening length) is the natural length scale for electrostatic interactions in a solution. Note that κ^{-1} is indeed a solution property and is not dependent on the surface charge provided that the linearization (Debye-Huckel approximation) step holds (for strongly charged systems Gouy-Chapman theory shows the same physical importance of the Debye length [87]). Thus charged bodies separated by more than a few κ^{-1} are not repelled or attracted to one another. In the salt concentrations used in this study $C_\infty \approx 0.01$ to 0.1M, $\kappa^{-1} \approx 1$ to 3nm, significantly less than the other physical length scales in the problem, saving one. The diameter of the DNA molecule is 2 nm, and it has very recently been shown that electrostatics slightly affect physics where the diameter of DNA is important (excluded volume interactions in v, see equation 2.23) at the salt concentrations used here [88]. The closeness of scales of these two parameters will arise again in discussions of electrophoresis of DNA molecules. In terms of DNA/wall interactions, since glass attains a negative charge in solutions with near-biological pH (like our buffers), DNA will tend to be repelled from the walls over length scales comparable to the Debye length, and therefore will be excluded from a negligible portion of the channel (relative to the channel height) in the following studies.

If we continue with the analysis above and evaluate the potential near a charged plane (like the surface of a channel with $h > \kappa^{-1}$). We obtain:

$$\frac{d^2\Phi}{dz^2} = \kappa^2\Phi \tag{2.50}$$

where z is a coordinate which determines distance into solution from the plane. We know the surface charge and that the potential must die away in bulk solution, thus

$$\Phi = \frac{q_e}{\varepsilon\kappa} \exp(-\kappa z) \tag{2.51}$$

where q_e is the surface charge density. The ion concentrations also follow an exponential approaches to their bulk values with the same length scale. Electronuetrality in the liquid is only broken at scales associated with the Debye length. The changes in potential and ion concentrations near a charged surface are often described as an "electrical double layer" (EDL).

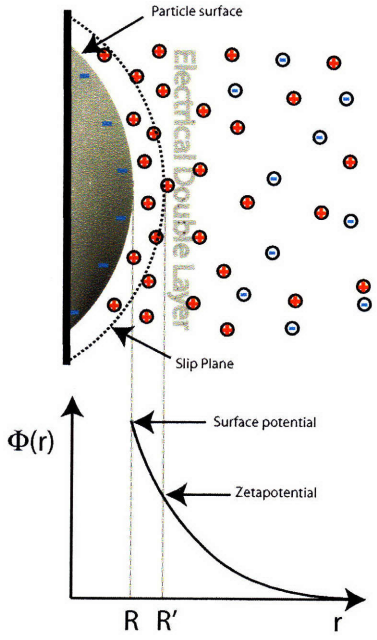

Fig. 2.3: *Schematic of the electrical double layer around a spherical particle*

2.5.2 Electroosmosis

To move DNA in small channels, an electric potential is applied across the channel, which sets up an electric field along the channel (E_x). This electric field acts parallel to the solid/solution interface and imparts a force to the charged fluid near the wall, causing electroosmotic flow (EOF). The velocity field set up by EOF where $\kappa^{-1} \ll h$ can be described by

$$v_x = -\frac{q_e E_x}{\kappa\eta}\left[1 - \exp(-\kappa z)\right] \tag{2.52}$$

Note that over most of the channel, the velocity profile is plug-like and varies in space only for $z \sim \kappa^{-1}$. Also note that the *strength* of the interaction at a given applied field depends on the salt concentration of the solution (through κ in the prefactor), the charge of the surface, and the viscosity

of the solution near (or at) the interface. Thus, EOF effects can be mitigated by operating at high ionic strengths and by selectively increasing the solution viscosity near the liquid/solid interface. One method used throughout this work is to dynamically adsorb surface-active polymers to the interface, drastically increasing the viscosity there and therefore decreasing the EOF velocity.

2.5.3 Electrophoresis

The application of electric fields also induced forces on the charged bodies themselves, and, if these objects are free to move, electrophoresis (EP) results. Mathematically, electrophoresis is a complicated problem since the charged body is surrounded by an electric double layer, which is also affected by the electric field (see Figure 2.3). For a large particles ($\kappa^{-1} \ll$ radius of particle), moving slowly enough through the fluid such that structure of the EDL does not change, and with no background pressure-driven flows, Smoluchowski derived an expression for the velocity of the particle due to electrophoretic effects:

$$\boldsymbol{v} = -\frac{\Phi_\zeta \varepsilon \boldsymbol{E}}{\eta} \tag{2.53}$$

where Φ_ζ is the zeta potential (potential in solution at the slip plane of the particle). The velocity is usually written

$$\boldsymbol{v} = \mu \boldsymbol{E} \tag{2.54}$$

where μ is the electrophoretic mobility. However, since the diameter of DNA is small relative to the thickness of the EDL, it is unclear whether the Smoluchowski equation holds for DNA mobility. Also, the additional complication of DNA being a flexible entity complicates matters, as tension distributions and conformational change may affect the mobility, or different mobilities in different sections of chain may add to the tension in the chain.

In the case of high salt concentrations, however, a study by Long *et al.* [89] showed that a polyelectrolyte of uniform charge density retains its equilibrium conformation during free electrophoresis. The authors used a bead-model of the chain, but separated hydrodynamic interactions due to electrophoretic motion from those due to other (Brownian, flow-induced, tensile) motion. The physical reason for this is the fact that during electrophoretic motion of the beads, the EDL surrounding the bead moves in the opposite direction, negating the velocity field at distances much larger than the Debye length [90, 91]. The equation of motion is solved, again using normal modes as above for the Rouse and Zimm models. The authors conclude that (1) the mobility in free solution of polyelectrolytes in high salt is independent of molecular weight and (2) there is no deformation of the polymer coil during free solution electrophoresis.

It is important to note that although the mobility of DNA may not strictly adhere to the Smoluchowski assumptions, the mobility of DNA is found to be constant at low $\boldsymbol{E}$ (in the range used in the following study) and independent of molecular weight for large ($>\sim$ 1 kbp) DNA. Also, the mobility measured is the sum total of all electrokinetic effects (assuming pressure differences are made negligible), that is, a sum of EOF and EP induced velocities. The measured mobility, then, will depend on the channel surface charge (channel material), the amount of EOF quenching, and ionic strength. In the studies that follow, we take the mobility as a measured constant in a given experiment (checked for consistency) applicable to all sections of the DNA molecule.

A secondary result of that analysis is that hydordynamic interactions are present in chains deformed by electric field gradients. Since the recoil mechanism is tension-induced (i.e. not an

electrophoretic force), the HI are not modified by the EDL and the Zimm model therefore applies to the relaxation process. A theory embodying this idea is termed "Electro-hydrodynamic Equivalence," pointing to the fact that a polymer deformed in an electric field E will behave the same as if it were in a uniform pressure-driven flow of velocity μE. This theory has been experimentally verified with tethered polymers [36, 92], however experiments free of the complication of tethering do not exist at this time.

2.6 Summary

This chapter introduced several basic aspects of polymer physics and the behavior of DNA in electric fields. The equilibrium polymer conformation and dynamics were described at length, and changes to polymer behavior upon confinement were introduced at a physical level. The motion of solvent and DNA upon application of an electric potential were described for conditions similar to experimental conditions discussed later in the thesis. The discussion here is by no means complete, nor is it meant to be, but we hope the reader is now equipped for the remaining portions of this thesis.

CHAPTER 3

Diffusion in Confinement and Hydrodynamic Screening

The purpose of the following chapter is to experimentally and mathematically verify that the changes to the mobility tensor induced by confinement are sufficient make hydrodynamic interactions negligible in the long length scale motion of DNA molecules. Experimentally, we investigate the diffusivity of DNA in confinement and compare the molecular weight dependence to the Rouse and Zimm models (equations 2.35 and 2.40) to determine which is applicable to describe dynamics in confinement. We also follow a Zimm-like scaling analysis to determine whether the change in the magnitude of the interaction (mobility) tensor damps HI sufficiently to allow the use of a local (Rouse) model to describe long-length scale behavior. We extract scalings with channel height as well, which are found not to agree with predictions from blob theory. The deviations with channel height are left to later chapters where a development in the experimental protocol allowed a complete comparison to and evaluation of blob theory. Here, using very basic principles of transport, we are able to show conclusively that hydrodynamic interactions are not important in the long length scale polymer motion in confinement, a fact that had eluded proof in the literature for some time. This small step, which is important in its own right, allowed us to conceptually pull apart blob theory for analysis in chapter 4.

3.1 Overview

We present an experimental study of double-stranded DNA diffusion in slit-like channels. The channel heights span the regime from moderate confinement (height $\sim$ bulk radius of gyration of the DNA) to strong confinement (height $\gtrsim$ Kuhn length). Scalings of diffusivity with channel height differ from blob model predictions. The diffusivity scales inversely with molecular weight when the channel height is smaller than the bulk radius of gyration. This scaling is indicative of hydrodynamic screening. A scaling analysis shows that the screening of hydrodynamic interactions arises from a combination of two mechanisms. After using a Zimm pre-average approximation, the unique symmetry of the thin-slit disturbance velocity and the isotropic nature of the polymer conformation together cause a cancelation of hydrodynamic interactions due to symmetry. We also find that the algebraic decay of the far-field velocity magnitude is sufficient to eliminate large-length scale hydrodynamic cooperativity in diffusion of quasi-two-dimensional polymers in good solvents.

3.2 Introduction

Advances in microfabrication technologies have allowed the fabrication of fluidic channels with a characteristic dimension on the order of tens of nanometers [93, 94]. The potential for the use of small-channel devices in DNA mapping [45, 48, 50, 85, 95] and separation [16, 17, 25, 96, 97, 98], single biomolecule manipulation [16], and even ion separation [99, 100] has inspired interest in the static and dynamic response of individual molecules to confinement [22, 101, 102]. The proximity of the bounding walls offers a very powerful method to change the polymer equilibrium conformation through steric interactions as well as the polymer dynamics through modulation of hydrodynamic interactions (HI). These effects manifest themselves by changing molecular transport properties such as the diffusivity, relaxation times, and mobility.

Theoretical and experimental studies of polymeric behavior in confinement extend well into the past [79, 80, 84, 103, 104, 105]. Today, microfabrication allows greater control over the size and shape of the confining environment. Furthermore, the use of biological macromolecules makes possible the study of mono-disperse samples, and epiflouresence microscopy allows one to directly observe single DNA molecules. Austin and coworkers [85, 95] have studied double-stranded (ds)-DNA behavior in small (35 nm to $\sim$ 400 nm) square channels. They find expected scalings of extension with molecular weight, but scalings with channel height are slightly different from proposed theory. Also, they attribute a drastic change of relaxation behavior in channels approximately 140 nm square to a conformational change from a "blob-like" state [79, 80] to the conceptual "reflecting chain" of Odijk [84] (Figure 3.1). The dynamics differ greatly when the geometry is a slit, especially under strong confinement conditions. In the limiting case, a square channel or tube constricts polymer motion to a reptation mechanism, however, in a slit there is a finite lateral mobility (x-y plane in Figure 3.1). Bakajin *et al.* [102] studied the extension of DNA around posts in slit-like channels. They were able to prove electro-hydrodynamic equivalence and showed that intramolecular HI was negligible in the smallest channel used (90 nm). However, the study only qualitatively reported changes to transport properties (longest relaxation time). Maier *et al.* [106, 107] studied DNA confined to a cationic lipid bilayer and found that 2-dimensional scaling laws held for both static and dynamic quantities. They also found that intramolecular HI does not affect DNA behavior due to the strong coupling between the DNA and the bilayer. While scalings for DNA on lipid bilayer membranes have been shown to agree with theory and the ability of slit-like channels to screen HI

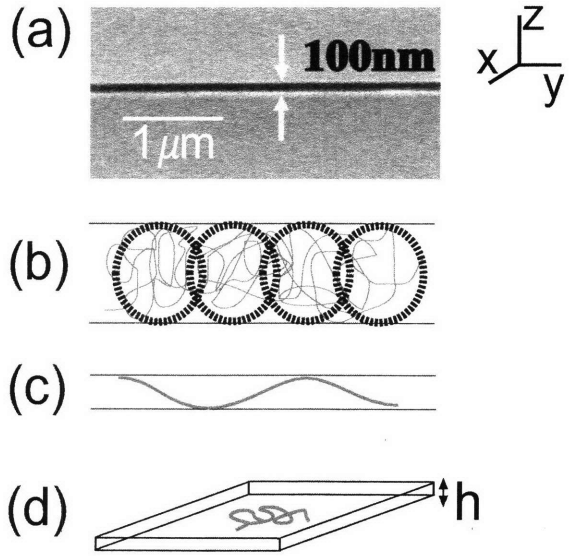

Fig. 3.1: *(a) SEM image of a glass channel cross section with a slit height of 100 nm. Also shown are schematics of polymer conformations in a slit-like channel for (b) $R_{g,bulk} \gg h \gg L_p$ (blob regime) and (c) $h \ll L_p$ (Odijk regime). A top view (d) shows the polymer attains a 2-D random walk and is free to diffuse laterally. This motion is readily observed with fluorescence microscopy.*

has been demonstrated, a detailed, quantitative understanding of slit-confined polymer behavior is lacking.

Recently, we studied DNA diffusion in slit-like channels made of PDMS and glass [101], but the mechanical integrity of the PDMS did not allow for study of chains confined much beyond the bulk radius of gyration. In this paper, we systematically examine the effects of channel height and molecular weight on the diffusion of ds-DNA molecules in slit-like nanochannels. Through the use of channels with gap heights that straddle the bulk radii of gyration of the polymer, we wish to experimentally test whether and at what length scale intramolecular HI is screened in slit-like channels. We also present a scaling-level analysis for the mechanisms of hydrodynamic screening in quasi-two-dimensional (Q2D) environments. This information will be useful in the design of nanofluidic devices to manipulate single molecules.

3.3 Theoretical Overview

First, we briefly review the scaling predictions for polymers in confinement. We consider a linear polymer of N monomers with a persistence length L_p, diameter d, and molecular weight $M_w \sim N$ in a slit of height h. In bulk, the polymer attains a coiled configuration with a radius of gyration $R_{g,bulk} \sim L_p N^{\nu}$, where ν is the Flory-Edwards exponent ($\approx \frac{3}{5}$ for good solvent) [108]. In confinement, the polymer can be described as a chain of shorter "segments" with a characteristic length

scale near h. The nature of these segments is defined by the static conformation the polymer can attain between the two planes. In effect, the polymer is coarse-grained near the length scale of the channel height. De Gennes and co-workers [79, 80] developed a theory for moderate confinement where $L_p \ll h \ll R_{g,bulk}$ and the "segments" of the polymer contain enough persistence lengths themselves to follow the high molecular weight conformational scalings developed by Flory (Figure 3.1b). These segments are termed "blobs" and contain $g \sim (h/L_p)^{(1/\nu)}$ monomers (there are $N_{blobs} = N/g$ blobs per chain). For stronger confinement ($h \ll L_p$), the chain cannot double back on itself and attains a "reflecting" conformation (Figure 3.1c) as described by Odijk [84]. In this case, we take the polymer segment to be a rod with length equal to the Odijk length scale $\lambda_{Odijk} \sim L_p^{1/3} h^{2/3}$ [84, 109, 110] and diameter d (there are $N_{rods} \sim N/\lambda_{Odijk}$ rods per chain). In the development of these theories, it is assumed that cooperative motion of the segments due to HI is negligible because HI is screened over distances larger than the channel height. The drag on the chain is then solely dependent on the drag on a polymer segment and the number of those segments in the chain ($\xi_{chain} \sim \xi_{segment} N_{segment}$). The drag on an individual segment is taken to be $\xi_{blob} \sim h$ [79, 80] and $\xi_{rod} \sim \lambda_{Odijk}/\log(h/d)$ [85, 111] for the blobs and rods respectively. Taking into account both the conformation and the hydrodynamics, scaling expressions for the in-plane diffusivity ($D \sim 1/\xi_{chain}$) in good solvent are the following

$$D_{blob} \sim \frac{1}{\xi_{blob} N_{blobs}} \sim \left[\frac{1}{h}\right] \left(\frac{h^{\frac{5}{3}}}{M_w L_p^{\frac{5}{3}}}\right) \tag{3.1}$$

$$D_{Odijk} \sim \frac{1}{\xi_{rod} N_{rods}} \sim \left[\frac{\ln(h/d)}{\lambda_{Odijk}}\right] \left(\frac{\lambda_{Odijk}}{M_w}\right) \tag{3.2}$$

The equations are left expanded to emphasize the contribution of the drag on an individual segment (square brackets), the number of segments defined by the conformation between the planes (parentheses), and the screened HI (unity exponent on the term in parentheses). Note that scaling of D with M_w isolates the effect of hydrodynamic interactions. The scaling of D with h is a combined effect of hydrodynamics, the conformation of a segment, and the drag on that segment. Also, since hydrodynamics are assumed to be screened regardless of the shape of the polymer, we can expect $D \sim M_w^{-1}$ even for channel heights between the ranges of applicability of the two equations above.

While making the assumption of screened hydrodynamic interaction simplifies the analysis, a closer examination calls the assumption into question. Hydrodynamic interaction occurs through disturbances of the solvent, the velocity of which must satisfy Stokes' equations at low Reynolds numbers. For the case of the far-field velocity of a point force between two parallel planes, the expression obtained by Liron and Mochon [82] can be reduced to

$$\boldsymbol{v}(\boldsymbol{r}) \sim \frac{1}{|\boldsymbol{r}|^2} \left(\hat{\boldsymbol{r}}\,\hat{\boldsymbol{r}} - \frac{1}{2}\boldsymbol{I}\right) \cdot \boldsymbol{f} \tag{3.3}$$

where $\boldsymbol{I}$ is the unit tensor, $\boldsymbol{v}$ is the in-plane velocity at a point defined by the vector $\boldsymbol{r}$ ($\hat{\boldsymbol{r}} = \boldsymbol{r}/|\boldsymbol{r}|$) due to a point force $\boldsymbol{f}$ at the origin. This expression is valid for $|\boldsymbol{r}| > h$ and decays only slightly faster than in bulk ($1/|\boldsymbol{r}|$). The rate of this algebraic decay alone has never been tested (to our knowledge) to be able to dampen the disturbance enough to eliminate cooperative motion between polymer segments, although its orientational effects have been studied in the HI between colloids [112, 113, 114, 115].

DNA	basepairs $\times 10^{-3}$	D_{bulk} (μm/s^2)	$R_{g,bulk}$ (μm)
M13mp18	7.2	1.32 ± 0.1	0.24 ± 0.02
$\frac{1}{2}\lambda$	24.4 ± 0.2	0.65 ± 0.06	0.45 ± 0.04
λ	48.5	0.46 ± 0.03	0.69 ± 0.05
2λ	97.0	0.28 ± 0.07	1.15 ± 0.03
T4	165.6	0.22 ± 0.03	1.46 ± 0.2

Table 3.1: *Molecular weight dependent properties of stained DNA molecules used in our experiments. Bulk diffusivity and radius of gyration data for T4 DNA was obtained through interpolation of data in Smith et al. [57] since we could not obtain significantly long enough traces where the entire molecule was in focus for the bulk measurement. Radii of gyration are obtained from the bulk diffusivity via* $R_{g,bulk} = 0.203 k_b T/(\sqrt{6}\eta D_{bulk})$.

3.4 Experimental Methods

3.4.1 Channel fabrication

We experimentally observe double-stranded DNA using single molecule epifluorescence microscopy in slit-like nanochannels with gap heights between 75 and 545 nm and a width of 150 μm. The glass nanochannels used in this study were fabricated as described in Mao and Han [94]. A schematic of the geometry and an SEM image of a channel is given in Figure 3.1. The channels are found to have low surface roughness without appreciable sagging [94]. We observe the DNA at least 15 μm away from the side of the channel to minimize any hydrodynamic effects related to the sides of the channel. Diffusivities calculated in channels as narrow as 50 μm wide do not vary appreciably from the data reported here.

3.4.2 DNA preparation

λ-DNA (48.5 kbp) and M13mp18 (7.2 kbp) DNA were purchased from New England Biolabs (NEB) and T4GT7 (165.6 kbp) DNA from Nippon Gene. An XbaI (NEB) digestion was used to linearize the M13mp18 DNA and cleave the λ-DNA at the 24,508th basepair, resulting in two λ-DNA halfmers ($\frac{1}{2}\lambda$) ($\pm$ 250 bp). λ-DNA dimers (2λ) were made using an oligo-protected ligation [116] (DNA oligomers from Sigma Genosys). The results of the biomolecular techniques were tested by staining and then combing the DNA onto a polystyrene-coated coverslip and measuring their contour length relative to a λ-DNA control. This collection of DNA gave $R_{g,bulk}$ values, smallest to largest, of 0.23, 0.49, 0.69, 1.15, and 1.48 μm as calculated from bulk diffusion measurements via $R_{g,bulk} = 0.203 k_b T/(\sqrt{6}\eta D_{bulk})$ [57, 101]. The DNA properties are summarized in Table 3.1.

Experimental runs were carried out in 0.5 $\times$ TBE (0.045 M Tris-Borate, 1 mM EDTA, OmniPur) and 4 vol% beta-mercaptoethanol (BME) (CabioChem). The viscosity of this buffer was 1.1 cP, measured through a diffusion analysis of 0.518 μm (diameter) spherical beads. The Debye length in this system is $\approx$ 2.5 nm, much less than the smallest channel height used. Repulsive electrostatic interactions with the channel surfaces are not expected to play a large role in processes other than

to confine the DNA to the channel. Since the ligation and digestion reactions were carried out in different buffers (NEB), exchange to the TBE buffer took place in Centricon (Millipore) filters. We found we could not use TBE buffer directly in the Centricons, presumably due to an interaction between the borate ion, the cellulose filter, and the DNA [117], so the exchange was first to TE buffer [0.09 M Tris (Promega), 2 mM EDTA (OmniPur)] and then diluted with equal parts in 0.09 M boric acid (J.T. Baker). DNA was stained with YOYO-1 dye (Molecular Probes) at a 4:1 base pair to dye molecule ratio (saturation) and allowed to sit overnight. Directly before use, the channel was loaded with the TBE/BME buffer (without DNA) and an electric field was applied to induce electroosmotic flow and equilibrate the channel. DNA-containing buffer was then placed at the cathodic reservoir and loaded (typical field $\sim$ 100 V/cm) into the channel for observation. Bulk measurements were obtained in a custom diffusion cell consisting of two glass slides separated by a $\sim$100 μm parafilm spacer and sealed with epoxy.

3.4.3 Observation and analysis

Epifluorescence microscopy was used to observe the DNA using a set up described previously [101]. Images of the stained DNA were collected with a Hamatsu EB-CCD camera (model: 7190-21) at 30 frames per second. Image analysis was performed using custom-written code and IDL software. In each frame, the background noise level was subtracted from the image and then the DNA center of mass (in the x-y plane) was calculated as the first moment of the intensity distribution [15, 101] (see Figure 3.2). The center of mass of more than 20 DNA were tracked for an average of 10 seconds each for every channel height and molecular weight condition. We calculated the center of mass displacement as a function of the time elapsed between the frames in which the displacement was measured (lagtime). The gap-averaged, in-plane diffusion coefficient (D) was obtained from the slope of the mean square displacement versus lagtime [101]. The error in the diffusivity was estimated as $\sigma_D/\sqrt{N_{DNA}}$ where σ_D is the standard deviation of the diffusivities of individual DNA molecules and N_{DNA} is the number of DNA molecules (tracked for a constant amount of time). We calculated the probability density functions of the displacement at all lagtimes (van Hove correlation functions) to ensure the absence of appreciable flow effects (see Figure 3.2). Also, the probability density functions were normally distributed and the mean-square displacement plots were linear, implying a lack of adsorption to the channel walls and/or obstruction in the channels over observable timescales [118]. In addition, the conformation of the DNA during loading and unloading into the visualization area did not show evidence of stretching or deformation due to interactions with the surface.

3.5 Results and Discussion

3.5.1 Nanoslit experimental results

Experimental results of confined behavior are plotted on a master curve to test the applicability of blob theory. If blob theory holds, a plot of the in-plane diffusivity in the confined slit (D) normalized by the diffusivity in bulk (D_{bulk}) versus $R_{g,bulk}/h$ yields a universal curve with a slope of -2/3 [80, 101]. Figure 3.3 shows this plot for all of the data collected in this study compared with results from Chen *et al.* [101]. Comparison with simulation and prior experiment is very favorable. Most of the information we can extract from this plot comes in the form of the data collapse. Here, the collapse is good, although the spread of the band is outside of the error bars (one standard

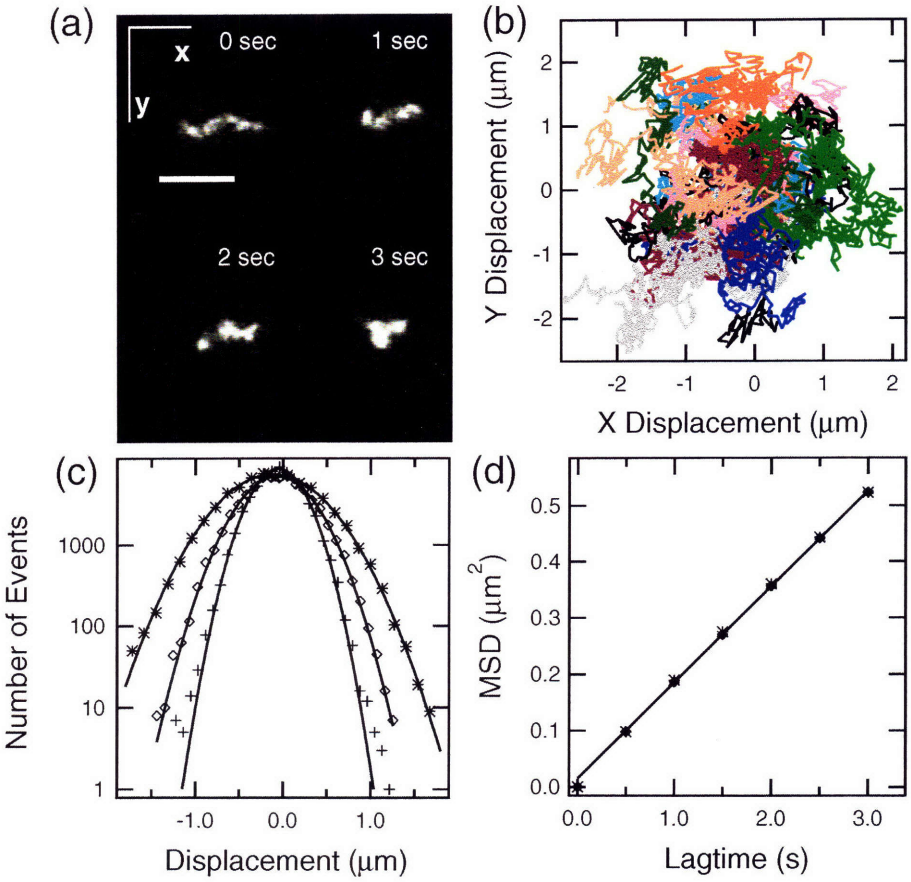

Fig. 3.2: *Summary of image analysis for 2λ-DNA in a 545 nm tall channel. (a) Time-series images from camera over four seconds (Δt = 1s) of a DNA movie (scale bar = 5.0 μm). (b) Center of mass trajectories for 28 2λ-DNA molecules. (c) Probability density functions (not normalized) for the trajectories at a lagtime of 0.33 (+), 0.66 (◇), and 1.23 (∗) seconds with accompanying fits to a Gaussian curve (solid lines). (d) Mean-squared displacement (MSD) (◇) and the variance of the probability density function (∗) as a function of lagtime. The two are identical in the limit of no net flow in the system. The MSD is fit to a line between lagtimes of 0.5 and 1.5 seconds (with a data point every 1/30 sec.), where short-time error associated with small displacements and the long time error associated with poor statistical information are minimized. The non-zero y-intercept of the fit to the MSD (solid line) is related to the image signal to noise [119].*

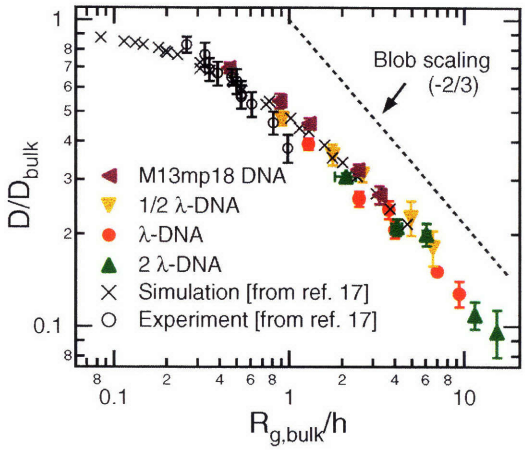

Fig. 3.3: *Curve collapse for all data plotted on normalized axes. Diffusivity is normalized by the bulk diffusivity, and the channel height by the bulk radius of gyration of the DNA. Also included is the simulation (×) and experimental (○) data from Chen et al. [101].*

deviation). Without separately analyzing the trends with channel height and molecular weight, it is impossible to know if the spread is due to experimental scatter or systematic deviation. By independently examining scalings of diffusivity with molecular weight and gap height, we are able to determine which assumptions used in scaling theories hold for this system and the regions where they break down.

Figure 3.4(a) shows diffusivity as a function of channel height for different DNA molecular weights. For complete curve collapse in Figure 3.3, the slopes in Figure 3.4 must be constant. In Figure 3.4(a) we see that the slopes systematically increase with increasing molecular weight. For the two largest DNA (λ and 2λ), the slopes are 0.55 ± 0.05 and 0.55 ± 0.06, respectively. These slopes should be compared to the blob theory scaling of 0.67. To within the precision of our data, it is difficult to say if the slope will continue to increase with increasing DNA molecular weight. To better understand this we must consider the limitations of blob theory. The bounds of the applicability of blob theory are set by the ability of the polymer to form blobs on the length scale set by h (which sets a lower limit on h) and having sufficient confinement of the polymer (which sets a lower limit on M_w and an upper limit on h). Experimentally, Reisner *et al.* [85] found that there was a drastic change in scalings of extension and relaxation times in channels approximately 110 nm square. They attribute the change in scalings to the onset of the Odijk regime, effectively setting the lowest conceivable bound on the channel heights to which blob theory can be applied for ds-DNA. Strikingly, this distance is only about twice the persistence length, which, when combined with the observed scalings for larger channels in ref. [85], brings into question whether the polymer is in a true blob-like conformation. In channels slightly larger than this bound, the blobs may be too small to contain enough chain to follow the long-chain scalings of blob size with the number of monomers due to excluded volume (EV) effects [55, 59]. In this regime, the number density of

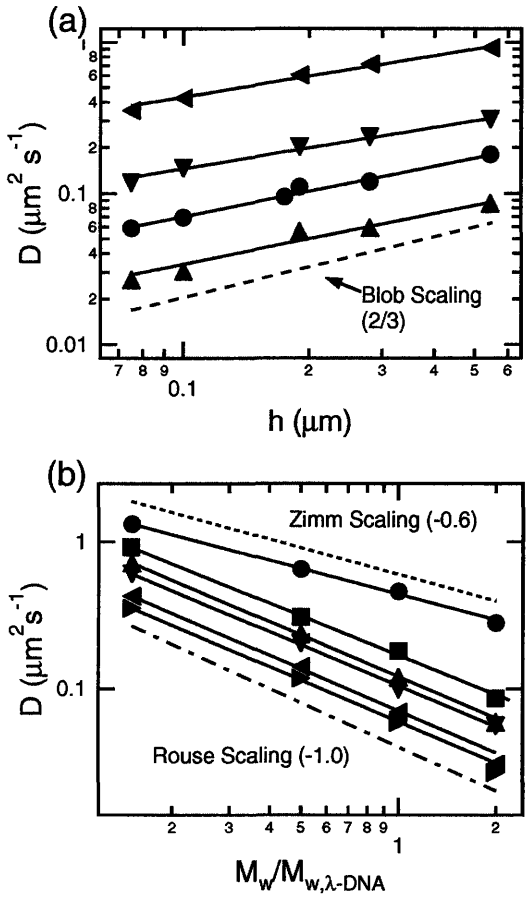

Fig. 3.4: *(a) Diffusivity versus channel height for different molecular weights. Solid lines are fits to the data, the dotted line is the slope expected for blob theory, and the error is less than the size of the symbols. The symbols correspond as follows:* ◀ *M13mp18 DNA,* ▼ $\frac{1}{2}\lambda$*-DNA,* ●λ*- DNA,* ▲ *2λ-DNA. The respective slopes are* $0.45 \pm .03$, 0.45 ± 0.04, 0.55 ± 0.05, 0.55 ± 0.06. *(b) Diffusivity versus molecular weight (M_w) relative to that of λ-DNA ($M_{w,\lambda-DNA}$). Solid lines are fits to the data, the dotted line is the scaling expected for Zimm hydrodynamics, the dash-dot line is the scaling expected for Rouse hydrodynamics. The symbols correspond as follows:* ● *bulk,* ■ *545nm,* ▲ *280nm,* ▼ *190nm,* ◀ *100nm,* ▶ *75nm. The respective slopes are the following:* -0.57 ± 0.01, -0.85 ± 0.04, -0.93 ± 0.05, -0.93 ± 0.06, -0.95 ± 0.07, -0.94 ± 0.07

monomers within each blob is small enough that the free energy increase due to internal repulsions of the chain is less than the thermal energy. Hence, the g-dependence (N-dependence in a coil) of

the second-virial term accounting for these interactions in Flory scaling theory is over-estimated and scalings of the blob size with g appear to be closer to θ-solvent scalings [55]. The concept of the "thermal blob" [55] is used to define the polymer size where the effects of EV can be considered to be in the long chain limit. For ds-DNA in our buffer conditions, this length scale (in terms of the radius of gyration of the thermal blob) is approximately $\zeta_T = \frac{4L_p^2}{\sqrt{6}w} \approx 0.8\mu$m where we use $L_p \approx 50$ nm and $w \approx 5$ nm (twice the Debye length for our buffer conditions) [55, 59]. This distance is larger than the channel heights investigated here, and may lead to different experimental scalings due to the fact that the internal structure of a blob is not correctly described in the theory (i.e. $\frac{1}{2} < \nu(g) < \frac{3}{5}$ and not $\approx \frac{3}{5}$ as assumed) especially in the smaller channels. Incorporation of these short chain effects on EV causes an increase in the theoretical slope of $\log(D)$ against $\log(h)$, which does not agree with our data. Setting $\nu = 0.5$ in the scaling of relaxation times and extensions with channel height, however, brings the theoretical scalings closer to the experimental results of Reisner *et al.* [85].

The other bound on the applicability of blob theory ensures that the polymer is moderately confined by setting the ratio of maximum channel height to minimum molecular weight. Hsu *et al.* [120] showed using Monte Carlo simulations that the "blob" conformation scalings cannot be expected to hold until $R_{g,bulk}/h \gtrsim 2$. We find, then, that the data collected in this study only brushes blob theory parameter space. The remaining assumption that the walls do not increase the drag on individual blobs should be examined if future experimental results cannot be brought into line with the theory [121, 122]. Also important to note, in both Figures 3.3 and 3.4(a), there is no dramatic change in trend at smaller channel heights even though our channels are in the range predicted for the onset of the Odijk regime [85].

Further experiments are needed to determine the exact cause of the discrepancy between the data presented here and the predictions of blob theory. A precise comparison of the complete theory may provide insight into physics at length scales on the order of the channel height and small time scales, which are not experimentally available for probing with our current experimental set up or with optical microscopy in general.

Shown in Figure 3.4(b) is diffusivity versus molecular weight for varying channel heights and bulk measurements. The bulk data and trend agree well with previous measurements [57, 101]. The molecular weight is normalized with that of λ-DNA as a convenient scaling factor and since λ-DNA has become a standard in single-molecule DNA studies. The scaling of diffusivity with molecular weight approaches Rouse scaling (-1.0) as the channel height is decreased, indicating hydrodynamic screening over the coil length of the polymer, in agreement with scaling theory (i.e. the exponents on M_w in eq 3.1 and eq 3.2 are indeed unity). This is the first experimental evidence showing that the effects of HI are negligible in describing coil behavior at channel heights only slightly smaller than the bulk radius of gyration of the polymer.

To investigate the crossover to Rouse-like behavior further, we chose a channel with a gap height ($h = 545$ nm) intermediate to the radii of gyration of available DNA and extended the molecular weight range with T4 DNA (see Figure 3.5). We compare the diffusion of DNA to an expression for the gap-averaged, in-plane diffusivity of a sphere between two plane walls [123].

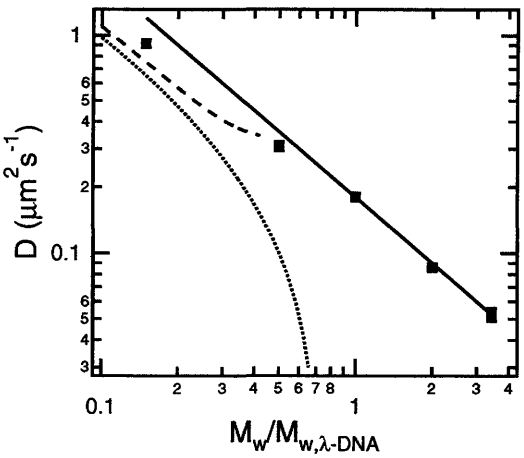

Fig. 3.5: *Diffusivity versus relative molecular weight in a 545 nm channel (points). The relative molecular weight where $R_{g,bulk} = h$ is $M_w/M_{w,\lambda-DNA} \approx 0.7$. Included are expressions for the gap-averaged, in-plane diffusion of a sphere in a slit pore (eq 3.4, dotted line), the local, in-plane diffusion of a sphere at the centerline of the channel (eq 3.5, dashed line), and Rouse scalings (solid line). The diffusivity at the centerline is plotted to the relative molecular weight where $2R_h/h \approx 1$, which already pushes the applicability of the theory, but after which there is a nonphysical upturn. DNA behavior smoothly transitions to free-draining behavior when $R_{g,bulk} \approx h$.*

$$\frac{D}{D_{bulk}} = \frac{\left(1 + \frac{9}{16}\left(\frac{2R_h}{h}\right)\ln\left(\frac{2R_h}{h}\right) - 1.19358\left(\frac{2R_h}{h}\right) + 0.4285\left(\frac{2R_h}{h}\right)^3 - 0.3192\left(\frac{2R_h}{h}\right)^4 + 0.08428\left(\frac{2R_h}{h}\right)^5\right)}{\left(1 - \frac{2R_h}{h}\right)} \tag{3.4}$$

where R_h is the hydrodynamic radius of the DNA defined by setting the Stokes-Einstein diffusivity equal to the Zimm diffusivity: $D_{bulk} = (k_bT)/(6\pi\eta R_h) = (0.203k_bT)/(\sqrt{6}\eta R_{g,bulk})$. This expression has been shown to be in excellent agreement with experimental results of spherical colloids in slit confinement, even in highly confining environments (i.e. $2R_h/h \gtrsim 0.8$) [123]. We compare to the diffusivity of a sphere because, in the large-channel limit, the hydrodynamic disturbance caused by the moving DNA molecule can be assumed to be in the far-field limit at the channel walls. In this case, information about the local structure of the DNA is lost and the disturbance is that of a sphere of radius R_h. Here, we can view the DNA as an effective sphere (i.e. coarse-grained to a single bead), and examine the increased drag on that sphere due to the presence of the walls. However, we see in Figure 3.5 that the expression falls well below the observed diffusivity of DNA. This underestimation could be due to the fact that the steric length scale of the polymer is greater

than its hydrodynamic length scale ($R_g > R_h$). This would tend to locate the DNA closer to the center of the channel than accounted for in eq 3.4. To check this, we compare the diffusion of the DNA to the diffusivity of a sphere midway between the two planes with the Faxén centerline approximation. This expression yields an upper bound for the diffusivity of a sphere in a slit channel [83].

$$\frac{D}{D_{bulk}} = 1 - 1.004\frac{2R_h}{h} + 0.418\left(\frac{2R_h}{h}\right)^3 + 0.210\left(\frac{2R_h}{h}\right)^4 - 0.169\left(\frac{2R_h}{h}\right)^5 \tag{3.5}$$

Since the derivation of this equation assumes far-field hydrodynamics, its applicability at high confinement is limited. For the smallest DNA in our study, $R_h/h \approx 0.5$ is still in the range where the centerline approximation is expected to hold, but the diffusivity is still slightly greater than predicted by eq 3.5. However, at low molecular weight, the overall trend tends toward sphere-like behavior.

As the molecular weight is increased and the DNA becomes more confined, diffusion follows Rouse scalings for polymers larger than λ-DNA. Using scaling arguments (i.e. $R_{g,bulk} \sim M_w^{0.6}$), the relative molecular weight where the channel height is equal to the bulk radius of gyration is $M_w/M_{w,\lambda\text{-}DNA} \approx 0.7$. To the precision afforded by the DNA used here, we find that for all chains where $R_{g,bulk} > h$, diffusivity scales linearly with molecular weight for a fixed value of h. This scaling directly confirms that intramolecular hydrodynamic interactions do not give rise to cooperative behavior over length scales governing molecular diffusion.

3.5.2 Hydrodynamic screening scaling analysis

Recently, colloidal experiments on the hydrodynamics in confined environments have yielded surprising results [113, 115]. The HI was found to have an inverse (or anti-drag) coupling in the transverse direction, originating from the far-field dipolar flow incurred by a point force in slit confinement [82]. Pair interactions were also found to be measurable over distances as far as an order of magnitude larger than the particle radius when the particle size was a substantial fraction of the channel height [113, 115]. It has also been shown in Q2D environments [112] that the average hydrodynamic force on a particle due to interparticle HI vanishes if the suspension is isotropically distributed. The complex and long-ranged interactions between colloids in slit confinement seem paradoxical when compared with the evidence of hydrodynamic screening presented here, and it is worthwhile to bring the two results into line.

We now present an argument for the scaling of the long-range hydrodynamic interactions with molecular weight. Our goal in this derivation is a general expression that can be used to determine whether hydrodynamic interaction is important at the length scale of the coil of a given polymer. The parameters in the expression are the rate of the algebraic velocity decay of the solvent due to a point force disturbance as well as the density of hydrodynamic interactions (i.e. the monomer distribution in space). These parameters are governed by both the geometry and the solvent quality. The final equation has been presented before in relation to electrophoresis [90], but the details of the derivation that provide its applicability to a variety of systems of interest are given below. The analysis will compare the drag on the chain induced by HI between chain segments and the single body effect of the drag on each segment. We evaluate the expression at the coil radius to determine whether or not HI effects can be neglected at that length scale. If so, we can coarse-grain the chain at a length scale smaller than the coil radius and use a local model (with no intra-chain HI)

to describe the polymer behavior at length scales larger than that of the coarse-graining. If so, diffusion is expected to follow Rouse scalings [58].

In the derivation that follows we will first consider, for the sake of an example, a bead-spring model of a Gaussian chain at equilibrium in Q2D. We assume the confined dimension is small enough that the conformation of the coarse-grained chain is strictly two-dimensional, and we use the HI interaction tensor for a Q2D geometry. This can be simulated, for instance, with modified spring forces that take into account the restricted phase space of the polymer [60, 61, 124]. We will use the convention where a tensor is denoted by an upper case letter in bold face font and a vector by a lower case letter in bold face font. For a coarse-grained model, the motion of the chain is described by the Langevin equation [58]

$$\frac{\partial \boldsymbol{r}_n}{\partial t} = \sum_{m=1}^{N} \boldsymbol{H}_{nm} \cdot \left(\boldsymbol{f}_m^B + \boldsymbol{f}_m^T + \boldsymbol{f}_m^E\right) \tag{3.6}$$

where $\boldsymbol{r}_n$ is the position of bead n, t is time, N is the total number of beads, $\boldsymbol{H}_{nm}$ is the hydrodynamic interaction tensor, and $\boldsymbol{f}_m^B$, $\boldsymbol{f}_m^T$, and $\boldsymbol{f}_m^E$ are the Brownian, tension, and external forces, respectively, on bead m. The tensor $\boldsymbol{H}_{nm}$ propagates those forces through the solvent and into a velocity of bead n. As mentioned above, since the interaction occurs through disturbances in the solvent, at far enough distances from the disturbance the form of the interaction must follow the far-field flow solutions for a point force. Here, we consider a Q2D geometry, where the third dimension is small compared to the radius of gyration of the polymer and can be coarse-grained into the bead-spring model. The form of the interaction tensor over distances greater than the channel height is of the form

$$\boldsymbol{H}_{nm} \sim \frac{1}{|\boldsymbol{r}_{nm}|^2}\left(\hat{\boldsymbol{r}}_{nm}\,\hat{\boldsymbol{r}}_{nm} - \frac{1}{2}\boldsymbol{I}\right)(1-\delta_{nm}) + \boldsymbol{A}_n\delta_{nm} \tag{3.7}$$

where $\boldsymbol{r}_{nm}$ is the vector from bead n to bead m, $\hat{\boldsymbol{r}}_{nm}$ is a unit vector in the direction of $\boldsymbol{r}_{nm}$, δ_{nm} is the Kronecker delta function, and $\boldsymbol{I}$ is the identity tensor. $\boldsymbol{A}_n$ is the self-mobility tensor of a single bead and would presumably depend on the position of the bead relative to the walls and the gap height [83]. In eq 3.6 we implicity use the linearity of the Stokes' equations to add the effects of the velocity disturbances from all of the other beads, resulting in a set of nonlinear and coupled equations. We therefore use a Zimm pre-averaging approximation [58] $\boldsymbol{H}_{nm} \Rightarrow \boldsymbol{H}_{nm,eq}$, where

$$\boldsymbol{H}_{nm,eq} = \int_0^\infty \int_0^{2\pi} \boldsymbol{H}_{nm}(|\boldsymbol{r}_{nm}|,\theta)\Psi(|n-m|;|\boldsymbol{r}_{nm}|,\theta)\,d|\boldsymbol{r}_{nm}|d\theta \tag{3.8}$$

and Ψ is the two-dimensional Gaussian probability distribution function for the distance between two beads separated by $|n-m|$ beads along the chain. We write the expression in polar coordinates to emphasize the orientational dependence of the tensor. After splitting the integral into the magnitude and orientational parts, we obtain

$$\boldsymbol{H}_{nm,eq} \sim \int_0^\infty \frac{1}{|\boldsymbol{r}_{nm}|^2}\left(\frac{3}{2\pi|n-m|L_p^2}\right)\exp\left(\frac{-|\boldsymbol{r}_{nm}|^2}{2|n-m|L_p^2}\right)|\boldsymbol{r}_{nm}|\,d|\boldsymbol{r}_{nm}| \int_0^{2\pi}\left(\hat{\boldsymbol{r}}_{nm}\,\hat{\boldsymbol{r}}_{nm}-\frac{1}{2}\boldsymbol{I}\right)d\theta\,(1-\delta_{nm})+\boldsymbol{A}_n\delta_{nm} \quad (3.9)$$

We note that the integral over θ vanishes due to the symmetry of the interaction tensor and the isotropy of the Gaussian distribution. Tlusty [125] followed a similar derivation to attain this result and extended the analysis to slits where the floor and ceiling are not perfectly parallel planes. Physically, the cancellation amounts to a many-body cancellation effect in an isotropic system, yielding a system with no net force due to HI [112]. We note that there may be interesting conformational repercussions due to incomplete cancellations at the outer "edge" of the polymer coil under a steady external force.

We continue with this analysis, however, noting the fact that the instantaneous conformation of the polymer is not isotropic [126, 127]. However, above we have ensemble averaged many anisotropic configurations and used the isotropy of the resulting distribution to cancel hydrodynamic interactions by symmetry. The argument for hydrodynamic screening can be made stronger if it can be shown that the decay of the velocity *magnitude* is sufficient to screen hydrodynamic interactions. In the following, we will assume that the interactions have no orientational dependence. Now, the direction of the resultant velocity of bead n due to HI with bead m is the same as the direction of the force on bead m. We examine the scenario with the highest possible amount of directional cooperativity between monomer units. The pre-averaged interaction tensor becomes

$$\boldsymbol{H}_{nm,eq}(r) \sim \int_0^\infty \frac{1}{r^2}\left(\frac{3}{2\pi|n-m|L_p^2}\right)\exp\left(\frac{-r^2}{2|n-m|L_p^2}\right)r\,dr\,\boldsymbol{I}(1-\delta_{nm})+\boldsymbol{A}_n\delta_{nm} \quad (3.10)$$

where $r = |\boldsymbol{r}_{nm}|$. Since we are concerned mainly with large length scale behavior, the local behavior described in the detailed form of $\boldsymbol{A}_n$ is not of importance. For simplicity, we take $\boldsymbol{A}_n$ to be isotropic (i.e. $\boldsymbol{A}_n = A_n\boldsymbol{I}$). Equation 3.10 then simplifies to

$$\boldsymbol{H}_{nm,eq} = H_{nm,eq}\boldsymbol{I} = \int_0^\infty \left[H(r)\Psi(|n-m|,r)\,dr\,(1-\delta_{nm})+A_n\delta_{nm}\right]\boldsymbol{I} \quad (3.11)$$

where $H(r)$ is the magnitude dependence of the interaction tensor $\boldsymbol{H}_{nm}$ and $\Psi(|n-m|,r)$ is still the same Gaussian bead distribution function, but it is stressed that there is no angular dependence. We now insert eq 3.11 into eq 3.6 in the place of the non-preaveraged interaction tensor, and average over all beads n to obtain a center of mass velocity

$$\frac{1}{N}\sum_{n=1}^{N}\frac{\partial \boldsymbol{r}_n}{\partial t} = \boldsymbol{v}_{cm}(t) \sim \frac{1}{N}\sum_{n=1}^{N}\sum_{m=1}^{N}\boldsymbol{H}_{nm,eq}(r)\cdot\left(\boldsymbol{f}_m^B+\boldsymbol{f}_m^T+\boldsymbol{f}_m^E\right) \quad (3.12)$$

Taking the equilibrium average of eq 3.12 causes the Brownian and tension forces to vanish. Calling upon the isotropy of the modified interaction tensor (eq 3.11), the dot product can be cancelled and the surviving terms are the following

$$\langle \boldsymbol{v}_{cm}(t)\rangle_{eq} \sim \frac{1}{N}\sum_{n=1}^{N}\sum_{m=1}^{N} H_{nm,eq}(r)\boldsymbol{f}_m^E \tag{3.13}$$

By analogy to the expression for the drag on the chain, $\xi_{chain}\langle \boldsymbol{v}(t)\rangle_{eq} = N\boldsymbol{f}_m^E$, we can write [128]

$$\frac{1}{\xi_{chain}} \sim \frac{1}{N^2}\sum_{n=1}^{N}\sum_{m=1}^{N}\left(\int_0^{\infty} H(r)\Psi(|n-m|,r)\,dr\,(1-\delta_{nm}) + A_n\delta_{nm}\right) \tag{3.14}$$

The second term can be written in terms of an average (scalar) mobility of a single bead. We note that the first term in the expression is not explicitly dependent on either n or m, but only on their difference. In the long-chain limit, end effects are not important and the expression is not dependent on the position of bead n along the chain. We can then write the double sum as a single sum $\sum_{n=1}^{N}\sum_{m=1}^{N} \Rightarrow N\sum_{n-m=1}^{N}$. Exchanging the order of summation and integration we obtain a direct sum of the pair probability distribution function over all beads, which is the pair correlation function [129]. The expression for the drag becomes

$$\frac{1}{\xi_{chain}} \sim \frac{1}{N}\left(\int_{L_p}^{L_pN^{\nu}} H(r)g(r)dr + \langle A_n\rangle\right) \tag{3.15}$$

where $g(r)$ is the pair-wise correlation between monomers and ν is the Flory-Edwards exponent. We have altered the limits of integration to reflect the fact that we are most concerned with HI effects at the length scale of the coil. Also, $g(r)$ is known to decay sharply to zero for r greater than the coil dimension [130], so to within a scaling approximation, the majority of the interactions are accounted for within the integral. We take the lower limit of the integral to be the smallest statistically independent step length of the polymer (a persistence length). This limit describes the effects of HI at the local level and does not appear (except as a prefactor) in the scaling analysis. The integral represents all of the pair-interactions between monomers through the solvent (i.e. the off-diagonal elements of the interaction tensor) from local effects (lower limit) to coil-length effects (upper limit). The second term represents the drag on an individual bead (i.e. the diagonal components of the interaction tensor). Eq 3.15 has been obtained by Long *et al.* [90] though details were not given which allow one to follow the assumptions leading to this expression. Since we are concerned with long length scale and far field effects, we are concerned primarily with the behavior in the limit of large N. If the integral evaluated at the upper limit dominates in the limit of large N, the motion is cooperative and HI is not screened. If the integral evaluated at the upper limit vanishes in the limit of large N, then the motion of polymer segments can be treated as independent at a length scale smaller than R_g. Therefore, a model can be devised using only *local* effects (i.e. $\xi_{chain} \sim N$) by coarse-graining the chain at a length scale larger than this hydrodynamic screening length and smaller than that of the coil. We can now use scaling assumptions [130] to express the dependence of $g(r)$ on r, and then insert this into eq 3.15 to find the effect of the

Condition	ν	$H(r)$	$g(r) \sim N/r^d$	$\int H(r)g(r)dr$	$\langle \xi_{chain} \rangle_{eq}$	model type	α
3d ideal chain	1/2	$1/r$	$1/r$	$N^{1/2}$	$N^{1/2}$	non-local	$\alpha > 2$
Q2d ideal chain	1/2	$1/r^2$	const	$ln(N)$	$N/\ln(N)$	non-local	$\alpha > 2$
3d (SAW)	3/5	$1/r$	$1/r^{4/3}$	$N^{2/5}$	$N^{3/5}$	non-local	$\alpha > 5/3$
Q2d (SAW)	3/4	$1/r^2$	$1/r^{2/3}$	$N^{-1/2}$	N	local	$\alpha > 4/3$
3d rod	1	$1/r$	$1/r^2$	$ln(N)$	$N/\ln(N)$	non-local	$\alpha > 2$

Table 3.2: *Summary of scaling results. ν is the Flory exponent, d is the dimensionality (2 or 3), and α describes the range of the applicability of a local model at large N if $H(r) \sim 1/r^\alpha$*

long-ranged HI.

The application of eq 3.15 for several case studies of solvent quality and dimensionality are summarized in Table 3.2. For each condition, there are two important pieces of required information: the rate of velocity decay ($H(r)$) and the pair-wise correlation function of the polymer ($g(r)$). For the geometries at hand, these scalings are readily available or calculable [130, 131]. Evaluation of the integral in eq 3.15 determines the strength of the hydrodynamic interactions between the beads. In particular, the value of this integral evaluated at the upper limit reflects the importance of long-range intrachain HI. In polymer physics, screening is typically said to take place if the chain can be replaced by a series of non-hydrodynamically interacting segments such that $\xi_{chain} \sim 1/N$. For this to occur, the integral evaluated at the upper limit must be $O(1)$ or vanish in the limit $N \to \infty$. Comparison of this interaction to the drag inflicted by each individual bead at large N determines whether or not HI is important in the dynamics of the chain. HI can be considered unimportant in cases where the interaction between beads decays at large N. A "local" model, which takes into account only the drag on individual beads, can then be employed to model the polymer. For the three-dimensional cases, our results are in accord with known scalings. For example, for an ideal polymer (theta conditions) in 3d (unconfined) the upper limit of the integral in eq 3.15 is the dominant contribution to the drag and we recover the well-known result that drag scales as $N^{1/2}$ and not as N.

The Q2D results point to the fact that HI are dependent not only on the form of the velocity decay, but also the monomer distribution. It is often cited that a velocity decay alone is sufficient information to qualify a system as hydrodynamically screened, but we see in Table 3.2 that this is not the case. The distribution of the monomers (dependent on the solvent quality) plays a large role in the resulting dynamics of the chain. For a polymer in a θ-solvent in Q2D, the velocity decay is not sufficient to prevent cooperative behavior (though the effect is only logarithmic), while for a polymer in good solvent in the same geometry the decay alone does suffice. We have shown that the magnitude decay of the velocity field alone is sufficient to cause hydrodynamic screening over equilibrium conformations of polymers in good solvents in Q2D environments.

We should note that hydrodynamic screening in confinement has been shown before. Bakajin *et al.* [102] showed hydrodynamic screening by comparison to a model based on a hydrodynamic screening length on the order of the persistence length of the polymer. Rädler *et al.* [107] showed hydrodynamic screening of DNA confined to two dimensions in a cationic bilayer directly next to

a solid surface. In short, previous experiments have focused on the screening of hydrodynamics at length scales comparable to the persistence length. While information at these small scales is important, applications concerned with the use of confinement to control the dynamics of a single molecule require information at the scale of the coil as well. We have shown that a significant coil-scale behavioral change to free-draining occurs in slit confinements that are very close to the bulk radius of gyration of the coil.

3.6 Conclusion

We use the precision and control of microfabrication techniques, biological macromolecules, and single molecule microscopy to perform systematic experiments of DNA diffusion in slit confinement. Separate analysis of the trends with channel height and molecular weight allows interrogation of different portions of confinement theories. Scalings of diffusivity with channel height do not agree well with existing theories, but the polymers here may be too short (and therefore must be confined to gaps that are too small compared to the persistence length and the thermal blob size) to allow a full comparison to the theory. Scalings with molecular weight directly show intramolecular hydrodynamic interactions in DNA solutions are screened when the channel height is smaller than the bulk radius of gyration. A scaling theory shows that both an orientational average and sole consideration of the algebraic decay of the hydrodynamic interactions can lead to free-draining like behavior in Q2D systems. The derivation also shows that information about the decay of the solvent velocity due to a disturbance is not sufficient to determine whether HI can be neglected at the coil's length scale, information about the spatial distribution of the hydrodynamic centers (i.e. solvent quality and spatial geometry) is needed as well.

Experimental studies of fundamental polymer physics require a significant level of detail in the results, even to test scaling predictions. Here, the use of DNA eliminates uncertainty due to molecular weight polydispersity and enables the use of direct visualization to quantify the motion of an individual polymer. The use of micro- and nano- fabrication techniques enables precise control of the channel dimensions and geometry. This increased control allows the design of experiments to test very specific hypotheses, which is ideal for fundamental studies. Furthermore, these slit-like geometries are important motifs in emerging lab-on-chip devices [25, 132].

CHAPTER 4

Dynamics in Confinement and Blob Theory

Given that the scaling of diffusivity with channel height varies significantly from that predicted by blob theory, a full experimental characterization of the conformation and dynamics in slit-like channels was carried out. Accurate measurement of the relaxation time, especially, requires significantly better statistics due to the fact that we are now very concerned with the time correlation of fluctuations of the chain. To achieve this measurement, a new protocol was developed which incorporates an enzymatic oxygen scavenging system in the experimental buffer (the presence of oxygen has been linked to DNA photobleaching and breakage). Scalings of the relaxation time, diffusivity, and polymer conformation (end to end distance or radius of gyration) with molecular weight and channel height are investigated. We find that not only is the blob theory assumption concerning long length scale hydrodynamics correct, but also that the measured conformation of the polymer is in agreement with that predicted by the theory. The reason for the discrepancy observed previously, then, is a fault in the remaining assumption, that hydrodynamics within blobs are not affected by the presence of the channel walls. As will be seen below, this chapter provides a complete characterization of DNA diffusivity and relaxation time at equilibrium in confinement, which are very important parameters for the design of devices and predictions of DNA behavior in those devices.

4.1 Overview

The longest relaxation time (τ_1) of DNA confined in nanoslits is characterized, and its dependence on molecular weight (M) and channel height (h) is investigated. The relaxation time is extracted from the rotational autocorrelation function obtained from time-sequence images of confined DNA at equilibrium using fluorescence microscopy. We find that $\tau_1 \sim M^{2.45}h^{-0.92}$, in partial agreement with the predictions of the blob theory ($\tau_1 \sim M^{5/2}h^{-7/6}$). The experimental results suggest that the assumptions of both a 2-dimensional self-avoiding walk of blobs and a 3-dimensional self-avoiding walk of polymer segments within blobs are valid, while the assumption of non-draining blobs is compromised. We also find $(\tau_1/\tau_{1,bulk}) \sim M^{0.1}(R_{g,bulk}/h)^{0.92}$ where $\tau_{1,bulk}$ is the bulk relaxation time and $R_{g,bulk}$ the bulk radius of gyration. Because of the very weak M dependence in above scalings, a master plot of $(\tau_1/\tau_{1,bulk})$ versus $(R_{g,bulk}/h)$ is constructed, and is used to compare our results to other studies. The plot also provides a convenient way to estimate the relaxation time of DNA in varying degrees of confinement. Using the measured relaxation time and blob theory, we explain recent observations that a very large shear rate is required to deform DNA when it is confined to channels with a dimension comparable to or smaller than the bulk radius of gyration.

4.2 Introduction

With the development of nanotechnology, new applications have been created for separating and manipulating biomolecules with nanodevices[25, 45, 46, 85, 95, 133, 134]. It is therefore essential to understand the underlying physics and transport properties of highly confined macromolecules. Such knowledge will not only be important for the development of polymer physics, but also could help the design and optimization in future applications such as separations and drug delivery.

Slit-like nanochannels with well controlled dimensions and properties have served as a platform for systematic investigation of the dynamics of confined biomolecules[25, 135]. Such channels can be fabricated with standard microlithography techniques[94] and can have one dimension small enough to substantially change the behavior of macromolecules. The dynamics of a polymer confined in a slit and a circular tube has been predicted by de Gennes and coworkers[79, 80, 81] using blob theory. The theory describes a confined polymer as a string of blobs with diameters equal to the smallest dimension of the confinement, and yields predictions for the scaling of the polymer equilibrium extension, diffusivity, and the longest relaxation time as a function of polymer molecular weight, chain rigidity, and the degree of confinement. In addition to blob theory, Odijk[84] proposed a deflection chain picture to describe the dynamics of a stiff chain confined in a circular tube with the diameter much smaller than its persistence length, b. Although both theories have existed for decades, they have only recently begun to be tested experimentally in well defined geometries.

Several experimental and simulation studies have investigated the dynamics of DNA confined in rectangular channels [85, 95, 121, 136]. Jendrejack et al.[121, 136] used Brownian dynamics (BD) with a bead-spring model to simulate DNA behavior in a square channel. An excluded volume force was used to mimic the good solvent condition. Both intramolecular and wall-molecule hydrodynamic interactions were included in the simulations. Although the study focused on shear-induced migration of DNA, the dependence of the equilibrium extension of DNA ($\langle x \rangle_0$) and the longest relaxation time (τ_1) on the channel size (h) were also examined. They found that $\langle x \rangle_0 \sim h^{-2/3}$ and $\tau_1 \sim h^{-1/3}$, in agreement with the predictions from blob theory. In an experimental study, Tegenfeldt et al.[95] showed that DNA were highly extended at equilibrium in nearly square

nanochannels, and their equilibrium extensions were found to be proportional to the molecular weight, again in agreement with blob theory. In a later experimental study, Reisner et al.[85] determined the scaling of the longest relaxation time and equilibrium extension of DNA versus the size of square nanochannels. The longest relaxation times of DNA were extracted from a single exponential fit to the decay of the autocorrelation function of the DNA extension. A strong transition was observed both in the scalings of τ_1 and $\langle x \rangle_0$ with h around $h \approx$140nm, roughly corresponding to twice of the persistence length of DNA. The experimental results were compared against the predictions given by blob theory for $h > 2b$ and those inferred from the deflection chain model[84] for $h < 2b$. However, only a qualitative agreement was reached. Odijk[137] recently developed a theory to predict DNA extension at equilibrium in circular, square, and rectangular nanochannels. Both the bending free energy that rises from the molecular elasticity, and the entropic free energy that rises from the reduction of the orientational and translational degree of freedom of molecule were taken into account in this theory. The predicted DNA stretches were close to those reported by Reisner et al.[85] and Jo et al.[46]. However, it was noted that the prediction given for DNA extension in a rectangular channel will not be valid for DNA in very wide nanoslits because the assumption of small lateral fluctuations of DNA is not satisfied.

The relaxation behavior of DNA confined in a well-defined slit-like structure was first observed by Bakajin et al.[92]. In this pioneering study, T4-DNA were hooked on obstacles and stretched electrohydrodynamically in small slits with heights of $5\mu m$, 300nm and 90nm. Their relaxation behavior was observed after DNA disengaged from the obstacles, and was found to be slower in shallower channels. However, the quantitative values of DNA relaxation time were not provided. Stigter[138] and Woo et al.[124, 139] performed Brownian dynamics simulations and reported satisfactory results comparing to those of Bakajin et al., but no comparison was made against the prediction of blob theory. Recently, Randall and Doyle [15, 140] and Randall[14] reported relaxation times of λ-, 2λ- and T4-DNA in $2\mu m$ high slits. The relaxation time of confined T4-DNA (with bulk radius of gyration ($R_{g,bulk}$) of approximately $1.5\mu m$) was found to be almost double its bulk value.

The blob theory prediction of the scaling of τ_1 of polymers confined in a slit was examined by Hagita et al.[141] using dynamic Monte Carlo simulation with the bond fluctuation model. They found in good solvent τ_1 scales as $M^{2.5}$, and the relaxation spectrum follows the same scaling down to the size of a blob. These findings are in agreement with blob theory[81]. Although the study did not consider hydrodynamic interactions, the results are still inspiring because blob theory also assumes no hydrodynamic interaction between blobs.

Chen et al.[142] simulated DNA conformation and diffusion in slits using the method of Jendrejack et al.[121]. The same study also reported experiments of DNA diffusivity in slit-like channels with $0.3 < (R_{g,bulk}/h) < 1$. The simulations confirmed that the equilibrium DNA stretch is proportional to the (-1/4) power of the slit height as predicted by blob theory. In addition, the simulations and experimental results for DNA diffusivity in different degrees of confinement agreed well with each other, and were close to the prediction of blob theory. Usta et al.[143] employed the Lattice Boltzmann method to simulate the confined polymer dynamics. Their results for diffusion of confined polymers in slit channels were essentially the same as those of Chen et al.[142]. However, when we scrutinize the results of Chen et al.[142] and Usta et al.[143], it is clear that the dependence of diffusivity on the slit height is weaker than that predicted by blob theory.

Balducci et al.[144] measured the diffusivity of DNA in nanoslits over a much wider range of conditions $0.4 < (R_{g,bulk}/h) < 15$. The diffusivity was found to vary inversely with molecular

weight when the channel height is smaller than $R_{g,bulk}$. This scaling follows exactly the blob theory prediction and suggests complete screening of hydrodynamic interactions between blobs. A scaling analysis was provided to explain why the algebraic decay of the far-field hydrodynamic interaction is sufficient to eliminate large-length scale hydrodynamic cooperativity in the dynamics of quasi-two-dimensional polymers in good solvents. The scaling of DNA diffusivity with channel height was also investigated in detail. The dependence of DNA diffusivity was weaker than the blob theory prediction. In contrast to Reisner et al.[85], no drastic change in DNA diffusivity was observed when the height of slits approached the persistence length of DNA.

After surveying previous work, we find the relaxation behavior of a polymer confined in slit-like geometry has not been quantitatively investigated in experiments. The longest relaxation time of a polymer is fundamentally important because it defines the natural time constant of the molecule and characterizes how fast a polymer can react in response to an imposed flow. An important example is that a polymer will not appreciably deform from equilibrium until Weissenberg ($Wi = \tau_1\dot{\gamma}$) approaches 1[145]. Here $\dot{\gamma}$ is the strain rate, and can be either shear rate or elongation rate. Moreover, by determining the dependence of τ_1 and D on molecular weight and channel height, we can also investigate the effect of hydrodynamic interactions on the dynamics of a polymer in confinement. The goal of this study is to provide an accurate measurement of the longest relaxation time of DNA confined in slits, and to test the applicability of de Gennes' blob theory for this scenario.

4.3 Scaling arguments for polymer dynamics in a slit

We consider a linear polymer with a persistence length b and a contour length Nb confined in a slit-like channel with height h smaller than the natural size of the chain but larger than b. Note that N is proportional to M, so we treat them as interchangeable variables in scaling expressions. de Gennes [79, 80] has described the behavior of such a chain using the blob picture. In the good solvent limit, de Gennes assumed: (1) the chain can be thought of as a string of blobs with each blob having a diameter h, (2) these blobs are confined in the slit so their configuration follows a 2D self-avoiding walk (SAW), (3) there are no hydrodynamic interactions between blobs, (4) chain segments within blobs are not aware of the presence of the confinement and behave as if they were under a 3D, non-confined condition. Therefore, segments within a blob will follow a 3D SAW, and interact hydrodynamically.

Following the above assumptions, the number of polymer segments g in each blob can be estimated using a simple geometrical argument:

$$g \sim \left(\frac{h}{b}\right)^{1/\nu_{3d}} \simeq h^{\frac{5}{3}} b^{-\frac{5}{3}} \tag{4.1}$$

where ν_{3d} is the Flory-Edwards exponent [108]. Throughout this study, we use '$\sim$' to indicate that two quantities are proportional to each other, '$\approx$' to indicate a numerical approximation to the quantity, and '$\simeq$' to indicate that ν_{2d} and ν_{3d} have been substituted with their ideal values of 3/4 and 3/5[79, 80, 81, 108], respectively. Although a more accurate value of $\nu_{3d} = 0.588$ has been obtained using renormalization group theory[58], we follow de Gennes and use $\nu_{3d} = 3/5$ in all our derivations. We will discuss the influence of using $\nu_{3d} = 0.588$ instead of $\nu_{3d} = 3/5$ in a later section. The scaling of the nominal size R of a confined chain can be derived using the assumption

of a 2D SAW of blobs, and can be expressed as:

$$R \sim h\left(\frac{N}{g}\right)^{\nu_{2d}} \sim N^{\nu_{2d}} h^{\frac{\nu_{3d}-\nu_{2d}}{\nu_{3d}}} b^{\frac{\nu 2d}{\nu_{3d}}} \simeq N^{\frac{3}{4}} h^{-\frac{1}{4}} b^{\frac{5}{4}} \tag{4.2}$$

Eq 4.2 can also be obtained from Flory theory by minimizing the free energy of a SAW chain confined in a slit [55, 146]. The N and h dependence in Eq 4.2 has been verified by ten Brinke and coworkers using Lattice Monte Carlo simulation[147] and by Chen et al.[142] using bead-spring Brownian dynamics simulations.

In addition to the static behavior, dynamic properties of a confined chain can also be derived. To obtain the scaling of the longest relaxation time, we consider the force balance on a chain. The elastic force $F_{elastic}$ required to stretch a polymer from its equilibrium size R to $R + \delta$R has been shown by de Gennes that [81, 146, 148]

$$F_{elastic} = -\frac{k_B T}{R^2}\delta R \tag{4.3}$$

where k_B is the Boltzmann constant. Notice the excluded volume effect has been included in R. The drag force F_{drag} applied by the solvent balances the elastic force, and can be estimated:

$$F_{drag} = \zeta_{chain}\delta\dot{R} \tag{4.4}$$

where ζ_{chain} is the drag coefficient of the entire chain. $\delta\dot{R}$ is the time rate of change of δR. Equating these two forces leads to:

$$\delta\dot{R} = -\frac{k_B T}{\zeta_{chain} R^2}\delta R = -\frac{\delta R}{\tau_1} \tag{4.5}$$

where the longest relaxation time is:

$$\tau_1 = \frac{\zeta_{chain} R^2}{k_B T} \tag{4.6}$$

Since hydrodynamic interaction is assumed to dominate within a blob, the drag coefficient of the chain is described by:

$$\zeta_{chain} \sim \zeta_{blob} N_{blob} \sim h\left(\frac{N}{g}\right) \sim N h^{\frac{\nu_{3d}-1}{\nu_{3d}}} b^{\frac{1}{\nu_{3d}}} \simeq N h^{-\frac{2}{3}} b^{\frac{5}{3}} \tag{4.7}$$

Substituting Eqs 4.2 and 4.7 into Eq 4.6, Brochard [81] has shown the scaling of the longest relaxation time τ_1 versus N, h, and b to be:

$$\tau_1 \sim N^{2\nu_{2d}+1} h^{3-\frac{2\nu_{2d}+1}{\nu_{3d}}} b^{\frac{2\nu_{2d}+1}{\nu_{3d}}} \simeq N^{\frac{5}{2}} h^{-\frac{7}{6}} b^{\frac{25}{6}} \tag{4.8}$$

The scaling of diffusivity D can be written as:

$$D \sim \frac{k_B T}{\zeta_{chain}} \sim N^{-1} h^{\frac{1-\nu_{3d}}{\nu_{3d}}} b^{-\frac{1}{\nu_{3d}}} \simeq N^{-1} h^{\frac{2}{3}} b^{-\frac{5}{3}} \tag{4.9}$$

This scaling of D with N has been confirmed in our previous study[144]. However, the measured D showed a weaker dependence on h than predicted by Eq 4.9.

We now consider another extreme case where the hydrodynamic interactions vanish even within blobs. The overall drag coefficient of a chain is then

$$\zeta_{chain} \sim \zeta_b N \tag{4.10}$$

where ζ_b is the drag coefficient of a single segment. While ζ_b should be a function of h, we treat it as a constant because the typical width of a molecule (about 2nm for a double-strained DNA) is much smaller than the slit heights considered in this study[83]. Using the same analysis as we have used to obtain Eqs 4.8 and 4.9, we reach

$$\tau_1 \sim N^{2\nu_{2d}+1} h^{\frac{2\nu_{3d}-2\nu_{2d}}{\nu_{3d}}} b^{\frac{2\nu_{3d}-2\nu_{2d}}{\nu_{3d}}} \simeq N^{\frac{5}{2}} h^{-\frac{1}{2}} b^{\frac{5}{2}} \tag{4.11}$$

$$D \sim N^{-1} \tag{4.12}$$

The N and h dependence of Eq 4.11 has been verified by Milchev and Binder[149], and Hagita et al. [141] using Bond fluctuation Monte Carlo simulations. For convenience, we will refer to Eqs 4.8 and 4.9 as *Zimm-blob* scaling, and Eqs 4.11 and 4.12 as *Rouse-blob* scaling.

Comparing experimental results with the predicted scalings, we should be able to verify the assumptions made in blob theory. For example, using the experimental scaling of $D \sim N^{-1}$ alone, one can readily infer that hydrodynamic interaction is screened between blobs[144]. However, it is not as straightforward to verify other assumptions because the dependence of D and τ_1 with N and h is usually a convolution of several assumptions. Therefore, we rearrange the above equations so individual assumptions can be independently examined. We find that although both D and τ_1 depend on ζ_{chain}, their product is independent of ζ_{chain} and is only a function of R:

$$D\tau_1 \sim R^2 \sim N^{2\nu_{2d}} h^{\frac{2(\nu_{3d}-\nu_{2d})}{\nu_{3d}}} \simeq N^{\frac{3}{2}} h^{-\frac{1}{2}} \tag{4.13}$$

Therefore, we can calculate the experimental value of ν_{2d} ($\nu_{2d,exp}$) from the scaling of $D\tau_1$ with N, and subsequently estimate the experimental value of ν_{3d} ($\nu_{3d,exp}$) from the scaling of $D\tau_1$ with h. Once $\nu_{2d,exp}$ and $\nu_{3d,exp}$ are known, we can substitute them back to Eqs 4.8, 4.9, 4.11 and 4.12 to infer the expected dependence of τ_1 and D on h, and to verify the assumption of dominating hydrodynamic interactions in blobs.

4.4 Longest relaxation time for polymer molecules

It is worthwhile to briefly review the definition of the longest relaxation time of a polymer chain in dilute solutions. For a polymer chain in either theta or good solvent, both Rouse and Zimm models predict that the longest conformational relaxation time ($\tau_{1,c}$) and the longest rotational relaxation time ($\tau_{1,r}$) are equal, while the longest stress relaxation time ($\tau_{1,s}$) is half of $\tau_{1,c}$[55, 58]. Here $\tau_{1,c}$ can be defined by the ratio of the drag coefficient to the spring constant of the first normal coordinate. $\tau_{1,r}$ can be defined by the inverse of the dominating exponential decay rate of the autocorrelation function of the end-to-end vector of a chain. In single-molecule experiments using fluorescence microscopy, $\tau_{1,s}$ of DNA in bulk solutions is typically obtained by fitting the decay of the mean squared stretch of an initially extended chain to a single exponential in the linear

regime[15, 48, 51, 140, 150]. This method has been widely used because it requires relatively small ensembles due to the large perturbation from equilibrium. On the other hand, $\tau_{1,c}$ and $\tau_{1,r}$ are difficult to measure in bulk solutions because one needs to collect data over larger ensembles of many relaxation times to extract the time constant, but a molecule can stay in focus only for a short period of time. However, the rotational relaxation time of so called type-A polymer that carries a molecular dipole parallel to its end-to-end vector can be measured by dielectric spectroscopy[151]. In most single-molecule studies, $\tau_{1,s}$ is implicitly designated as the longest relaxation time. Therefore, we follow this tradition in the current study to avoid possible ambiguity.

4.5 Experiments

4.5.1 Channel and DNA preparation

The nanoslits used in this study were made with glass using the method described in Mao and Han [94]. The slits are 150μm wide and 92nm to 760nm high. Their heights were determined from SEM images. The DNA samples used are λ-DNA halfmers (1/2λ,24.25$\pm$0.25kbp),λ-DNA (λ, 48.5kbp), λ-DNA dimers (2λ, 97kbp), T4GT7-DNA (T4, 165.6kbp) and a bacterial artificial chromosome (BAC) clone (12M9) (185kbp). λ-DNA were purchased from New England Biolabs (NEB). λ-DNA halfmers were made by digesting λ-DNA with XbaI restriction enzyme(NEB). λ-DNA dimers were made using an oligoprotected ligation[116]. T4GT7-DNA were purchased from Nippon Gene. BAC-DNA were donated by U.S. Genomics. DNA samples were stained with YOYO-1 fluorescent dye (Molecular Probes) overnight at room temperature at a concentration of 1 dye molecule every 4 base pairs. DNA samples were diluted 2- to 10-fold immediately before experiments to reach an optimal concentration for observation. The experimental buffer is 0.5X TBE (Tris-Borate-EDTA) solution with an oxygen scavenger system consisting of 4% β-mercaptoethanol (CabioChem), 7.26 mg/ml β-D glucose, 0.37 $\mu l/ml$ catalyse (Roche) and 0.16 mg/ml glucose oxidase (Roche). The buffer viscosity η_s is 1.075 centipoise (cp) at 22°C, 13.3% higher than water viscosity measured at the same temperature. The viscosity was determined using microrheology by measuring the diffusivity of 0.925μm polystyrene beads (Polysciences). Nanochannels were filled the night before experiments with 0.5X TBE buffer, and flushed by an electroosmosis flow at a field of 10V/cm to remove bubbles and any residual chemicals left from the fabrication process. The flushing buffer was replaced with the experimental buffer two hours before experiments. A low electric field was used to prevent ion polarization in the channel[152]. DNA were driven into the channel using a field of approximately 30V/cm.

4.5.2 Image acquisition and analysis

We observed single DNA molecules using an inverted Zeiss Axiovert 200 microscope with a Plan-Apochromat 100X(N.A. 1.40) oil-immersed objective. The images were taken with a Hamamatsu EB-CCD camera (model:7190-21) at the rate of 30 frames/sec for all experiments except for T4-DNA and BAC-DNA (15 frames/sec due to their long relaxation times). With our setup, one pixel represents 0.135μm. 3600 frames were collected for each molecule. Averages were taken over ensembles containing 20 $\sim$ 35 molecules. Images were processed using custom-developed code in Interactive Data Language(IDL). The background signal was subtracted from the image before the analysis. With the assumptions that the dyes are evenly distributed along the backbone of a DNA

and the the camera gain is a linear function of the fluorescent signal, the fluorescent intensity in a pixel is proportional to the total mass of DNA in that pixel. We calculate the total fluorescent intensity (I_0), the center of the mass vector ($\mathbf{r}_{cm}$) and the radius of gyration tensor ($\mathbf{G}$) of a DNA molecule in each frame:

$$I_0(t) = \sum_{m,n} I_{mn}(t) \tag{4.14}$$

$$r_{cm,i}(t) = \frac{1}{I_0(t)} \sum_{m,n} r_{mn,i}(t) I_{mn}(t) \tag{4.15}$$

$$G_{ij}(t) = \frac{1}{I_0(t)} \sum_{m,n} (r_{mn,i}(t) - r_{cm,i}(t))(r_{mn,j}(t) - r_{cm,j}(t)) I_{mn}(t) \tag{4.16}$$

where I_{mn} is the fluorescent intensity of the pixel [m,n], and i and j represent x or y directions that are perpendicular to the smallest dimension of the slit (z direction). The in-plane diffusivity (D) can be obtained from the mean-square-displacement (MSD)[119]:

$$MSD = \langle [r_{cm,x}(t) - r_{cm,x}(t - \delta t)]^2 + [r_{cm,y}(t) - r_{cm,y}(t - \delta t)]^2 \rangle = 4D\delta t \tag{4.17}$$

where δt is the lag time.

The radius of gyration tensor ($\mathbf{G}$) carries information about the instantaneous size, shape and orientation of the DNA. The radius of gyration (R_g) is the square root of the trace of $\mathbf{G}$. The eigenvectors of $\mathbf{G}$ represent the principle and minor axes that describe the temporal orientation of the DNA. More importantly, the longest relaxation time of the DNA can be extracted from the rate of the change of DNA orientation[106, 107]. We first calculate the angle between the principle eigenvector and the x-axis:

$$\theta(t) = \arctan \frac{\lambda(t) - G_{xx}(t)}{G_{xy}(t)}, \qquad \frac{\pi}{2} > \theta(t) > -\frac{\pi}{2} \tag{4.18}$$

where $\lambda(t)$ is the eigenvalue associated with the principle eigenvector. The time autocorrelation function of $\theta(t)$ is defined by[106]:

$$C_r(\delta t) = \frac{\langle (\theta(t) - \theta_0)(\theta(t - \delta t) - \theta_0) \rangle}{\langle (\theta(t) - \theta_0)^2 \rangle} \sim \exp(-\delta t / \tau_1) \qquad for \qquad \delta t \geq \tau_1 \tag{4.19}$$

where $\langle\rangle$ denotes the ensemble average. θ_0 is the equilibrium average of $\theta(t)$, and is taken to be zero in our calculation[127]. We will show that this assumption is valid in a later section.

The physical reason that one can obtain the longest relaxation time by tracking the rotation of the principle eigenvector ($\mathbf{P}$) of the radius of gyration tensor is because $\mathbf{P}$ is always parallel to the first normal coordinate of a chain[153] that represents the slowest mode of the chain's internal motion. We emphasize that the rotational relaxation time obtained by our method will be equal to $\tau_{1,s}$, or half of the true rotational relaxation time $\tau_{1,r}$ because the orientation of the principle axis is defined between $\pi/2$ and $-\pi/2$. Since the phase space is cut to half, the measured relaxation time becomes half of the true $\tau_{1,r}$. This fact has been verified using BD simulations.

A small amount of photobleaching will always occur in single molecule DNA studies. We must carefully examine our data to make sure the DNA physical properties are temporally invariant.

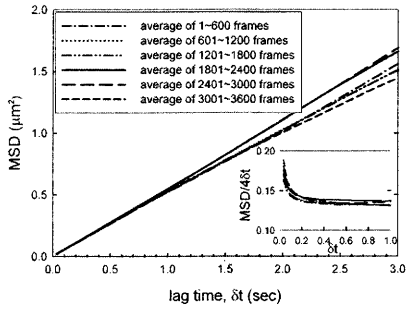

Fig. 4.1: *Analysis of λ-DNA diffusion in a 223nm high slit from different time segments of the experiment movies. The mean-square-displacement curves fluctuate at long lag times($\delta t > 1$ sec) due to limited statistics, but the deviation among the ensemble is not systemic. The inserted plot shows $MSD/4\delta t(\mu m^2/sec)$ versus δt. Despite the initial surge caused by the noise in the DNA images, the value of $MSD/4\delta t$ is fairly constant for $0.2 < \delta t < 1sec$. The frame rate for this data is 30 frames/sec.*

Two detrimental effects may associate with photobleaching on a stained DNA. Its contour length may shorten with time, and it may be nicked and eventually fragment[116]. We expect that DNA will diffuse and relax faster if it becomes shorter or more flexible. Therefore, by checking the time variation during the course of an experiment of either DNA diffusivity or relaxation time, we should be able to determine if DNA is intact through the experiments. Since we are not able to obtain accurate relaxation times using short movies, we choose to use diffusivity as the indicator. We cut each of our movies into six submovies and compare the MSD curves from the ensemble average of the submovies. Figure 4.1 shows the result of such an analysis for λ-DNA in a 223nm high slit. The MSD curves of the six different ensembles are very close to each other for $\delta t < 1$ sec. They fluctuate at long lag time space ($\delta t > 1$ sec) due to limited statistics while no sign of systemic change is observed. The inserted plot shows the value of $MSD/4\delta t$ for $\delta t < 1$. The curve starts high and decays to a constant after 0.2 secs. This initial surge is mainly caused by the noise in the DNA images. The same phenomenon occurs in colloid particle tracking experiments and has been investigated in detail by Savin and Doyle[119]. After the initial 0.2 secs, the value of $MSD/4\delta t$ is fairly constant and does not systematically vary over the six ensembles.

4.6 Results and Discussion

4.6.1 Measuring DNA relaxation time from rotational autocorrelation function

Given time-sequence images of DNA, one can extract the relaxation time not only from the rotational autocorrelation function, but also from the stretch autocorrelation function ($C_s(\delta t)$) that can be defined in a similar way as Eq 4.19 with θ replaced with DNA stretch. However, we choose to measure τ_1 from the rotational autocorrelation function for two main reasons. First, the relax-

ation time measured from the stretch autocorrelation function is greatly affected by the blooming effect that also decays with time due to the photobleaching of fluorescent dyes. Therefore, $C_s(\delta t)$ becomes a convolution of two decay modes. When this happens, $C_s(\delta t)$ does not become a single exponential decay even for $\delta t \geq \tau_1$. Although we have tried to remove this artifact by making a correction to the raw data, the resulting autocorrelation curves are not consistently as good as those from the rotational autocorrelation function. On the other hand, since the blooming effect is isotropic, it has minimum effect on the measured orientation of the DNA.

Second, it is difficult to estimate accurately the average stretch of DNA. Since the average value of the stretch must be subtracted from the temporal stretch in the calculation of $C_s(\delta t)$, its accuracy greatly affects the measured τ_1. We have characterized such effects using Brownian dynamics simulations and found that errors in the average stretch generally lead to a smaller relaxation time compared to the true relaxation time. The signature of this problem is that the autocorrelation function does not decay to zero in the long time limit. In contrast, θ_0 requires no estimation from the experiments and should be zero because the average orientation of a DNA is isotropic. We have checked this assumption in our experiments and found it to be valid.

Figure 4.2a shows a time sequence of a λ-DNA confined in a 223nm slit, and Figure 4.2b shows a typical time-evolution of the orientation angle $\theta(t)$ of a $\lambda-$DNA in this condition. Figure 4.2c shows the rotational autocorrelation function versus lag time in a linear scale. The dashed line is the single exponential fit to extract the longest relaxation time. This plot also demonstrates that $C_r(\delta t)$ decays to zero in the long lag time limit and confirms the validity of our assumption of $\theta_0 = 0$. Figure 4.2d is identical to Figure 4.2c, but in a semi-log scale. As can be seen, the autocorrelation function becomes a single exponential decay when the lag time δt approaches $\tau_1 \approx 0.67 sec$.

4.6.2 Relaxation time and diffusivity scalings versus channel height

We have measured the diffusivity and the longest relaxation time of λ-DNA in nanoslits with heights of 760nm, 475nm, 223nm and 92nm. The radius of gyration of λ-DNA is approximately 670nm using the relation $R_g = 0.203\frac{k_BT}{\sqrt{6}\eta_s D_{bulk}}$[58] and measured value D_{bulk}=0.47$\pm$0.03$\mu m^2/s$. The results of DNA diffusivity versus channel height are shown in figure 4.3a. We also plot the blob theory scalings with both Zimm-blob (Eq 4.9) and Rouse-blob (Eq 4.12) assumptions. As can be seen, the diffusivity of λ-DNA decreases with the decreasing channel height. The slope of the regression curve is 0.48$\pm$0.03. This scaling is between the Zimm-blob and Rouse-blob scalings, and may suggest the partial-draining nature of the blobs in our experiments.

We also compare the DNA diffusivity with those measured in our previous study[144]. Although the fitted slope of D versus h in the current study is slightly lower than that in the previous study[144] (0.55$\pm$0.05) over a similar range of channel heights, they are still within the error range. However, the absolute values of DNA diffusivity are constantly higher than those reported in our previous work by about 10%. The experimental setup of the current study is identical to that of our previous study except that an extra oxygen scavenger system consisting of β-D glucose, catalyse and glucose oxidase is introduced to the experimental buffer to further suppress photobleaching and to extend the lifetime of DNA in experiments. Similar buffers have been used by the Chu group [51, 57]. We call the buffers used in the previous and the current studies as BME and GLOX buffers, respectively. A λ-DNA molecule can only be continuously observed with our experimental setup for less than 30 sec without breaking in BME buffer, while it can stay intact for at least few minutes in GLOX buffer. This prolonged observation time allows us to measure the DNA relaxation

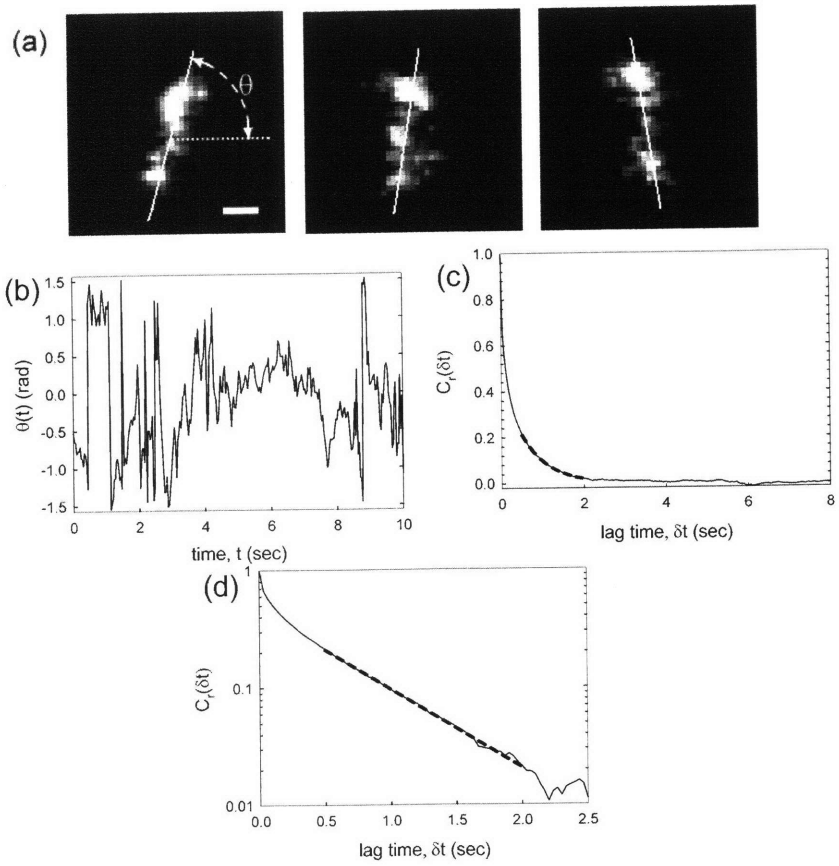

Fig. 4.2: *(a) A time sequence of a λ-DNA confined in a 223nm nanoslit. The time interval between each image is 0.1 sec. The solid line overlaying the DNA is the direction of the principle axis of the DNA calculated from the radius of gyration tensor. The orientation angle of the principle axis is designated as θ. The scale bar in the first image is 1μm. (b) A typical time-evolution of θ. (c) The ensemble average of the time autocorrelation functions of θ versus δt in a linear scale. The solid line is the experimental result, and the dashed line is a single exponential fit to extract the longest relaxation time from the data. This set of data is also measured from λ-DNA in a 223nm slit, and the longest relaxation time is found to be 0.67 sec. (d) The same plot as (c) but in a semi-log scale.*

Table 4.1: *Comparison of buffer viscosity and confined λ-DNA diffusivity measured in BME and GLOX buffers. The temperature was 22° C - 23° C.*

Buffer	BME buffer	GLOX buffer
Buffer viscosity (cp)	1.05	1.075
λ-DNA diffusivity in bulk solution($\mu m^2/s$)	0.456±0.041	0.474±0.032
λ-DNA diffusivity in 223 nm slit ($\mu m^2/s$)	0.118±0.004	0.130±0.002
λ-DNA diffusivity in 92 nm slit ($\mu m^2/s$)	0.071±0.003	0.081±0.001

time more accurately. Moreover, we cannot access the long relaxation time of BAC-DNA without the GLOX buffer.

To make sure the discrepancy in the measured DNA diffusivity is not caused by the channels or due to human error, we redo the experiments using λ-DNA with the BME and GLOX buffers in 92nm and 223nm slits, and confirm that the difference in λ-DNA diffusivity still exists. Table 4.1 summarizes the buffer viscosities and λ-DNA diffusivity in 92nm and 223nm slits. Since everything else is identical between the current and our previous studies, we suspect that the agents of the oxygen scavenger system may have slightly changed either the solvent quality or the persistence length of the DNA. We briefly check these two factors independently. If solvent quality becomes worse, a DNA coil shrinks and diffuses faster. However, blob theory predicts that if the solvent quality becomes worse and thus ν_{3d} becomes smaller, the diffusion coefficient should become more strongly dependent on the channel height. Such effect is not seen in our experiments because the diffusion coefficient becomes more weakly dependent on the channel height once GLOX buffer is used (see Fig 4.3a). On the other hand, we notice that the diffusivity of DNA is proportional to b^{-1} in bulk solutions[58], while blob theory predicts $D \sim b^{-5/3}$ in a slit. Thus, a 6% reduction in the persistence length will result in an increase of DNA diffusivity for 6% in bulk solutions and 10% in confinement. This picture is consistent with our results (see Table 4.1); however, we cannot fully confirm our explanation due to the magnitude of the error associated with the measured bulk diffusivity.

The relaxation time versus channel height is shown in figure 4.3b. We also plot blob theory scalings with both Zimm-blob (Eq 4.8) and Rouse-blob (Eq 4.11) assumptions. The experimental relaxation time follows the slope of -0.92±0.08 that again falls between the predicted scalings with Zimm-blob (-7/6) and Rouse-blob (-1/2), but is closer to Zimm scaling. With the above results, it is tempting to conclude that the blobs are partial-draining. However, we notice that the scalings of D and τ_1 versus h also depend on the values of ν_{2d} and ν_{3d} (see Eqs 4.8, 4.9, 4.11 and 4.12). Therefore, we cannot draw the conclusion before ν_{2d} and ν_{3d} are independently verified.

4.6.3 Relaxation time and diffusivity scalings versus DNA molecular weight

The relaxation time and the diffusivity of DNA with different molecular weights are measured in 475nm slits. The DNA diffusivity is found to be inversely proportional to its molecular weight (see figure 4.4a). This result agrees with our previous study and with the predictions given by both Eq 4.9 and Eq 4.12. It indicates that hydrodynamic interactions are totally screened between

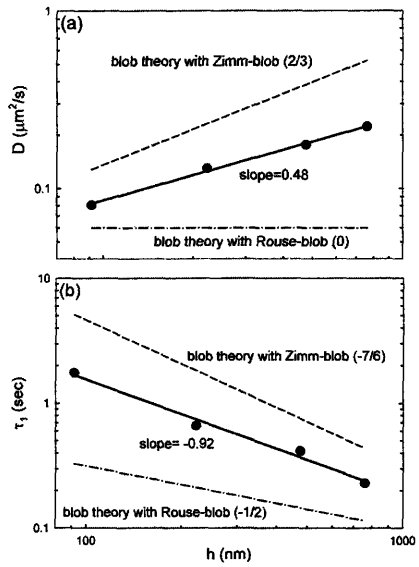

Fig. 4.3: *(a) Diffusivity versus channel height for λ-DNA. The slope of the best-fitting curve through the data is 0.48±0.03. The slope of the Zimm-blob scaling (dashed line) is 2/3, while the slope of the Rouse-blob scaling (dash-dot line) is 0. (b) The longest relaxation time versus the channel height for λ-DNA. The slope of the best-fitting curve through the experimental data is -0.92±0.08. The slope of the Zimm-blob scaling is -7/6, and slope of the Rouse-blob scaling is -0.5.*

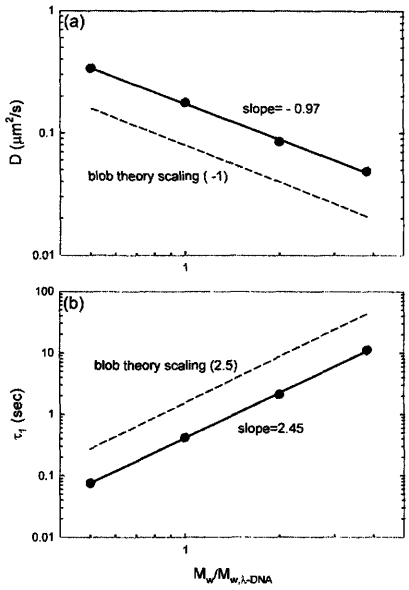

Fig. 4.4: *(a) Diffusivity versus molecular weight(M_w) relative to that of λ-DNA ($M_{w,\lambda-DNA}$) in 475nm slits. The slope of the best-fitting curve through the experimental data is -0.97±0.03. The slope of the dashed line is -1 that is predicted in both Eq 4.9 and Eq 4.12. (b) The longest relaxation time versus molecular weight(M_w) relative to that of λ-DNA in 475nm slits. The slope of the best-fitting curve through the experimental data is 2.45±0.04, in agreement with the blob theory scaling (2.5).*

blobs, but provides no information about hydrodynamic interactions within blobs. Figure 4.4b compares DNA relaxation times versus their molecular weights relative to the molecular weight of λ-DNA. The slope of the best fitted line over the experimental data is 2.45±0.04, very close to the theoretical value 2.5 predicted by Eqs 4.8 and 4.11. As discussed in an earlier section, this 2.5 power prediction arises from the assumptions of 2D SAW of blobs and absence of hydrodynamic interaction between blobs. Since the latter assumption has been confirmed, we can infer that DNA blobs in our system confined in a thin slit do follow a 2D SAW.

4.6.4 Verification of assumptions made in blob theory

As we have pointed out in earlier sections, it is important to verify the values of ν_{2d} and ν_{3d} in order to fully test de Gennes' assumptions, and this can be achieved by examining the scalings of $D\tau_1$ with N and h, respectively. As can be seen in Figure 4.5a and 4.5b, $D\tau_1 \sim N^{1.48\pm0.06}h^{-0.45\pm0.06}$. Comparing Eq 4.13 with the experimental scaling $D\tau_1 \sim N^{1.48}$, we can calculate $\nu_{2d,exp}$ to be 0.74(0.739). Then, substituting $\nu_{2d,exp}$ to Eq 4.13 and comparing it with $D\tau_1 \sim h^{-0.45}$, we obtain $\nu_{3d,exp}$ to be 0.60(0.603). The numbers in () are the values of $\nu_{2d,exp}$ and $\nu_{3d,exp}$ to three significant

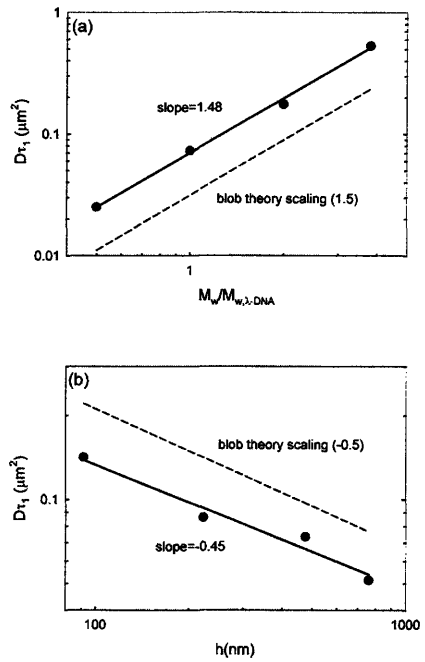

Fig. 4.5: *(a) Product of diffusivity and the longest relaxation time versus molecular weight relative to that of λ-DNA in 475nm slits. The slope of the best-fitting curve is 1.48±0.06. The slope of the dashed line is 1.5, predicted by Eq 4.13 using ν_{2d}=(3/4). (b) Product of diffusivity and the longest relaxation time versus channel height for λ-DNA. The slope of the best-fitting curve of experimental data is -0.45±0.06. The dashed line with the slope of -0.5 represents the scaling predicted by Eq 4.13 using ν_{2d}=3/4 and ν_{3d}=3/5.*

figures to highlight the small deviation in $\nu_{2d,exp}$ and $\nu_{3d,exp}$ from their ideal values. Since $D\tau_1$ is only a function of R, the estimated values of $\nu_{2d,exp}$ and $\nu_{3d,exp}$ are free from the influence of the drag coefficient that contains the information of hydrodynamic interactions within blobs. Giving the error associated with our experiments, $\nu_{2d,exp}$ and $\nu_{3d,exp}$ are indistinguishable from $\nu_{2d} = 3/4$ and $\nu_{3d} = 3/5$ used by de Gennes. Therefore, the assumptions of 2D SAW of blobs and 3D SAW of segments within blobs are valid.

Substituting $\nu_{2d,exp}$ and $\nu_{3d,exp}$ into Eqs 4.8, 4.11, 4.9 and 4.12, we obtain the expected scalings

that have accounted for the slight deviation in ν_{2d} and ν_{3d} observed experimentally:

$$\tau_{1,Zimm-blob} \sim N^{2.48} h^{-1.11} \tag{4.20}$$

$$\tau_{1,Rouse-blob} \sim N^{2.48} h^{-0.45} \tag{4.21}$$

$$D_{Zimm-blob} \sim N^{-1} h^{0.66} \tag{4.22}$$

$$D_{Rouse-blob} \sim N^{-1} \tag{4.23}$$

Comparing these scalings with experimental results in figure 4.3, we can readily confirm that blobs are partial-draining, not non-draining as de Gennes has assumed. It is also worthwhile to note that the experimental scaling of $D\tau_1$ with h seems to deviate considerably from de Gennes' prediction, which leads one to expect a sizable discrepancy between $\nu_{3d,exp}$ and ν_{3d}. However, $\nu_{3d,exp}$ is found almost identical to ν_{3d}. The discrepancy in the scaling of $D\tau_1$ with h is found to be caused by the combined effect of the slight deviations in $\nu_{2d,exp}$ and $\nu_{3d,exp}$ from their ideal values. It highlights the significance of our argument that one might be mislead to erroneous conclusions by comparing the experimental data with the blob theory scalings without noticing the convolution of several assumptions.

As we have mentioned in an earlier section, the more accurate value of ν_{3d} is 0.588. Therefore, we want to clear any concern that using $\nu_{3d} = 0.588$ may affect our conclusion. Substituting $\nu_{2d} = 3/4$ and $\nu_{3d} = 0.588$ into Eqs 4.8, 4.11, 4.9 and 4.12, we obtain $\tau_{1,Zimm-blob} \sim N^{2.5} h^{-1.25}$, $\tau_{1,Rouse-blob} \sim N^{2.5} h^{-0.55}$, $D_{Zimm-blob} \sim N^{-1} h^{0.7}$ and $D_{Rouse-blob} \sim N^{-1}$. We note that the scalings of τ_1 and D with N remains the same while those with h change. Using $\nu_{3d} = 0.588$ leads to an even larger discrepancy between the experimental results and the blob theory predictions with Zimm-blob assumption. This finding reinforces our conclusion that blobs are partial-draining.

4.6.5 Comparison to relaxation times in other studies

The goal of this section is two-fold. First, we want to compare the DNA relaxation times measured in the current study with those reported in other studies. Second, we want to construct a master plot of DNA relaxation time and thus provide an easy way for estimating τ_1 of DNA molecules in different degrees of confinement.

If de Gennes' prediction is perfectly held, one expects $(\tau_1/\tau_{1,bulk}) \sim (h/R_{g,bulk})^{-7/6}$, where $(\tau_1/\tau_{1,bulk})$ depends only on the degree of confinement, but is independent of the polymer molecular weight, M. Here M is equivalent to N defined in an earlier section. To reach the above formula, we have used $\tau_{1,bulk} \sim M^{1.8}$, and $R_{g,bulk} \sim M^{0.6}$[57, 58]. Since we observe deviation from de Gennes' prediction in our experiments, we use measured scalings and reach a similar formula: $(\tau_1/\tau_{1,bulk}) \sim M^{0.1}(h/R_{g,bulk})^{-0.92}$. Due to the very weak M dependence, we are able to construct a master plot for comparison and estimation of the relaxation time of a DNA under different degrees of confinement. We collect the data from this study, Randall and Doyle[15, 140], Randall[14] and Bakajin et al.[92], and plot $(\tau_1/\tau_{1,bulk})$ versus $(R_{g,bulk}/h)$ in Figure 4.6. The bulk values of the longest relaxation time $\tau_{1,bulk}$ and the radius of gyration $R_{g,bulk}$ are estimated using $\tau_{1,bulk} = 0.1\eta_s(M/M_{\lambda-DNA})^{1.8} sec$, and $R_{g,bulk} = 0.7(M/M_{\lambda-DNA})^{0.6}\mu m$ [51, 57, 150]. η_s is the solvent viscosity in the unit of centipoise (cp). We note that the DNA relaxation time collected from other studies were all measured from the relaxation of initially stretched DNA. To estimate the relaxation

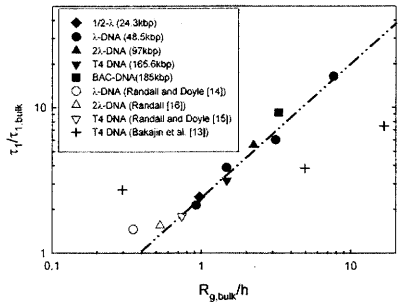

Fig. 4.6: *A master plot of the longest relaxation time of DNA versus the degree of confinement. The bulk values of the longest relaxation time* $\tau_{1,bulk}$ *and the radius of gyration* $R_{g,bulk}$ *are estimated using* $\tau_{1,bulk} = 0.1\eta_s(M/M_{\lambda-DNA})^{1.8}sec$, *and* $R_{g,bulk} = 0.7(M/M_{\lambda-DNA})^{0.6}\mu m$. *The dashed line is the regression over the results of λ-DNA in different channels from the current study. The black symbols indicate the data of this study. The hollow symbols indicate those from Randall and Doyle[14, 15, 140]. The cross symbols are estimated from Bakajin et al.[92]. The diamond, round, up-triangle, down-triangle and square symbols represent 1/2-λ DNA, λ-DNA, 2λ-DNA, T4-DNA and BAC-DNA, respectively. Except for the current study, the longest relaxation times of DNA were measured by observing the relaxation of an initially stretched DNA.*

times of T4-DNA in Bakajin et al.[92], we have used

$$(X^2 - X_0^2) = A\exp(-t/\tau_1) \tag{4.24}$$

where X^2 is the stretch square obtained from their figure 4, X_0^2 is the equilibrium value of X^2, and A is a free parameter. We find $\tau_1 \approx 2.5$, 3.6, and 6.8 sec in $5\mu m$, 300nm and 90nm slits, respectively. These values are in agreement with their qualitative description that the relaxation time of a T4-DNA was doubled when the slit height decreased from $5\mu m$ to 300nm, and was doubled again when h decreased from 300nm to 90nm.

As can be seen in Figure 4.6, all our data and those of Randall and Doyle fall along the dashed line within a narrow band for $R_{g,bulk}/h > 0.5$. The dashed line with the slope of 0.92 is the regression over measured τ_1 of λ-DNA in different channels from the current study. τ_1 of other sizes of DNA measured in 475nm high channels also agree well with the regression. In order to further verify the master plot, we also measure the rotational relaxation time of T4-DNA in a $1\mu m$ slit-like glass channel (donated by U.S. Genomics). The result is shown as the black down-triangle in figure 4.6, and it does follow the dashed line closely. The results of Randall and Doyle spread in the region where DNA is less confined. Their results start to deviate from the dashed line at $R_{g,bulk}/h \approx 0.5$, where the channel height is equal to the unconfined coil size of a DNA. Although the transition is very smooth, it indicates where blob theory starts to break down. On the other hand, the relaxation times estimated from Bakajin et al., although in qualitative agreement with

our results, deviate significantly from the master curve. The cause of this discrepancy is not yet clear, but we suspect that it is because the data of Bakajin et al. are single-chain results. Due to molecular individualism[53], even physically identical molecules can behave differently under identical conditions. Therefore, accurate results are only accessible through analysis of an average of many single-chain results. Another possible cause of this discrepancy is that Bakajin's data only covered the normalized chain extension $\overline{X}$ from 0.6 to 0.2 while the true relaxation time is only accessible near equilibrium. $\overline{X}$ is defined as the ratio of DNA stretch to its contour length. In single-molecule studies, the relaxation time is typically fitted where $\overline{X}$ is smaller than 0.3. We also note that one tends to obtain a relaxation time smaller than the true relaxation time when monitoring the relaxation of an initially highly stretched chain in good solvent. The reason is that although the excluded volume has strong effect on the relaxation time of a chain, it has little effect even when $\overline{X}$ is around 0.3.

4.6.6 Effective relaxation time for confined DNA

A polymer will be deformed from its equilibrium when Weissenberg number $Wi = \tau_{effective}\dot{\gamma}$ is larger than one. Although $\tau_{effective}$ is typically taken as the longest relaxation time τ_1 in bulk, this is not always true for a confined polymer. For a chain confined in a slit, if the flow gradient is imposed over xy plane (z direction is the smallest dimension), $\tau_{effective}$ is indeed equal to τ_1. As a result, long DNA will be stretched much easier than short DNA because τ_1 scales as $N^{2.5}$. Such a flow condition can be generated, for instance, in a slit with a contraction in either x or y direction[47]. On the other hand, if the flow gradient is applied along z direction such as in simple shear flow or in Poiseuille flow, all confined chains, regardless their size, will start to deform from equilibrium at the same critical strain rate. This is because the flow gradient is only applied over the size of a blob where τ_{blob} is the governing time constant at this length scale, and τ_{blob} depends only on the channel height but not on DNA molecular weight[136].

While we cannot measure τ_{blob} directly, we can estimate it given that τ_1 is known. For instance, Balducci et al.[144] have estimated the R_g of a M13mp18 DNA (7.2kbp) to be 240nm. Therefore, a blob in a 475nm ($\sim 2 \times 240nm$) slit will contain roughly 7.2kbp. Since we have shown blobs follow a 2D SAW, the relaxation time of a blob can be related to its longest relaxation time by $\tau_1 = N_{blob}^{2\nu_{2d}+1}\tau_{blob}$[55, 141]. Using $\tau_{1,BAC-DNA,475nm} = 11.1sec$ and the experimental scaling $2\nu_{2d} + 1 \approx 2.48$, we obtain $\tau_{blob,475nm} \approx 3.5 \times 10^{-3}sec$. Therefore, if one wants to deform a linear DNA confined in a 475nm slit with a shear flow, a shear rate of at least 300 sec^{-1} is required. We can roughly verify this value of τ_{blob} by comparing it with the relaxation time of a 7.2kbp DNA in bulk solutions. Using $\tau_{1,\lambda-DNA} = 0.1sec$ in water with Zimm scaling in good solvent, we obtain $\tau_{1,7.2kbpDNA} \approx 3.3 \times 10^{-3}sec$ that is a little lower than the estimated $\tau_{blob,475nm}$.

Having the above idea in mind, we are able to explain some unusual observations reported in recent literature[47, 135]. For instance, Larson et al.[47] characterized the average stretch of BAC-DNA ($R_{g,bulk} \approx 1.6\mu m$) confined in a $1\mu m$ glass slit in Poiseuille flow. A significant rise in BAC-DNA stretch was observed from a gap averaged shear rate $\dot{\gamma} \approx 250s^{-1}$, and the DNA stretch did not reach a plateau until $\dot{\gamma} \approx 6000s^{-1}$. We estimate $\tau_1 \approx 4sec$ and $\tau_{blob} \approx 0.04sec$. Therefore, if one naively uses τ_1 as $\tau_{effective}$, DNA seems to be undeformed until $Wi \approx 1000$, and its stretch does not saturate until $Wi \approx 24000$! However, using τ_{blob} as $\tau_{effective}$ we find that DNA starts to stretch at $Wi \approx 10$ and its stretch saturates at $Wi \approx 240$. It is not surprising that DNA did not start to deform at $Wi \approx 1$ since the velocity gradient is nonuniform in Poiseuille flow. Similarly, Stein et

al.[135] measured the mobility of λ-DNA in Poiseuille flow in a 250nm high slit (see their Fig. 1). The gap averaged shear rate was around $90sec^{-1}$ while no flow-induced deformation of DNA was observed. Again, if $\tau_1 \approx 0.7sec$ is used, $Wi \approx 60$. While we estimate the true $Wi = \tau_{blob}\dot{\gamma} \approx 0.06$. The same phenomenon has been predicted and discussed by Jendrejack et al.[136, 154] for DNA confined in square channels. Woo et al.[139] also demonstrated in simulations that the tumbling dynamics of DNA is hindered in confinement, and the dominating time constant of the tumbling dynamics is much smaller than the longest relaxation time measured in the xy plane.

4.7 Conclusions

In summary, we have measured the diffusivity and the longest relaxation time of DNA confined in silt-like nanochannels, and find $\tau_1 \sim M^{2.45}h^{-0.92}$. Comparing the experimental results with the predictions given by blob theory, we find that DNA blobs follow a 2D self-avoiding walk, and DNA segments within blobs follow a 3D self-avoiding walk. However, the assumption that hydrodynamic interactions dominate within blobs is found to be compromised. Our results indicate that blobs are partial-draining in the channels that we investigate. We expect that the assumption of non-draining blobs might become valid in the limit that a very long polymer confined in a large slit. In that case, there are enough polymer segments within a blob to induce very strong inter-segment hydrodynamic interactions. Using the experimental scalings, we find $(\tau_1/\tau_{1,bulk}) \sim M^{0.1}(R_{g,bulk}/h)^{0.92}$. The very weak M dependence allows us to provide a master plot of $(\tau_1/\tau_{1,bulk})$ versus $(R_{g,bulk}/h)$. Relaxation times of confined DNA reported in other studies are collected in the master plot for comparison. Our results are in good agreement with those of Randall and Doyle[14, 15, 140], but not with those of Bakajin et al.[92]. We also addressed how the longest relaxation time and the blob relaxation time of DNA are related and when they are the dominant time constant in different flow conditions. We explain the recent observations that extreme high shear rate is required to deform a confined DNA using the blob picture.

With dependencies of DNA dynamics at equilibrium well in hand, we turn in chapters 5 and 6 to observations of DNA in non-equilibrium conformations.

CHAPTER 5

Relaxation of Deformed Polymers in Confinement

The previous chapters characterized the behavior of DNA in confinement at equilibrium. However, for gene mapping and other applications of interest, the polymer conformation is significantly stretched and far from equilibrium. In this and the following chapter, we evaluate DNA dynamics in perturbed conformations. The purpose of this chapter is to investigate DNA properties during recoil of the molecule. In confinement, we find that the polymer conformation is especially important to the dynamical behavior of the polymer due to the fact that the conformation of the chain also determines whether or not the polymer "feels" the applied confinement. For instance, if a polymer is fully stretched, its lateral dimension (in the confined direction) is 2 nm, much smaller than any of the channels used here (or that can be made currently). For relaxation in confinement, the fact that the polymer "feels" the walls causes a new characteristic time scale to emerge. This chapter presents the discovery of this new relaxation time and a simple model from which studies aiming at a more detailed understanding can be built. It is important to realize that the existence of *two* slow modes of relaxation will have very interesting repercussions in terms of molecular manipulation, which we leave for discussion in chapter 6

5.1 Overview

We experimentally observe two separate timescales governing the entropic recoil in the linear force-extension regime of single ds-DNA in slit confinement. We demonstrate the existence of two distinct relaxation regimes at different extensions during relaxation. Contrary to bulk measurements, the true longest relaxation time may only be probed very close to equilibrium. A simple model of the relaxation mechanism leads to a scaling analysis that correctly predicts the extension at the crossover between the two regimes.

5.2 Introduction

Micro- and nano- fluidic systems show much promise in their ability to precisely control flows, reactions, and even biological separations [54]. Micro-devices have recently been used in DNA separations [98] and single-molecule mapping [50]. The performance of such devices is highly dependent on the conformation of the polymer in response to collisions [19] and field gradients [50]. The deformation of the polymer is the result of a competition between the imposed stretching rate and polymer relaxation. Therefore, to efficiently design new devices, it is important to understand the effects of confinement on the relaxation of a polymer.

Historically, blob theory has been used as a method to study slit-confinement effects on the longest relaxation time of a polymer [81]. Several studies have since characterized the relaxation time of DNA in slit confinement. An experimental study by Bakajin *et al.* [102] presented the relaxation of initially stretched DNA as a function of time. The authors reported that the longest relaxation time increased with decreasing channel height, as expected. A later study [155], in an effort to compare new longest relaxation time results obtained through conformational fluctuations at equilibrium, fit the data from Bakajin *et al.* to a single-exponential decay over available extensions ($\sim$ 50% to 10%). Results from the two studies give different apparent longest relaxation times [155]. Furthermore, each experimental study is supported by analogous computer simulations. Simulations of a relaxing chain with hydrodynamic interactions (HI) have been able to reproduce the extension data of Bakajin *et al.* [124, 138], but were not compared to blob theory. Monte Carlo simulations, which access the relaxation time through fluctuations at equilibrium but neglect HI, have found scalings in accord with a free-draining blob theory [141, 149]. These Monte Carlo results are in better agreement with the more recent experimental findings [155]. Taken together, these previous results suggest that different relaxation modes may be probed in the recoil and equilibrium studies.

In this Chapter, we argue that slit confinement induces a new relaxation regime. Experimental results of the extension evolution of a confined, relaxing chain are best described by *two* distinct time constants within the linear force-extension regime. In contrast, experiments on unconfined DNA show that a single time constant describes the dynamics of a relaxing chain from the onset of the linear force regime ($\sim$ 30% extension) to equilibrium [156, 157]. We show that a simple scaling analysis correctly predicts the crossover between the two regimes as well as relaxation time scalings near equilibrium. We also show that, in slit confinement, the true longest relaxation time governs the dynamics of the polymer only very close to equilibrium and thus can be easily overlooked without careful analysis.

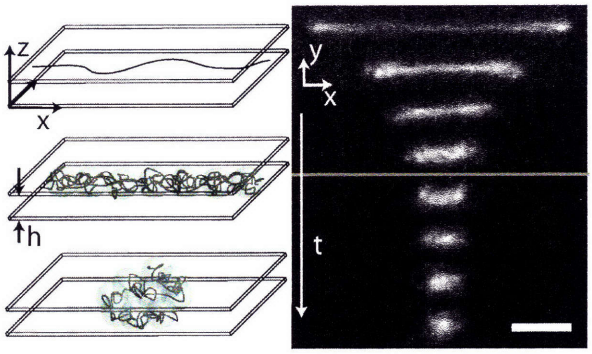

Fig. 5.1: *Schematic of confined polymer relaxation along with ensemble-averaged time-series images of 5λ-DNA. The time between the images is 5 s and the scale bar is 10 μm. The gray line represents the predicted crossover between the two relaxation regimes discussed in this chapter.*

5.3 Experimental Methods

The relaxation of T4 DNA (165.6 kbp, Nippon Gene) and λ-DNA concatamers (194, 242.5, and 291 kbp, referred to as 4λ-, 5λ-, and 6λ-DNA respectively) were observed in a 1 μm tall glass microchannel (unless otherwise noted). λ-DNA (New England Biolabs, NEB) was ligated with T4 ligase (NEB) for 25 minutes. All DNA samples were stained with YOYO-1 (Invitrogen) dye at 4 bp per dye molecule and diluted into 0.5x TBE (Omnipur) which contained 4% (vol.) beta-mercaptoethanol (Cabiochem), 12.5 mg/mL glucose (Mallinckrodt), 0.16 mg/mL glucose oxidase (Roche), 7.4 μg/mL catalase (Roche) and 0.1% (wt.) 10 kDa poly(vinylpyrrolidone) (Polysciences). The 200 μm wide microchannel contained three rows of 2 μm diameter cylindrical obstacles spaced at 4 μm. An electric field was used to stretch the DNA on the obstacles and was turned off after the stretched DNA exited the post array. The λ-DNA concatamers were identified during a symmetric collision by measuring the contour length (L_c) of the nearly fully extended molecule. Our imaging set-up and image analysis is described elsewhere [155]. The extension (X_{ex}) was determined by the projected distance along the initial stretch direction.

Images were collected on a Hamamatsu EB-CCD camera at 30 fps for T4 DNA and 15 fps for the λ-DNA concatamers. The reduced frame rate for the larger polymers allowed collection of adequate equilibrium statistics. Image pre-processing consisted of rotation and noise filtration. Image rotation aligned the DNA with the x-axis at the moment the electric field was turned off and all subsequent frames were rotated by the same amount. The rotation angle was calculated as in Ref. [155]. Noise filtration consisted of background subtraction and shot noise filtration. The first was achieved by using pixels on the border of the movie to sample the population of background pixels and estimate their average and standard deviation. Shot noise consisting of one or two bright pixels away from the DNA molecule was found to be detrimental to extension measurements. Therefore, we further processed each image pixel by pixel: if the average value of the pixels surrounding a given pixel did not exceed a given value (set to 4 times the standard

deviation measured above), that pixel was set to the background intensity, otherwise the pixel was unchanged. Unlike a true low-pass filter, we find that this process eliminated all bright pixels away from the DNA without smearing, blurring, or altering the image of the DNA itself.

Extension measurements were obtained as the maximum distance projected along the x-axis between two points on the DNA molecule. Computer analysis used a simple threshold to find these points; the value of the threshold was chosen to match a subset of data analyzed by hand. The extension was first divided by the applicable contour length (see Table 5.1), then the time was set to 0 at the frame where the relative extension was closest to 30%. Resulting single molecule data is presented in Fig. 5.2. The relative extension squared was then averaged at each point in time over all individual molecules. The equilibrium value of the relative extension squared was then subtracted from this ensemble average. Scaled in this manner, the curves were fit using

$$\frac{\langle X_{ex}^2 \rangle - \langle X_{ex,eq}^2 \rangle}{L_c^2} = A_n \exp\left(-t/\tau_n\right) \tag{5.1}$$

where A_n and τ_n are fitting parameters. Error in the fitted parameters was calculated using a least squares analysis on the fitted data.

5.4 Results and Discussion

Figure 5.3a displays the scaled squared extension of the DNA as a function of time for increasing molecular weight. Each curve represents the ensemble average of 20-45 molecules. Previous work has explained the need to fit the squared extension in single molecule relaxation experiments in order to extract a longest relaxation time that agrees with rheological measurements [156]. The curves in Fig. 5.3a display two distinct time constants; one near 30% extension and another near equilibrium. A different presentation of the data for 4λ-DNA is shown in the inset where the decay has been normalized such that the plot should be horizontal over the region in which the fitted time constant describes the decay. The inset figure shows two time-distinct plateaus, and each fitted region persists in time for more than twice the applicable time constant. The crossover (taken as the intersection of the extrapolated fits) occurs at a relatively constant scaled square extension of 0.002 to 0.005 or relative extensions (X_{ex}/L_c) of 7 to 9%. In this paper, the higher extension time constant will be referred to as τ_I and the low extension time constant as τ_{II}. Table 5.2 displays both relaxation times, and Fig. 5.3b shows the results of this study in comparison to previous results in slit confinement [102, 155]. We propose that the two different relaxation time constants found in this study are due to two different relaxation mechanisms present at different extensions and not due to the nonlinear elasticity of the DNA.

Although we study extensions in the linear force regime, there may be several reasons for the observed change in slope in Fig. 5.3a. For example, when the stretched DNA leaves the obstacle the tension distribution is initially asymmetric. To check this, we calculate the distance from the right and left endpoints of the chain to the center of mass as a function of time and fit our data only after the relaxation is symmetric around the center of mass 5.4. Symmetry is obtained very shortly after the DNA leaves the post (1-2 s), suggesting that the asymmetric tension distribution quickly re-equilibrates throughout the chain [158]. Further, an accurate measure of the mean equilibrium extension ($\langle X_{ex,eq} \rangle$) is needed in order for the data in Fig. 5.3a to properly decay to zero at long times. We investigated both the polymer size and diffusivity at equilibrium (Fig. 5.5a) and find these are in agreement with blob theory [80, 144], confirming that the polymers are confined at

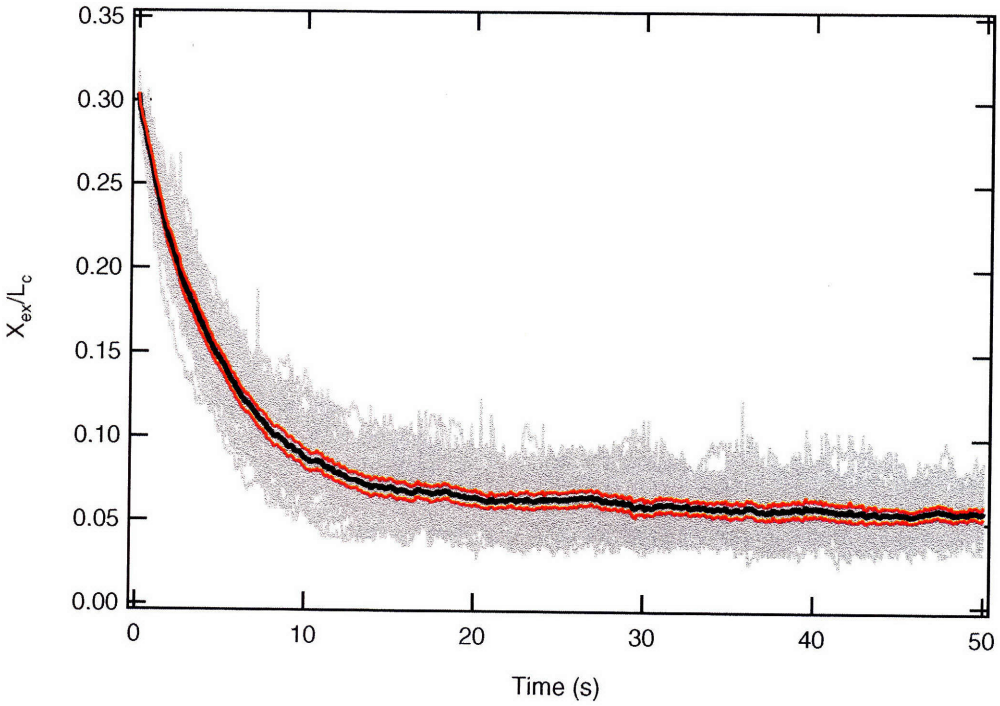

Fig. 5.2: *Extension, normalized by the contour length for 4λ-DNA as a function of time. The grey curves indicate values for individual molecules, the black line is the ensemble average, and the red lines are a 95% confidence band (± 2 standard errors).*

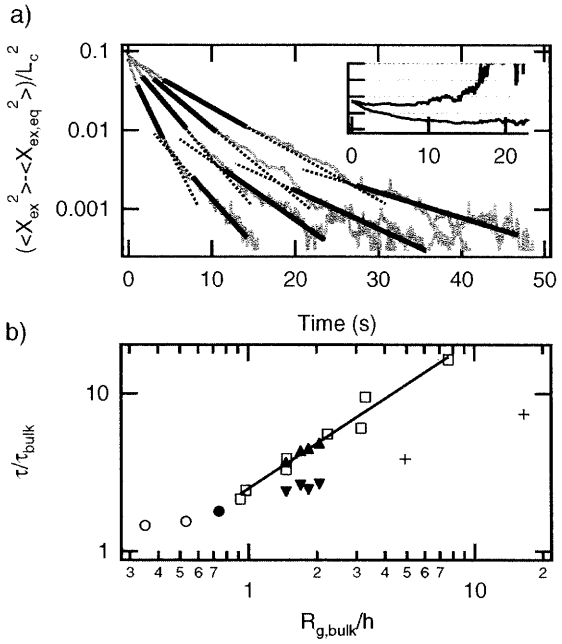

Fig. 5.3: *A.) Normalized extension versus time (t) for T4, 4λ-, 5λ-, and 6λ-DNA from left to right.* $X_{ex}/L_c = 0.3$ *at* $t = 0$. *Solid lines are fits to the data; dotted lines are extrapolations of the fits to guide the eye. Regime I is fit to a single exponential from the onset of symmetric relaxation (see text) until approximately twice the crossover extension predicted by Eq. 5.2. Regime II is fit from half the crossover extension to statistical noise taken as the equilibrium extension* ($X_{ex,eq}$, *a typical fluctuation distance) divided by the square-root of the number of DNA molecules observed. Inset:* $(\langle X_{ex}^2\rangle - \langle X_{ex,eq}^2\rangle)/(L_c^2 \exp(-t/\tau_n)), n = I, II$ *for 4λ-DNA versus time in seconds. B.) Measured relaxation time in confinement normalized by bulk relaxation time versus the inverse channel height normalized by the bulk radius of gyration. Open symbols are previous measurements by our group [155], + are single exponential fits [155] to data from Bakajin et. al. [102], and data from this study are represented by ▼* (τ_I), *▲* (τ_{II}), *and • (T4 DNA,* $h = 2\ \mu m$). *The solid line is an empirical fit from ref [155] with slope 0.92.*

equilibrium. To ensure this transition is truly caused by confinement effects, we qualitatively compare the relaxation of T4 DNA in a 1 and 2 μm tall channel (Fig. 5.5b). If the transition is caused by confinement, we expect to delay or completely eliminate the transition by increasing the channel height. The transition is absent in the 2 μm channel. We will return to this result. We conclude that the existence of two separate relaxation regimes is indeed a confinement effect.

To explain the scalings of these relaxation regimes as well as the crossover point between them, we utilize a simple scaling model of the recoil. We describe the polymer in a tension-blob framework until the dimension of the tension blob is equivalent to the height of the channel. At this point, the confining effects of the channel walls become important (see Fig. 5.1). Before this point, relaxation occurs by increasing the size of the tension blobs along the chain, as if it were in bulk but with a modified drag coefficient. After this point, the blobs can no longer grow and must re-arrange within the channel to further dissipate stress. The second regime is equivalent to the relaxation of a quasi-two dimensional self-avoiding chain.

If we take the relaxation to be quasi-steady, good solvent scalings within blobs, and minimal rotation of the molecule during the initial relaxation, the crossover between the two above mechanisms occurs when blobs that span the height of the channel are perfectly aligned in the direction of original stretch. Using this criterion, the relative extension at the crossover point is

$$\frac{X_{ex}}{L_c} = \frac{hN_{blobs}}{Nb} = 2^{5/3} a_{bulk}^{5/3} b^{1/3} h^{-2/3} \tag{5.2}$$

where h is the height of the channel, and a_{bulk} is the proportionality constant relating the bulk radius of gyration ($R_{g,bulk}$) to the number of Kuhn steps ($N = L_c/b$):

$$R_{g,bulk} = a_{bulk} b^{4/5} N^{3/5} \tag{5.3}$$

Note that a_{bulk} incorporates an effective excluded volume diameter. Using $R_{g,bulk} = 0.69$ μm [155], $L_c = 21.5$ μm and $b = 106$ nm for stained λ-DNA, we find $a_{bulk} = 0.17$ μm$^{1/5}$. Equation 5.2 predicts a crossover extension of 8.0% (0.003 to 0.004 on the ordinate of Fig. 5.3a), in very good agreement with the experimental results. The crossover extension is not dependent on molecular weight, but depends on channel height and solvent quality, ionic strength, and temperature through dependencies in b and a_{bulk}. We can confirm the assumption of negligible rotation by measuring the average angle between the principle axis of the DNA and the original stretch direction (Fig. 5.5c). The DNA tend to stay oriented in the direction of original stretch for extended periods of time ($> \tau_I$), as seen previously in bulk simulations [159, 160].

We test the prediction of Eq. 5.2 by re-examining the T4 relaxation in a 2 μm channel. For this case, Eq. 5.2 predicts a crossover extension of 5%. The equilibrium extension in a 2 μm channel was measured at 6%, greater than the crossover value. Hence, equilibrium was reached and the poylmer stopped relaxing before entering regime II. This result demonstrates the effective upper bound on channel heights for which two relaxation time constants will be observed. The lower bound on channel height is set by forcing the crossover extension to be significantly less than 30% so that regime I is observable within the linear force regime. Between these two limits, the parameter space for dual-regime relaxation is of practical importance because DNA with sizes of interest ($\sim$100 kbp) will exhibit two relaxation regimes in channel heights from $\sim$200 nm to order microns.

We now compare both sets of measured relaxation times with those from previous studies (Fig. 5.3b), in particular the assembly of data presented in Ref. [155]. The data represented by

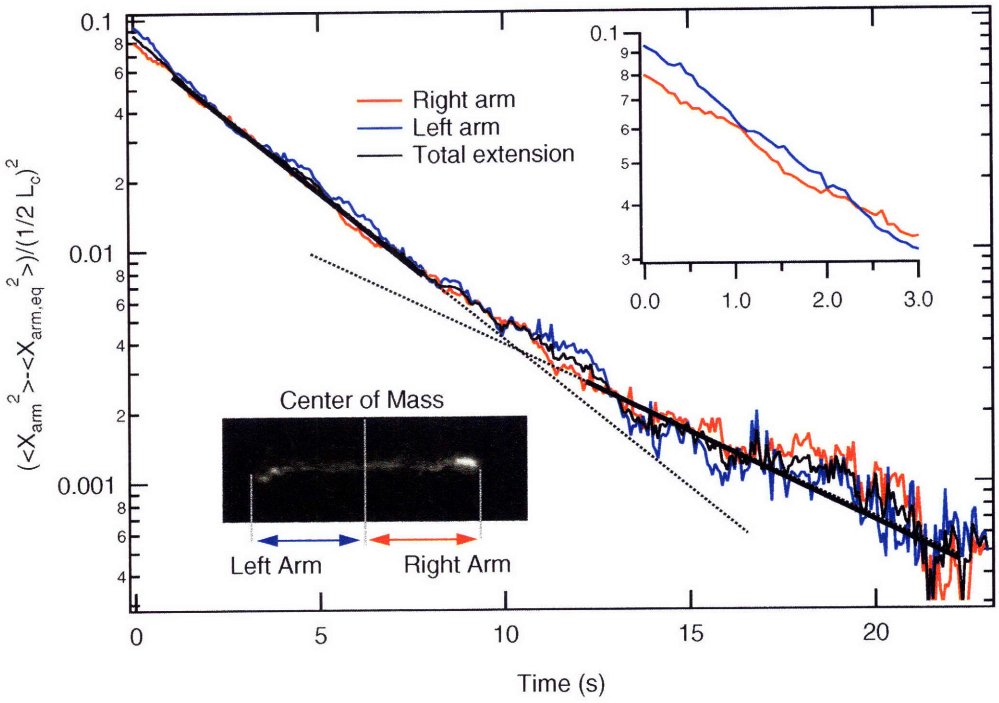

Fig. 5.4: *Scaled extension versus time in seconds for 4λ-DNA. The extension of the right (left) arm (X_{arm}) is defined by the distance between the right (left) endpoint of the chain and the center of mass (see inset diagram of an image of 4λ-DNA at t=0). The equilibrium value ($\langle X^2_{arm,eq}\rangle$) is subtracted from the ensemble-averaged squared extension ($\langle X^2_{arm}\rangle$) and the result is divided by $(\frac{1}{2}L_c)^2$, allowing direct comparison to the scaled decay of the scaled total extension of the molecule and fits from Fig. 2a of the main text (thin and thick black lines, respectively). Inset: Short time behavior of the full-frame plot.*

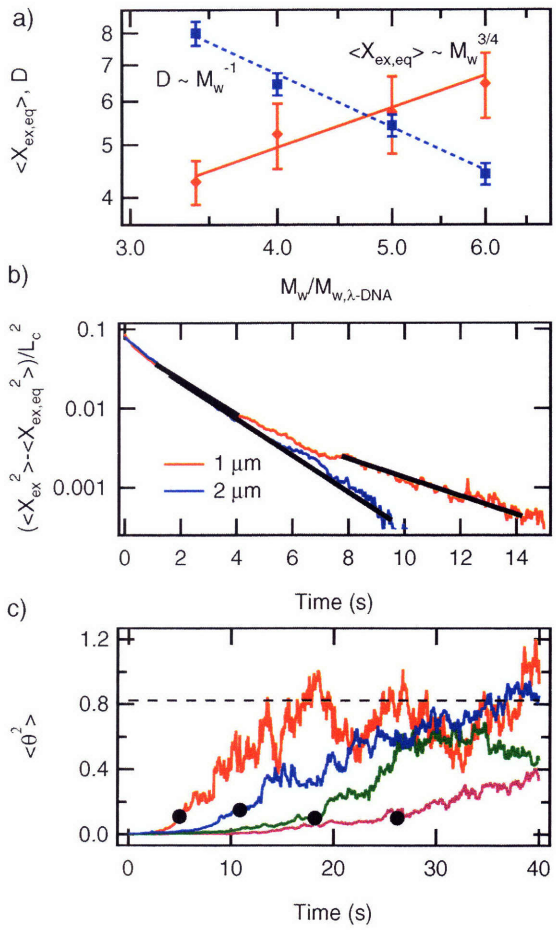

Fig. 5.5: *A.) Equilibrium extension (μm) and diffusion coefficient ($10^2 \mu m^2/s$) versus molecular weight normalized by that of λ-DNA. Lines are scaling predictions from blob theory. B.) Scaled squared extension of T4 DNA recoil in a 1 and 2 μm tall channel. Solid black lines are fits to the data. C.) Angle between the DNA principle axis and the original stretch direction for increasing molecular weight, left to right. The dotted line is the equilibrium value and the solid circles denote the crossover times from Fig. 5.3a.*

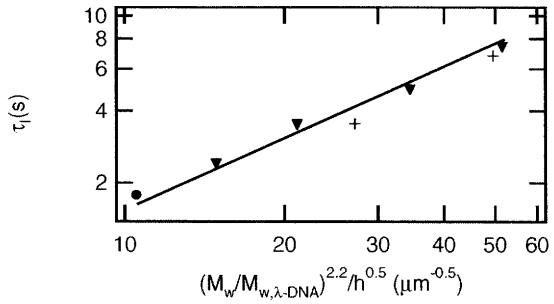

Fig. 5.6: *Scaling results for regime I. Solid line has slope = 1. Symbols are defined in Fig. 5.3b.*

the open squares is measured by the time-correlation of the orientation angle of DNA at equilibrium [155]. All other data are measured by following the relaxation of an initially stretched chain. It is clear that τ_{II} is in very good agreement with the rotation autocorrelation data taken over a range of molecular weights and channel heights. This data was previously compared to blob theory and is well-described within that framework [155]. We describe the low-extension relaxation (regime II) as arising from the steric confinement of the polymer and having the same scaling relation ($\tau_{II} \sim N^{2.45}h^{-0.92}$) as in Ref. [155].

We now turn to the regime I results presented in Fig. 5.3b. τ_I is significantly less than τ_{II}, signifying that confinement effects are not as strong in this regime. Data from Bakajin *et al.*, fit at comparable extensions to those of regime I, are included on the plot and appear to follow the general trend of the regime I data. The coincidence of these two data sets may explain previous discrepancies in the literature [155]. However, a different physical mechanism is needed to explain this regime.

Using again the scaling model description of relaxation described above, the relaxation in this regime is expected to be free of the steric effects of the confining walls. Woo *et al.* [124] found that the presence of the walls does not effect the spring force law for polymers at 30% extension until the channel height approaches the persistence length. Also, Stigter was able to reproduce the data from Bakajin *et al.* by taking into account the increased drag on the polymer due to the channel walls without confinement effects on the spring force law [138]. Assuming that the spring force constant scales as in bulk ($\kappa \sim R_{g,bulk}^{-2}$), we still need a scaling for the drag on an extended polymer in slit confinement. This scaling is not available at present; however, we expect that the drag will scale linearly with molecular weight due to hydrodynamic screening [144]. Empirically, we find that a scaling of

$$\tau_I \sim \frac{\zeta}{\kappa} \sim \frac{R_{g,bulk}^2 N}{h^{0.5}} \sim \frac{N^{2.2}}{h^{0.5}} \tag{5.4}$$

collapses the data from this study and that of Bakajin *et al.* (Fig. 5.6). The drag scaling used, $\zeta \sim Nh^{-0.5}$, is in agreement with previous experiments of diffusivity at equilibrium under similar confinement conditions [144]. This substitution assumes the drag on the polymer is constant throughout the relaxation process and the appearance of regime II is only due to a confinement-induced change in the spring force law.

5.5 Conclusions

We have demonstrated the existence of two separate, slow relaxation regimes present during polymer recoil in slit confinement. The existence of these two regimes has most probably been overlooked by researchers because for the same range of extensions an unconfined polymer relaxes with a single exponential decay. While the relaxation times for these two regimes follow similar scalings with N, the scaling with h is much stronger in regime II ($\sim h^{-0.92}$) than regime I ($\sim h^{-0.5}$). Further experiments and simulations should be performed to explore in more detail this scaling dependence on h. In addition to the fundamental importance of a new relaxation mode, the existence of these two regimes has important consequences in applications such as single molecule DNA mapping and electrophoretic separations that rely on controlling DNA conformations by the interplay of applied fields and molecular relaxation processes.

Table 5.1: *Contour length for DNA molecules. The contour length was calculated using* $L_c = 21.5 M_w / M_{w,\lambda-DNA}$ *(in microns), assuming a contour length of 21.5 μm for stained λ-DNA. Measured contour lengths, though always smaller due to incomplete stretching during collisions, are within 7% of these values.*

	T4 DNA	4λ-DNA	5λ-DNA	6λ-DNA
L_c (μm)	73.4	86	107.5	129

Table 5.2: *Relaxation times in a 1 μm tall channel.*

	T4 DNA	4λ-DNA	5λ-DNA	6λ-DNA
τ_I (s)	2.1 ± 0.1	3.5 ± 0.1	4.9 ± 0.2	7.4 ± 0.3
τ_{II} (s)	3.7 ± 0.7	5.8 ± 0.8	9.0 ± 2.6	13.5 ± 2.2

CHAPTER 6

Stretching DNA in Confinement

Since polymer relaxation is intimately tied to stretching, the fact that two relaxation times exist in confinement holds the possibility that stretching, too, is significantly modified in slit-like nanochannels. The purpose of this chapter is to investigate the effects of confinement on DNA stretching in an ideal, controlled, homogenously deforming electric field. A new nano-slit cross-slot channel device was designed to allow observation of DNA molecules in this precisely defined electric field, enabling direct comparison to theory and previous experiment. We find confinement serves to modify the nature of the coil-stretch transition, yield significantly more stretch at sub-critical Deborah numbers, and cause the second longest relaxation time to govern the location of the coil-stretch transition. The fact that the second longest relaxation time must be used to predict large deformations of the polymer is strikingly different from bulk dynamics and important since it is polymer behavior at those extensions that is pertinent to gene mapping experiments.

6.1 Overview

A nanofluidic cross-slot device is designed and fabricated to investigate the effects of slit-like confinement on the electrophoretic stretching of single DNA molecules. The device is capable of trapping and stretching single DNA molecules at the stagnation point of a homogeneous planar elongational electric field. Different from bulk studies, we find the *second-longest* relaxation time allows better prediction of the drastic increase of extension with applied strain rate in confinement. The longest relaxation time is important in polymer rotation and small deviations from equilibrium.

6.2 Introduction

The development of nanofabricated devices capable of confining single DNA molecules creates the potential to alter and control the DNA shape and dynamics [79, 80, 81, 84]. A series of recent single molecule studies has characterized DNA conformation and dynamics at equilibrium in different types of confinement (i.e. tube-like [44, 46, 85, 161, 162, 163], slit-like [144, 155, 164, 165], etc.), but significantly deformed molecules are important in a number of applications for DNA separation [18, 25] and mapping [30, 47]. Recently, nanoconfinement in one-dimensional (tube-like) channels has been used to create highly extended DNA of interest in particular to direct mapping methods [44, 46, 85, 161, 162]. Here, we report a facile method for dynamically trapping and stretching single molecules in *slit-like* nanoconfinement at a stagnation point. The molecular extensions attained here match those in the most extreme tube-like confinement, but in slit-like channels with photolithographically defined dimensions three orders of magnitude larger than the tube-like case. Also, since stretching the polymer can alter the interactions of the polymer with the confining walls [73, 166], the dynamics of the molecule can vary with extension, making this problem interesting from a fundamental polymer physics standpoint. Even with a recent surge in the research being done in this area (see [167] for a recent review), a complete understanding of polymer dynamics in confinement is lacking.

Recently, we found that the entropic relaxation of single DNA molecules from a stretched initial condition in slit-like confinement is governed by two separate time scales [166] (see Figure 6.1). The longest relaxation time (τ_{II}) governs behavior of the molecule only very near equilibrium and a "second-longest" relaxation time (τ_{I}) governs relaxation at higher extensions. In bulk experiments, a single time scale governs dynamics in the entire linear force regime (from equilibrium to approximately 30% fractional extension) [157]. We found that the emergence of the second slow mode was indeed due to the presence of the confining walls. A simple model based on the fact that, as a polymer relaxes, the lateral dimensions of the polymer grow and are eventually sterically confined by the channel walls correctly predicts the crossover extension where the relaxation time changes (X^*_{ex}, see Figure 6.1). It is important to note that both relaxation times in confinement are significantly greater than the bulk relaxation time, pointing to the fact that confinement may allow stretching of DNA molecules at smaller deformation rates, as described below. The purpose of this letter is to examine the effects of these newly observed relaxation physics on the electrophoretic stretching of single DNA molecules in slit-like confinement.

Polymer deformation in homogeneous extensional flows or fields is a balance of the stretching forces applied by the flow or field and the polymer's entropic elasticity tending to recoil the molecule [77]. In the unconfined case, a dimensionless group termed the Deborah number is typically used to characterize this balance. The Deborah number is defined as the product of the

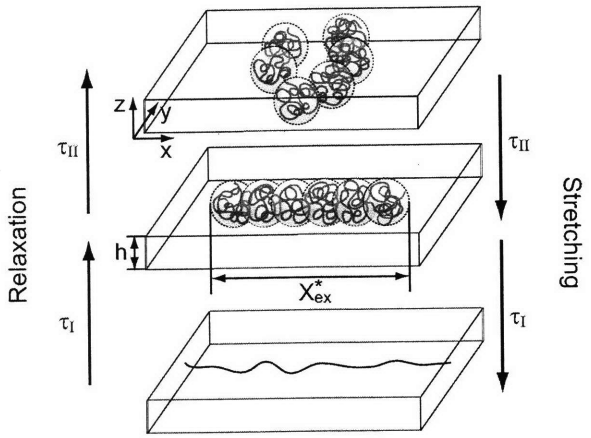

Fig. 6.1: *Schematic of the two longest relaxation times of DNA in slit-like nanochannels and the possibility of their importance in DNA stretching. Extended molecules are no longer sterically confined, and thus have different stretching and relaxation dynamics.*

deformation rate of the flow or field (the strain rate $\dot{\varepsilon}$) and the polymer's longest relaxation time (τ): $\mathrm{De} = \dot{\varepsilon}\tau$. A large change in extension with De is found [51, 52, 168] to occur near the theoretically predicted [71] critical value of $\mathrm{De}_{\mathrm{crit}} \approx 0.5$. The fact that two longest relaxation times exist in slit-like confinement brings some ambiguity as to the ability to predict where this drastic deformation occurs. This is especially important in the design of devices aiming to take advantage of the increase in relaxation times to stretch DNA [92, 155]. In slit-like confinement we expect the two different longest relaxation times to govern DNA behavior. The regions governed by each relaxation time are determined by the polymer's extension (unlike Rouse or Zimm modes). Hence we define two Deborah numbers for the current problem. The precise role of the two De's will be characterized below. $\mathrm{De}_{\mathrm{I}} = \dot{\varepsilon}\tau_{\mathrm{I}}$ is defined using the second-longest relaxation time, which governs relaxation above the crossover extension X^*_{ex} to approximately 30% fractional extension. $\mathrm{De}_{\mathrm{II}} = \dot{\varepsilon}\tau_{\mathrm{II}}$ is defined using the longest relaxation time, which governs dynamics near equilibrium.

6.3 Experimental Methods

6.3.1 Device design

To investigate confinement-induced changes on stretching DNA, we place single DNA molecules in homogeneous extensional electric fields under varying degrees of confinement. Electric fields are employed to move and stretch DNA because the kinematics are purely elongational at lengthscales larger than the Debye length (here $\sim 3\,\mathrm{nm}$) and deformation due to shear can be neglected [140]. In addition, electric fields are much easier to implement than pressure-driven flows for nano-scale devices. In planar elongational electrophoretic deformation, the electrophoretic velocity of a point

charge varies linearly with position:

$$v_x = \mu E_x = \dot{\varepsilon} x \tag{6.1}$$

$$v_y = \mu E_y = -\dot{\varepsilon} y \tag{6.2}$$

where v_x, v_y, are the velocities in the x and y directions, respectively, E_x and E_y are the electric fields in the x and y directions, respectively, μ is the electrophoretic mobility, and $\dot{\varepsilon}$ is the strain rate. Previous studies have used cross-slot [51, 52, 169] and T [168] channels to achieve these kinematic conditions. In tall channels the large spans used to create O(100 μm) regions of constant strain rate are not an issue. However, even slight sagging due to large spans in nanochannels affects the strength of the field and may cause pinch-off of the channel. Cross-slot nanoslit channels with the incorporation of hyperbolically curved sidewalls (see Figure 6.2) were implemented in this study. Since the shape of the sidewalls matches exactly the streamlines in homogeneous extensional fields, there are no inhomogeneities to disrupt the linear electric field profile over the entire intersection region [62]. This development minimizes the span needed to create O(100 μm) regions of homogeneous deformation. Independent control of the potential applied to the side reservoirs allows movement of the stagnation point via slight perturbations to the field [168]. These small adjustments allow the entrapment of DNA molecules at the stagnation point for very high accumulated strains (up to 50 Hencky strain units $= \dot{\varepsilon} t_{\text{res}}$, where t_{res} is the molecule's residence time in the field). Furthermore, due to confinement within the focal plane, every portion of the polymer is in focus for the entire observation time.

6.3.2 Channel fabrication and sample preparation

The channels are prepared using two methods. 2 μm tall channels are constructed in polydimethylsiloxane (PDMS, Sylgard 184, Dow Corning) using soft-lithography on a silicon master (SU8-2 photoresist). The channels are soaked in 0.5 × Tris-borate-EDTA (TBE, Omnipure) buffer at 40 °C overnight to eliminate permeation driven flow through the PDMS [170], rinsed and dried briefly, and sealed to a glass cover-slide. 300 nm and 150 nm tall glass nanochannels are created by a photo-resist protected etch in buffered oxide etchant and thermally bonded to a glass cover slide as described previously [94]. Nanochannels are filled with filtered RO-water and rinsed overnight via application of potentials at the fluid reservoirs. All channels are rinsed with the experimental buffer prior to exposure to DNA molecules. The buffer contains 4% betamercaptoethanol (BME, Cabiochem) and 0.1% 10 kDa polyvinylpyrrolidone (PVP, Polysciences) in 0.5 × TBE. The experimental buffer in the glass nanochannels also incorporates a glucose (Mallinckrodt)/glucose oxidase (Roche) /catalase (Roche) ($12.5, 0.16, 7.4 \times 10^{-3}$ mg/mL, respectively) oxygen scavenging system to allow prolonged exposures required in the small channels. The channel was flushed with new buffer every two hours during experiments to ensure a constant ionic strength environment [88]. DNA molecules (T4 DNA, 165.6 kbp, Nippon gene and λ-DNA, 48.502 kbp, New England Biolabs) are stained with YOYO-1 (Invitrogen) dye at a basepair to dye ratio of 4:1 and allowed to sit at least overnight. Our epifluorescence microscopy and detection setup as well as data analysis and extraction of the extension and principle axis of the radius of gyration tensor are described elsewhere [155, 166].

Table 6.1: *Channel dimensions and T4 DNA relaxation times.*

h	τ_{I} (s)	τ_{II} (s)	$\mathrm{De_{II}/De_{I}}$	l (μm)	w (μm)
2.0 μm	1.5	1.5	1	100	40
300 nm	2.7	5.4	2	50	40
150 nm	4.6	14.6	3.2	50	40

6.3.3 Electric field measurement

The electric field kinematics generated in the intersection region of all cross-slot devices were verified by tracking the center of mass of electrophoresing DNA under conditions in which they do not appreciably deform. λ-DNA was used as the tracer since both relaxation times (τ_{I} and τ_{II}) are not large enough to yield significant deformation at the electric fields employed. Figure 6.2C shows the center of mass position of 189 λ-DNA molecules as they electrophorese through the 2 μm tall channel. The role of the hyperbolically shaped sidewall is easily observed as no disruption to the streamlines occurs even very near the walls. Panels D and E show the experimental determination of the strain rate as the slope of the position versus time plots on semi-log scales. The strain rate is indeed uniform in the intersection region of the channel, and experiments at different applied voltages confirmed that the strain rate is linear with applied electric field for all channel heights used (data not shown). The strain rate is calibrated against applied voltage prior to each experiment.

6.3.4 Relaxation time measurement

Measurement of the relaxation time occurs in the same channel used for the stretching experiments. A T4 DNA molecule is stretched to nearly full extension in a high field gradient at the stagnation point, the field is switched off, and the relaxation of the molecule is observed. Two distinct time constants are obtained for the nanochannels, as expected [166]. The relaxation time is fit using the equation:

$$\frac{\langle X_{\mathrm{ex}}^2\rangle - \langle X_{\mathrm{ex,eq}}^2\rangle}{L_c} = A\exp\left(\frac{-t}{\tau}\right) \tag{6.3}$$

where X_{ex} is the extension of the molecule in the stretched (x) direction, $X_{\mathrm{ex,eq}}$ is the equilibrium extension in the stretched direction (measured after more than 10 relaxation times after turning off the field), L_c is the contour length of the T4 DNA molecule (70 μm) and t is time. A and τ are fitted parameters. Fitting regions for the two time constants are the same as those described previously [166]. Relaxation times for T4 DNA measured here are summarized in Table 6.1.

6.3.5 Experimental protocol

T4 DNA is used for the stretching experiments. A typical molecule is moved into the channel intersection and allowed to rest for typically 10 longest relaxation times. The field was then switched on and the molecule observed for 6 minutes or at least 20 units of strain. The time constraint is to limit photo-bleaching of and photo-induced damage to the stained DNA molecules. The extension of the molecule in the x-direction (X_{ex}) is measured via a simple threshold. Steady-state averages are obtained by sampling individual traces at time intervals equal to the second-longest relaxation time after the molecule has experienced a strain of 10 (except where not possible, then a strain of

5 is used). Ensemble averages are taken over at least 10 molecules (at the lowest strain rates) to more than 50 (at the highest strain rates).

6.4 Results and Discussion

Figure 6.3A shows the fractional extension (normalized by the contour length) with strain for individual molecules (gray lines) as well as their ensemble-average (bold line) for the 300 nm tall channel at $De_I = 1$. Figure 6.3B shows the ensemble-average extension for four De_I in the 300 nm tall channel. It is clearly observed, even for low De_I, that the molecules reach steady state after an applied strain on order 10. Thus, the trapping ability and residence times afforded by our device is sufficient for experimental observation of the steady state stretch at these deformation rates. The fact that steady state is reached after approximately 10 units of strain is interesting in its own right. This is the same order of magnitude as observed in bulk studies [78], implying that while confinement may alter the level of stretch that can be attained at a given strain rate, it does not necessarily significantly increase the rate of stretching. More careful studies focusing on the stretching transients are needed to fully characterize these effects.

Figure 6.4 shows the steady state extension versus dimensional and non-dimensional measures of the strength of the deformation applied. Figure 6.4A shows very clearly that confinement does indeed aid DNA stretching. The stretch increases at a given strain rate with decreasing channel height, more than 7-fold between the 2 μm and 150 nm tall devices at a strain rate of $0.2\,s^{-1}$. Importantly, at high extensions, the strain rate required to achieve a given extension can be decreased by more than 70% by exploiting confinement at these scales.

Figure 6.4B displays the same steady-state average extension versus De_{II}, the Deborah number using the longest relaxation time (τ_{II}) to normalize the strain rate. The data does not collapse over the entire range of De_{II}, and the location where the large increase in extension occurs does not agree with the predicted value of $De_{crit} = 0.5$. We conclude that the longest relaxation time does not govern the coil-stretch transition in slit-like confinement, in contrast to bulk results [51, 52, 67, 76]. These results are in accord with our previous data [166] where the dynamics of relaxation are governed by the longest relaxation time only very near equilibrium. We will return to this point below.

Figure 6.4C displays the steady-state average extension versus De_I, the Deborah number using the second longest relaxation time to normalize the strain rate. It is clearly seen that this second slow timescale collapses the data quite well, and the drastic increase in extension occurs at approximately $De_I = 0.5$. The coil-stretch transition and stretch at higher extensions are better described by the second-longest relaxation time, a phenomenon unique to confinement in polymer physics. This data collapse is also seen in the inset of Figure 6.4 where the standard deviation of the average extension (σ/L_c) is plotted against De_I. Recent studies [171] have shown that the peak in this plot is a very good indicator of the location of the coil-stretch transition, and here we note that the peak is well-aligned on the abscissa. This alignment confirms that the second-longest relaxation time governs the large increase in the stretch of the molecule with applied strain rate.

However, at low De_I, Figure 6.4C does show some differences in steady state extension between the three channel heights. Specifically, the coil-stretch transition becomes more gradual in the more confined channels. We observed significant stretching at sub-critical $De_I < 0.5$, but where $De_{II} > 0.5$ (see Figure 6.3C). The more gradual transition may also account for the decreasing amplitude of the peak in the standard deviation with De_I (inset of Figure 6.4C) [171]. As expected,

τ_{II} appears to affect stretching at low extensions, below the predicted crossover extensions [166] of $X^*_{ex}/L_c = 0.17$ and 0.27 for the 300 and 150 nm tall channels respectively. Note that these predicted crossover extensions over-estimate the region governed by τ_{II} because they predict the center of a gradual transition [166]. Since the changes of steady state extensions involved here are small, it is helpful to examine other indicators of behavior departing from equilibrium dynamics.

Figure 6.5 shows the root-mean-square angle (θ_{RMS}) of the principle axis of the in-plane DNA radius of gyration (see Figure 6.2) as a function of strain. θ_{RMS} indicates the degree of orientation towards the axis of elongation (x-axis, $\theta_{RMS} = 0°$) from the equilibrium average of $\theta_{RMS,eq} = 52°$ (the horizontal solid line in Figure 6.5). The angle reaches steady state at relatively low strain and fluctuates about the average. Figure 6.5A shows ensemble average θ_{RMS} traces and the steady state averages for the three channel heights at similar sub-critical De_{II} (≈ 0.25). The data collapses well and DNA molecules in three channel heights all show similar degree of orientation. Figure 6.5B shows the same quantities for the three channel heights at the same De_I ($= 0.3$). Data collapse is not as good and DNA molecules in the two nanochannels display significantly more orientation than those in the 2 μm tall channel. This observation is consistent with the fact that although De_I is sub-critical for all channel heights in Figure 6.5B, De_{II} are above 0.5 for the two nanochannels (0.6 and 0.96 for the 300 and 150 nm tall channels, respectively). Thus, the true longest relaxation time more adequately describes behavior close to equilibrium and should be used to predict the first deviations from equilibrium.

6.5 Conclusions

To conclude, we have designed a cross-slot device which yields large regions of homogeneous extensional deformation with limited spans amenable to the nanofluidic environment. Thus, we are able to exploit changes to the polymer dynamics induced by nanoslit confinement in order to facilitate dynamic manipulation of single molecules. We are able to easily select, trap, and stretch individual DNA molecules to steady state in this device with the molecule completely in focus for the entire observation. From the stretching results presented here, we conclude that confinement does aid the stretching of single DNA molecules by allowing the use of much smaller strain rates to achieve the same amount of extension. However, the time scale governing the large change in extension with applied strain rate is not the longest relaxation time (τ_{II}) but the second-longest relaxation time (τ_I), in contrast to bulk results. This finding is important since the prediction of this transition often forms the crux of design specifications for processes involving stretching or deforming DNA molecules, and naive application of bulk theory to confined systems would significantly under-predict the strain rates required to deform DNA molecules. The longest relaxation time (τ_{II}) governs the orientation and small deviations from equilibrium of the molecule. Our results are important for future studies of DNA dynamics in confinement, especially those concerned with the measurement of relaxation times or dynamic manipulation of extended DNA.

Funding for this work was provided by NSF Career Grant No. CTS-0239012.

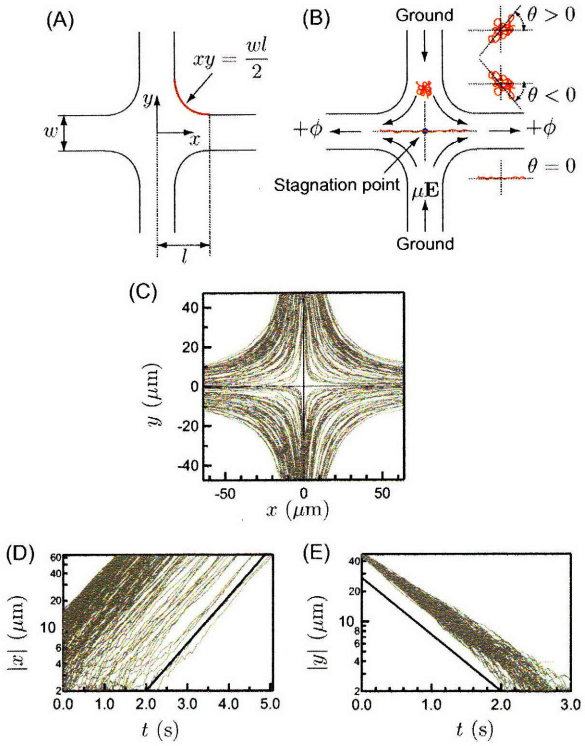

Fig. 6.2: *A. Diagram of the cross-slot stretching device geometry. B. Schematic of the motion and stretching of DNA molecules in the device. Independent applied voltages to the left and right arms of the channel allow adjustment of the location of the stagnation point and trapping of the DNA molecules. Also shown is the geometrical setup for the measurement of the angle of the principle axis of the radius of gyration. C-E. Confirmation of planar elongational deformation in the center region of the 2 μm device by tracking of λ-DNA molecules C. Trajectories of the center of mass of each λ-DNA molecule illuminate the electric field streamlines in the device. D and E display the x and y locations (respectively) of each molecule with time. The solid lines are the average of the fitted slopes of the individual traces, yielding a strainrate of* $\dot{\varepsilon} = 1.2 \pm 0.1\,\mathrm{s}^{-1}$. *The relaxation time of λ-DNA in a 2 μm tall channel is* $\tau_{\mathrm{I}} = \tau_{\mathrm{II}} = 0.2\,\mathrm{s}$ *[140], yielding* $\mathrm{De}_{\mathrm{I}} = \mathrm{De}_{\mathrm{II}} = 0.24 < \mathrm{De}_{\mathrm{crit}}$.

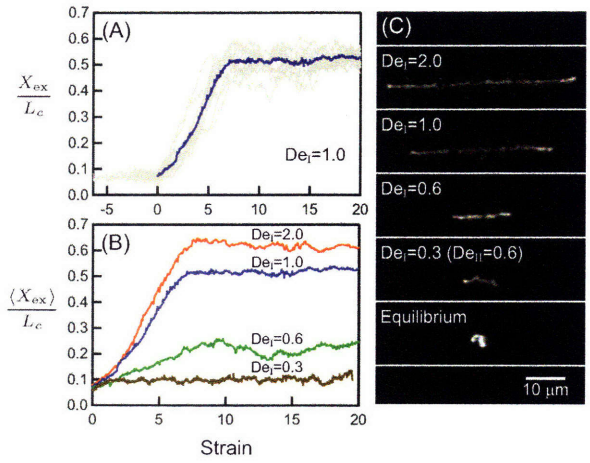

Fig. 6.3: *A. Gray lines indicate individual traces of the fractional extension of each molecule versus strain applied (residence time in the field times the strain rate) for* $\mathrm{De_I} = 1$ *in a 300 nm tall channel. The bold line is the ensemble average extension with strain. B. Ensemble average extension as a function of strain for selected* $\mathrm{De_I}$ *in the 300 nm tall device. C. Snapshots of individual DNA images at steady state at the given* $\mathrm{De_I}$ *in the 300 nm tall device.*

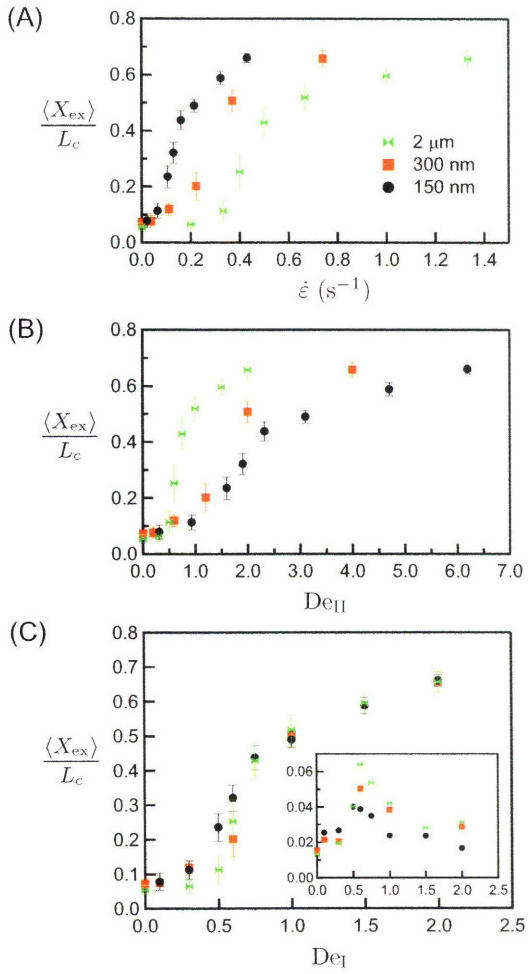

Fig. 6.4: *A. Ensemble average steady state extension versus the dimensional strain rate for three channel heights. B. Ensemble average steady-state extension versus* $\mathrm{De_{II}}$*, the strain rate normalized by the longest relaxation time. C. Ensemble average steady-state extension versus* $\mathrm{De_I}$*, the strain rate normalized by the second-longest relaxation time. Inset: Standard deviation* (σ/L_c) *of the steady-state stretch versus* $\mathrm{De_I}$*.*

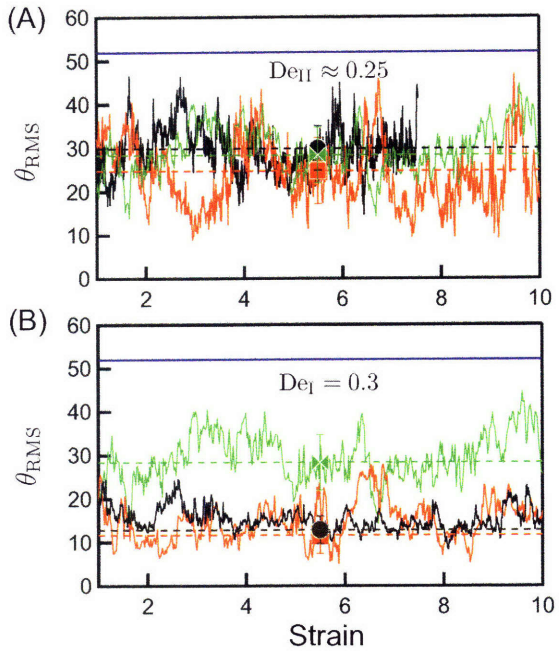

Fig. 6.5: *A. Root-mean-square angle of the principle axis of the radius of gyration relative to the x-axis (θ_{RMS}, in degrees) versus strain for* $De_{II} \approx 0.25$ *for the three channel heights. Green, red, and black solid lines denote the 2 μm, 300 nm, and 150 nm tall channels, respectively; colored dashed lines and markers denote the steady state ensemble average RMS angle.* $De_{II} = 0.3$, *0.2, and 0.32 for the 2 μm, 300 nm, and 150 nm channels respectively. The horizontal solid line denotes the equilibrium average ($\theta_{RMS,eq} = 52°$). B. θ_{RMS} for the three channel heights for* $De_{I} = 0.3$, *corresponding* De_{II} *is 0.3, 0.6, and 0.96 for the 2 μm, 300 nm, and 150 nm channels respectively.*

CHAPTER 7

Stretching DNA: Practical Concerns and Preconditioning

This chapter considers more applied aspects of DNA stretching. While we can learn a lot from the behavior of the steady-state stretch, if the transient behavior is too slow, the steady-state stretch will never be observed in reasonable processing timescales. Here, then, we investigate the possibility of using microfabrication to "preconfigure" DNA molecules (make the DNA conformation more amenable for later stretching). We find here that (1) collisions with posts prior to exposure to an extensional field do, in fact, increase the stretching observed after a finite strain and (2) the increase is largely due to the absence of slowly-stretching conformations.

7.1 Overview

We investigate the effectiveness of DNA conformational preconditioning by electrophoresis through an obstacle array on the later stretching of molecules in a microchannel contraction. The control, reproducibility, and ability to compare with the well-studied single post collision problem make this a model system for conformational preconditioning studies. We find that the obstacle array increases the average deformation applied to the DNA in the contraction through elimination of slower-stretching DNA conformations. In the current device, a dramatic change in the resulting polymer behavior occurs at a pre-deformation in the obstacle array of about 20% relative extension. We show that the hooking probability in the array is geometrically limited at large electric fields and that modification of the geometrical parameters shows promise for optimization of a second-generation device.

7.2 Introduction

Early visualization studies of DNA stretching directly observed that the rate of stretching of an individual polymer was greatly influenced by the polymer's initial conformation [51, 52]. Termed "molecular individualism," [53] this phenomenon, along with Brownian motion, provides the basis for much of the molecule-to-molecule variation between polymers subject to the same processing history [48]. Since the discovery and realization of significant advances in DNA mapping technologies that accompany precise control of molecular conformation [30, 47, 172], new interest has grown in a methodology to eliminate this molecular dispersion.

Very recent studies have used advances in nano-fabrication to modify the equilibrium conformation and attain this precise control, avoiding the molecular individualism effect [45, 46]. While significant progress has been made in this area, the practical alternative of dynamically altering the conformation with flow and flow gradients remains useful not only in larger, cheaper, and more robust devices, but also in the insight attained into flow properties of dilute polymer solutions [78, 145].

Significant efforts have been made to understand and mediate molecular individualism for finite-strain processes. In such devices, polymers which tend to stretch slower may not attain sufficient strain to stretch completely and therefore retain folds or kinks, for instance, at the exit and/or detection region of the device [47, 48, 49, 173]. As such, the focus was to reliably control the initial conformation of the polymer, i.e. precondition, the polymer for further processing [78]. Visualization [51, 52] and simulation [67] studies easily identified certain equilibrium or slightly-deformed conformations as likely to stretch quickly, while others are likely to fold and stretch slower. It was soon observed that molecules that had been stretched previously were less likely to form folds (i.e. stretch easier on subsequent attempts) [78]. Simulations have also shown that the extension attained in a shear-flow is sufficient to significantly increase the rate of stretching in a subsequent extensional flow [78].

Collision processes also change the conformation of DNA molecules [10, 13, 15, 19, 20, 174, 175], pointing to possible use in preconditioning studies. A recent study used a polymerized hydrogel as the collision matrix and tested its effectiveness to pre-configure DNA just prior to a microchannel contraction [48]. The gel caused the DNA to elongate by two mechanisms: by creating a mobility difference between the head and tail of the molecule as it exits the gel [176] and through collision processes between the gel and the DNA. That study found that the gel placed just prior to the

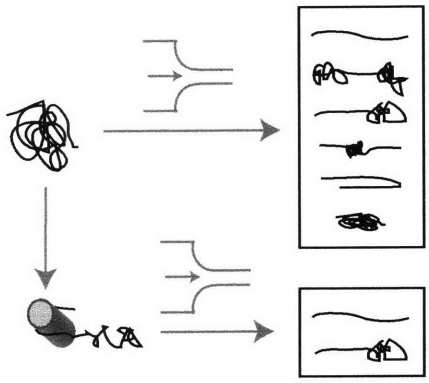

Fig. 7.1: *Schematic of molecular individualism (top) and molecular preconditioning (bottom) of a DNA molecule undergoing extensional deformation with finite strain. The final stretch and conformation of the polymer is largely dependent on the initial configuration of the polymer. Collisions with posts precondition the molecule and change the likelihood of the intermediate states in favor of faster-stretching configurations.*

contraction increased the average stretch and decreased the standard deviation of the stretching distribution of the polymers through the contraction. However, the inhomogeneity of the DNA behavior through the gel limited the results to being qualitative. Also, experimental difficulties in the fabrication of the gel, rinsing of the channel, and in the sticking of the DNA to the gel prohibit re-use of the channel and limit the scalability of the technique.

The purpose of this study is to investigate the possibility and quantitative effectiveness of using a microfabricated obstacle array placed immediately before a contraction to pre-configure DNA molecules for stretching. Figure 7.1 shows a schematic representation of the hypothesis of this work: an obstacle array can alter the final stretch of a molecule exiting a contraction through mediation of molecular individualism effects by controlling the initial conformation of the polymer. The use of collisions with cylindrical obstacles, a well-studied problem [10, 11, 12, 13, 15, 20, 174, 177, 178], offers insight into the polymer configurations during and after the collision event. Thus, it is possible to study the effects of a known processing history on downstream stretching of the polymer, a model preconditioning system.

7.3 Background

Deformation of a polymer from its equilibrium conformation in a purely extensional field is expected when the rate of deformation applied exceeds that of entropic relaxation [77]. The dimensionless parameter comparing these two rates is the Deborah number, $De = \dot{\varepsilon}\tau$, where $\dot{\epsilon}$ is the characteristic strain rate and τ the longest relaxation time of the polymer. Previous studies [51, 52] have observed that the coil to stretch transition occurs at nearly the theoretical prediction $De \approx 0.5$ [70, 71]. Above this critical De, the steady-state stretch (i.e. stretch after infinite strain) has been reasonably

described by a simple dumbbell model. In this model, the drag force acting to extend the dumbbell is balanced by the worm-like chain spring force [59]. Neglecting Brownian fluctuations, this force balance can be written as:

$$3De\frac{X_{ex}}{L_c} = \left[\frac{1}{4}\left(1-\frac{X_{ex}}{L_c}\right)^{-2} - \frac{1}{4} + \frac{X_{ex}}{L_c}\right] \tag{7.1}$$

where X_{ex} is the extension of the polymer in the flow direction, and L_c is the polymer contour length. This model has no adjustable parameters and can be used to estimate the amount of stretch attained after infinite strain (i.e. at steady state).

Previous studies have used flow gradients created either by contractions [47, 172, 179, 180] or cross-slot channels [51, 52]. Electric field gradients in similar devices have been used to stretch DNA [48, 140, 168, 169] with similar results, including the onset of stretching at $De = \dot{\varepsilon}\tau = \mu\nabla E\tau \approx 0.5$ (where μ is the electrophoretic mobility and ∇E is the electric field gradient). Electric fields are unusual in terms of kinematics in that local deformation is purely elongational (no vorticity) [140, 177]. Furthermore, upstream from the contraction, the electric field is constant and does not perturb the DNA from its equilibrium conformation [181].

The collision process between a DNA molecule and a single small obstacle has been previously studied by our group [15, 174, 177]. These studies classified collisions into four types, U, J, X, and W, depending on the conformation during the collision. In U and J collisions, the polymer stretch saturates while the polymer is still in contact with the obstacle and the polymer leaves the post with a rope on a pulley mechanism. The difference between U and J collisions relies on an arbitrary tolerance for the equality of the length of the arms on either side of the post. For this reason, and since the conformation leaving the post is expected to be very similar between the two types, we group U/J collisions together for the remainder of this work. X collisions are ones in which the polymer has not yet completely unraveled before disengaging from the obstacle. W collisions are ones in which both ends of the polymer are on one side of the obstacle (or folded multiple times on an obstacle) at the collision outset. The conformation imparted to the DNA varies drastically between U/J and X/W collision types.

Obstacle arrays in a variety of shapes and forms have been studied as models and possible substitutes for gel-based DNA separations [8, 17, 19, 182, 183]. These studies focused on the steady state migration through the arrays rather than the transient behavior at the start of the array. The DNA conformation in obstacle arrays is cyclic, going from a coiled to an extended state during a collision, after which the polymer migrates and relaxes before encountering another collision. A recent study [184] investigated the start-up behavior of single DNA molecules entering an obstacle array under pressure driven flow both with experiments and simulations. One major finding germane to our study is that the average hooking probability and configuration of the DNA do not change considerably past the third row of posts in the array, suggesting a length scale for startup effects in the array.

7.4 Experimental Methods

Microchannels used in this study are of the same form as those used previously [48] and are $w_1 = 200$ μm wide, $h = 2$ μm tall and of variable length (O(cm)). Each channel contains one hyperbolic contraction, with a contraction length L_c= 80 μm and a final width of $w_2 = 3.8$ μm.

The hyperbolical shape results in an electrophoretic strain rate which is nearly constant in the contraction. The nominal strain on polymers passing along the centerline as they move through the contraction is $\ln(w_1/w_2) = 4$. Obstacle-free microchannels are constructed with soft lithography. Poly(dimethylsiloxane) (PDMS, Sylgard 184, Dow Corning) channels are soaked overnight in 2.0 $\times$ Tris-Borate-EDTA (TBE, Omnipur) buffer to eliminate permeation-driven flow [170], briefly rinsed and surface-dried, and then sealed to a glass cover slide. Channels with obstacle arrays are microfabricated in glass using a deep reactive ion etch and were anodically bonded to a glass cover slip. The posts themselves are 1 μm in radius (R_{obst}), are spaced center to center by 4 μm (X_{sep}), in three rows with each row offset by 4 μm center to center, and the last row of posts is located 10 μm before the contraction. Due to the high ionic strength of the buffer used, and quenching of electroosmotic flow with a dynamically coated polymer layer, the small difference between the surface properties of PDMS and glass is not expected to be important.

The experimental buffer was 2.0 $\times$ TBE with 4% (v/v) beta-mercapto ethanol (Cabiochem) and 0.1% (wt) 10 kDa poly(vinyl pyrolidone) (Polysciences). Experiments in glass channels also incorporated a glucose (Mallinckrodt)/glucose oxidase (Roche) /catalase (Roche) ($12.5, 0.16, 7.4 * 10^{-3}$ mg/mL, respectively) oxygen scavenging system. T4gt7 DNA (Nippon Gene, 165.6 kbp, 70 μm stained contour length), stained overnight with YOYO-1 at a 4:1 bp to dye ratio, was observed through a 63X, 1.4 NA oil-immersion lens. The fluorescence signal was detected with a Hamamatsu EBCCD camera and recorded to digital videotape. Data analysis proceeded off-line using ImageJ software.

The extension of the polymer leaving the obstacle array and leaving the contraction is measured, as well as the type of collision (U/J, X/W, and non-hooking) and the conformation of the polymer at the end of the contraction. The categorization scheme used here is as follows: "stretched" polymers attain a linear conformation with a uniform intensity profile, "folded" polymers attain a linear conformation with at least one step change in intensity, and "coiled" polymers do not elongate to a linear conformation. As any categorization of the polymer conformation using fluorescence microscopy, this scheme is qualitative, but gives a general idea of the shape of the DNA moving through the contraction. More than 70 polymers are observed for each De (excluding $De = 1$).

A slight refinement of the collision-type categorization scheme is needed to allow use in an obstacle array and under non-uniform fields. We start with the definitions described above to determine the collision type. If there are multiple collisions or multiple collision types while traversing the array, the type of the last collision is used. Secondly, a hooking polymer is defined as a molecule which, during any imaged frame, has mass in all four quadrants around a single post with the direction of the abscissa defined along the direction of travel of the DNA as it impinges on the obstacle. This new definition is due to the fact that the electric field streamlines do not lie along a simple coordinate system in all areas of the device.

The longest relaxation time (τ) of the T4 DNA was measured in glass and PDMS channels of the same height as described previously [48, 51, 140]. Molecules are stretched on a post and then allowed to relax. A single-exponential was fit to the mean squared extension in time from 30% relative extension to equilibrium. The relaxation time measured in both the PDMS/glass and glass channels is 1.7 ± 0.2 seconds, in good agreement with previous measurements in similar conditions [48, 168].

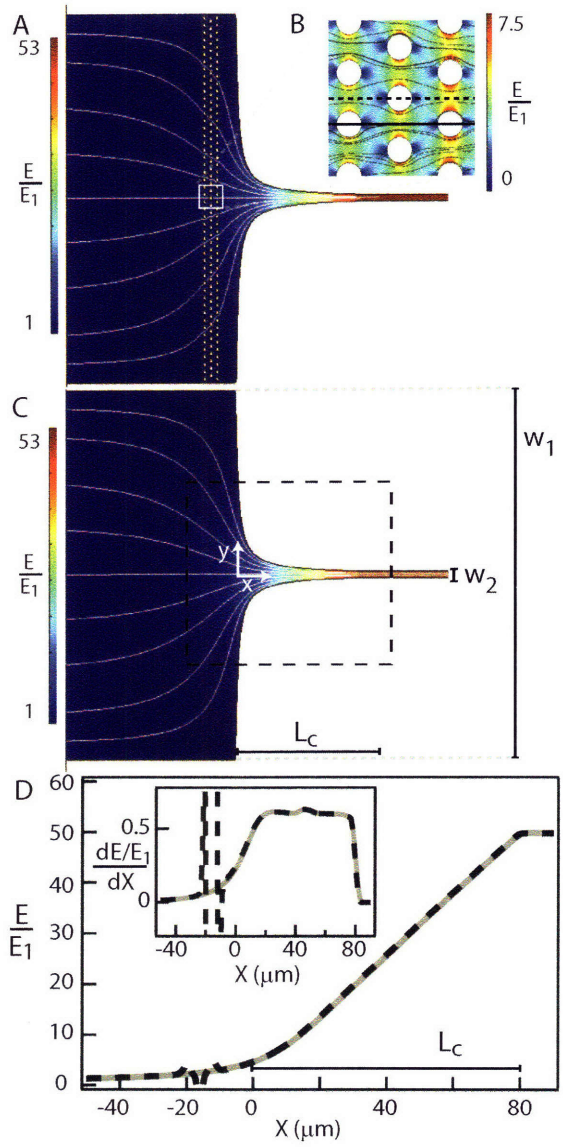

Fig. 7.2: *(a) Results of a FemLab simulation of the obstacle-array channel for the electric field magnitude normalized by the electric field in the wide part of the channel (E_1). (b) Close up of the electric field in the obstacle array at the channel centerline (dashed line). (c) Results of a FemLab simulation of the obstacle-free channel. Also denoted is the notation for the geometric characterization of the channel. (d) Electric field along the centerline of the channel for the obstacle-array (dashed line) and obstacle-free (solid gray line) channels versus X, the distance to the contraction entrance. Inset: Electric field gradient (units of μm^{-1}) along the centerline for obstacle-array (dashed line) and obstacle-free (solid gray line) channels.*

7.5 Results and Discussion

We first investigate the kinematics of the electric field in our device with finite element analysis as well as a more general scaling analysis. Since there are different sections of our device which yield different kinematics (strain rates), we cannot expect one dimensionless parameter to characterize the polymer behavior across the whole device. We therefore introduce several Deborah numbers based on characteristic strain rates which arise in different portions of the device. These scaling analyses as a whole will yield insight into the locations of possible polymer deformation as well as provide a basis for comparison to previous studies of polymer deformation and hooking on cylindrical obstacles.

Finite element simulations carried out in FemLAB software were used to calculate the electric field in both types of channels and are presented in Figure 7.2. As seen by comparison of panels a and c, and in the more quantitative comparison along the centerline (d), the electric field away from the obstacle array is nearly identical in the two channels. As previously observed [48, 180], there does exist a large entrance region prior to the contraction where the strain-rate ramps to its final value. The length scale for the entrance region is w_1. The obstacle array is placed in the entrance region. This placement ensures that deformation applied by hooking on a post does not relax away before the molecule enters the contraction. Due to the hyperbolic shape of the contraction, the strain rate reaches a constant value over much of the contraction, and rapidly decays to zero at the end of the contraction. As expected, the electric field increases by a factor of $w_1/w_2 = 52.6$ through the contraction. A simple scaling argument, taking the change in electric field magnitude (ΔE) and dividing by the distance over which the change occurs (ΔR) can be used to approximate the field gradients in the contraction: $\nabla E \approx \Delta E/\Delta R = \frac{E_1(w_1/w_2-1)}{L_c}$ where E_1 is the electric field in the wide part of the channel. This analysis yields a result within 3% of the simulated field gradients. Conversion to the electrophoretic strain rate requires multiplication by the electrophoretic mobility, μ, measured to be 1.4 ± 0.1 $(\mu m\ cm)/(s\ V)$ in both types of channels. This analysis leads to the definition of the Deborah number in the contraction:

$$De = \frac{\mu E_1(w_1/w_2 - 1)}{L_c}\tau. \tag{7.2}$$

The posts themselves also alter the field, creating field gradients over small length scales ($O(R_{obst})$) which can potentially alter the conformation of the DNA. The electric fields and the electric field gradients are shown in Figure 7.3 for two horizontal slices near the centerline (solid and dashed lines in Figure 7.2b). The gradients in this section of the channel are superimposed on the deformation due to the entrance region of the contraction, but there is significant length scale separation ($w_1 \gg R_{obst}$) which allows a scaling analysis of the gradients in the obstacle array treating the entrance region as a simple modification to the background electric field. This obstacle-induced field deformation gives rise to separate strain rates and therefore different applicable Deborah numbers. At the stagnation point at the front of a single isolated obstacle, the electric field varies from its far-field value (E^∞, the value of the electric field a few post radii from the obstacle, $E^\infty \sim O(E_1)$) to 0 ($\Delta E = E^\infty$) over the characteristic length scale R_{obst}. The characteristic De_{obst} has been previously defined using the maximum electric field gradient at the surface of the post [177]:

$$De_{obst} = \frac{2\mu E^\infty}{R_{obst}}\tau \tag{7.3}$$

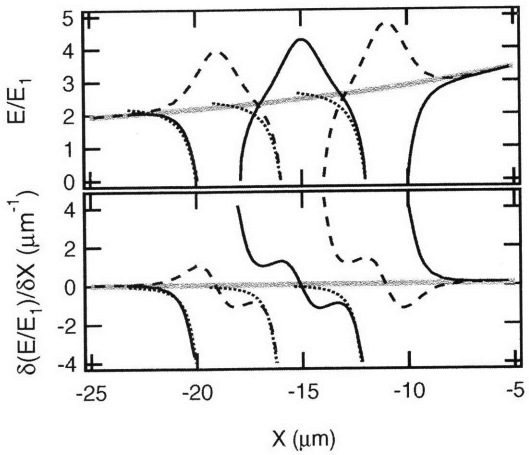

Fig. 7.3: *(a) Normalized electric field magnitude in the obstacle array versus X, the distance to the contraction entrance. The dark dashed and solid lines correspond to the like lines in Figure7.2(b). The solid gray line is for the obstacle-free channel and is calculated along the channel centerline. The dotted lines are evaluations of the analytical solution for the electric field around a cylindrical obstacle (eq 7.4 with $\theta = 0$), E^{∞} is approximated by the electric field in the obstacle-free channel at the location of the center of the post. (b) Electric field gradients for the data in (a).*

where the factor of 2 is a result of the analytical solution around a single, insulating post [140, 177]:

$$\boldsymbol{E} = E^{\infty}\cos\theta\left(\frac{R_{obst}^2}{r^2}-1\right)\boldsymbol{e_r} + E^{\infty}\sin\theta\left(\frac{R_{obst}^2}{r^2}-1\right)\boldsymbol{e_\theta}. \tag{7.4}$$

Here r is the distance to the center of the post and θ is the angle to the direction of the far-field electric field. De_{obst} governs the deformation of a DNA molecule in the field gradients prior to a single post. These gradients decay rapidly away from the post (as $(R_{obst}/r)^3$), and as our posts are spaced $4R_{obst}$ center to center, the field-deformation effects from one post are expected to be minimal at adjacent posts. We expect, then, this De_{obst} to affect the field-assisted hooking probability according to the mechanism discussed previously [177]. This effect is especially valid at the first row of posts, where the field experienced by the polymer is nearly uniform prior to the post. As seen in Figure 7.3, the electric field prior to and around the second- and third- row posts is affected by the previous posts in the array as discussed below. Very near the posts ($\sim R_{obst}$), however, the electric field and gradients are well approximated by the single-post solution (Eq 7.4 displayed as a dotted line in Figure 7.3).

Polymers which traverse freely to the second row of posts may be deformed by the field gradients between two first-row posts (see Figure 7.2b). Due to the finite size of the posts, they act in aggregate to reduce the cross-sectional area of the device by a factor of $c = X_{sep}/(X_{sep} - 2R_{obst})$ where X_{sep} is the center-to-center post spacing. Due to the constant current constraint, the electric field must increase by the same factor ($\Delta E \sim (c-1)E^{\infty}$) over a distance comparable to the post radius ($\Delta R \sim R_{obst}$). In our device, $c = 2$, yielding $\dot{\epsilon} \sim \frac{\mu E^{\infty}}{R_{obst}}$ and:

$$De_{array} \approx \frac{\mu E^{\infty}}{R_{obst}}\tau \tag{7.5}$$

where E^{∞} is again the far-field electric field. De_{array} is applicable to the deformation of polymers that pass between two posts. For scaling purposes, we notice that E at the start of the obstacle array along the centerline is $\approx 2E_1$, and we use this value to approximate E^{∞}. Using this value, $2De_{array} = De_{obst} = 6.2De$ and the predicted field gradients normalized by E_1 are $2\mu m^{-1}$ and $4\mu m^{-1}$ for between posts and at the stagnation point, respectively. As can be seen in Figure 7.3, these scaling values agree quite well with the simulated electric field gradients in the device. Since the two Deborah numbers in the post array are greater than that in the contraction, we cannot *a priori* neglect possible deformation and preconditioning in the obstacle array at field strengths sufficient to deform polymers in the contraction, even for non-hooking polymers. Also, since we study conditions for which De_{obst} is on order 1 to greater than 10, we expect to at least be partly in the regime where the obstacle collision probability varies with the applied field.

It is also worthwhile to note that the stretch evolution has been found to depend on the initial y-position of the molecule in this contraction geometry [49]. To mitigate these effects, only polymers within the experimental field of view (black dashed square in Figure 7.2c) approximately $\pm$ 45 μm from the channel centerline are considered for analysis. Also, since the streamlines are observed to bend prior to the obstacle array, the local relative orientation of the obstacle array and the field streamlines also change with y-position, possibly altering the hooking probability. However, in the region of observation, these are secondary effects to those just discussed.

Figure 7.4a demonstrates the effectiveness of the obstacle-filled channel in comparison to an obstacle-free channel and the simple dumbbell model described in Eq 7.1. The ensemble average

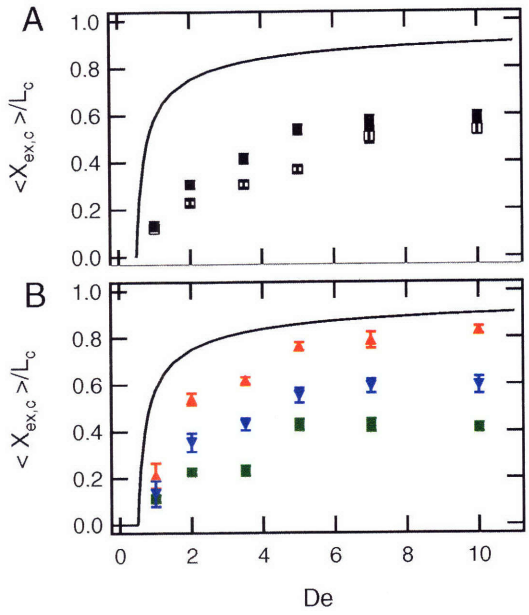

Fig. 7.4: *(a) Ensemble-average relative stretch at the end of the contraction versus De for T4 DNA in obstacle-filled channels (■) and obstacle-free channels (□). Also shown is the infinite-strain stretch calculated from the simple dumbbell model (Eq 7.1). (b) Average relative stretch at the end of the contraction versus De sorted by collision type, ▲, ▼, ■ represent U/J, X/W, and non-hooking collisions respectively. The same dumbbell model shown in (a) is displayed for reference. Error bars in both plots are the standard error.*

stretch at the end of the contraction ($\langle X_{ex,c} \rangle$) is significantly less than the model due to the finite strain applied. The extension measured in the obstacle-filled channel is systematically greater than the stretch for the obstacle-free channel at all *De* investigated implying that the posts alter the initial configurations and the conformational paths taken to the stretched state. The effect is greatest in the middle of the range of *De*, where the final stretch in the obstacle array is 150% of that in the obstacle-free channel. At low field strengths, the deformation imparted to the DNA on the obstacle is small and the low velocities for these polymers means there is the most time for relaxation between the collision and the contraction. The diminishing effect at high *De* is probably due to the fact that the the U/J collisions approach the infinite-strain model prediction (Figure 7.4b), providing an effective extension ceiling for the most effective collisions.

Figure 7.4b displays the average stretch at the end of the contraction by the type of collision experienced by the polymer during the obstacle array. As expected, the U/J collisions outperform the X/W collisions, which in turn outperform the polymers which do not hook. The X and W collisions are grouped together, but it should be noted that the number of X collisions overwhelms that of the W collisions (in all cases $>$ 95% of X/W collisions are classified as X collisions). Surprisingly, the non-hooking collisions do not differ significantly from the obstacle-free channel sample, implying that the steep electric field gradients experienced between the posts do not alter the conformation of the polymer in such a way as to aid stretching.

Figure 7.5 displays histograms of polymer stretch at the end of the contraction for *De*=2 (a) and *De* = 7 (b). As expected and observed previously, the U/J collisions are the optimal pre-conditioners, with a peaked distribution at high extension which is clearly distinct from the non-hooking collisions. The X/W collisions result in polymers with a broad stretch distribution at the end of the contraction. We note here that the data for the obstacle channel is normalized by the total number of polymers observed in the channel (the accumulated area under the solid symbols is unity). The data in the open channels is rescaled such that the integrated probability is set equal to that of the non-hooking molecules in the obstacle array channel. The purpose of this rescaling is to highlight the similarity between these two curves. The stretching distribution of non-hooking polymers and polymers in the obstacle-free channel nearly quantitatively agree. We conclude that the pre-conditioning experienced by the polymers in the obstacle-filled channels is nearly exclusively due to direct collision-based interactions with the posts and is not greatly influenced by the electric field gradients between the posts.

Figure 7.6 shows the stretching effects of the obstacle array alone and gives some insight to the amount of preconditioning. It is clear that hooking polymers make up all of the extended molecules. The U/J collisions are more stretched than the broad distribution of X/W collisions, especially at higher field strengths. While by definition the U/J collisions must have a very sharp and highly extended distribution leaving the obstacle, the low field strengths allow some of the polymers, especially those slightly displaced from the centerline or those that collide with the first row of posts, time to relax before leaving the obstacle array. Accordingly, the distribution of U/J extensions leaving the array sharpens with increasing electric field. Comparing Figures 7.5 and 7.6, the distribution of extension leaving the posts clearly effects the distribution of extensions at the contraction. U/J collisions are grouped at the upper end of the distribution and do not appear to stretch further in the contraction, in agreement with the fact that the extension during a U/J collision saturates while the polymer is in contact with the post. X/W collisions stretch significantly in the contraction, but the broad distribution remains.

The broad extension distribution of the X/W collisions is expected from the nature of the

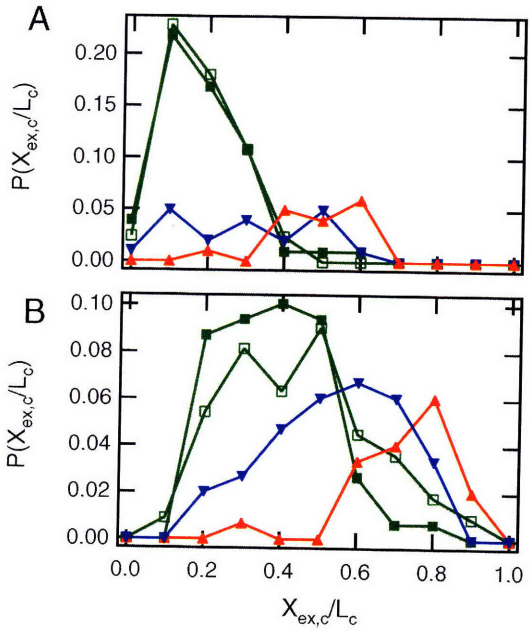

Fig. 7.5: *Histograms of relative stretch leaving the contraction for (a) De = 2 and (b) De = 7.* □ *represent all molecules in an obstacle-free channel,* ■ *represent non-hooking collisions in the obstacle array channel,* ▲ *represent U/J and* ▼ *represent X/W collisions. Data in the obstacle array channel are normalized such that the accumulated probability under the solid symbols is unity. The data in the obstacle-free channels is rescaled such that the integrated probability is set equal to that of the non-hooking molecules in the obstacle array channel (the area under the filled and open squares is the same). This rescaling was done to draw attention to the similarity between the* ■ *and* □ *curves. The fraction of molecules that hook is 44% for De = 2 and 63% for De= 7.*

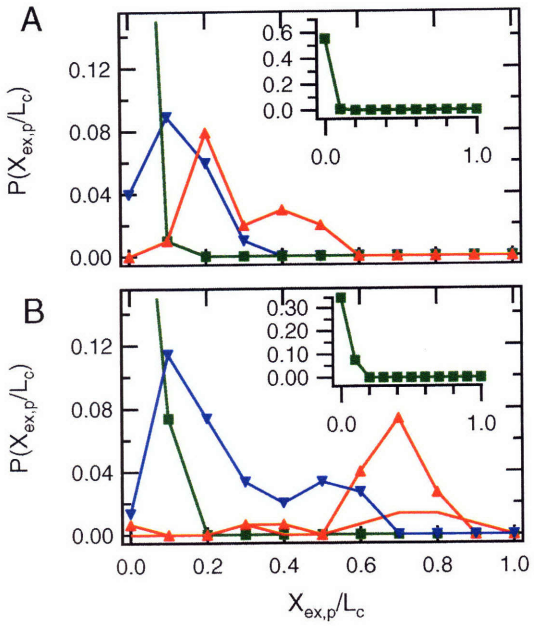

Fig. 7.6: *Histograms of relative stretch leaving the obstacle array at De = 2 (a) and De = 7 (b). The symbols are as defined in Figure 7.5. Insets are complete plots of the histograms for the non-hooking collisions.*

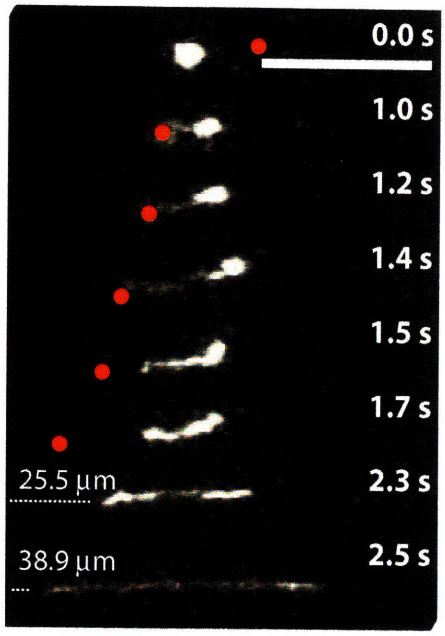

Fig. 7.7: *Time series images of a T4 DNA moving through the obstacle-array contraction device at De = 5. Each frame is re-centered on the molecule center of mass to allow for greater magnification and clarity. The post involved in the collision is drawn by hand, and the distance to the post is shown for the final two frames. The scale bar is 20 µm. The collision with the obstacle array is seen in the second and third frames (1.0 and 1.2 sec). The polymer then relaxes slightly (1.5 and 1.7 sec) before stretching again in the contraction (2.3 and 2.5 sec).*

collision type. At high field strengths in constant fields, the dynamics of the X collision have been described as a coil which freely convects downstream with the field and a nearly fully-stretched tail that connects the coil to the obstacle [15, 178]. In the current device, the field is not uniform near the post and one can expect some deformation of the convecting coil during the collision. However, these field-gradient effects are secondary to the direct collision effects, and at the end of the collision, one would expect the polymer to retain the major features of the coil-tail configuration as it moves into the contraction.

An example of this behavior can be seen in Figure 7.7, a time series image of an X-colliding T4 DNA molecule. The coil-tail configuration is clearly seen during the collision (1.0 and 1.2 sec). Even though there is some relaxation and reorganization of the polymer configuration between the collision and the contraction (1.4 to 1.7 sec), the stretched conformation retains some of the characteristics of the coil-tail. Most notably, the stretched conformation retains a fold at the front end, originating from the coiled part of the polymer while on the post. The highly pre-configured

tail stretches without folds in the contraction. The natural question to follow, then, is how small the coil must be, or better put, how much collision-pre-configuration must occur, to eliminate folds from the stretched polymers.

We can investigate the preconditioning effectiveness of the X/W collisions if the quantitative stretching at the end of the posts is taken into account. Figure 7.8 displays the extension at the end of the contraction versus the extension at the end of the obstacle array by collision type. The abscissa represents the amount of preconditioning incurred on a particular molecule, and varies from none to the extension expected after infinite strain. From these plots we can determine that the amount of preconditioning needed to effectively alter the stretching outcome is approximately 20%. Below 20% extension after the obstacle array, the distribution of stretch at the end of the contraction is similar to that if the polymer does not hook, i.e. as if the obstacle array were not there. Above 20% extension, the distribution shifts to more highly stretched polymers with a small return for further pre-deformation.

Upon closer examination of the conformation of the polymers at the end of the contraction (Figure 7.8f), the increase in stretch is correlated to the exclusion of heavily coiled conformations. This conformation type has been observed previously to stretch slowest [51, 52, 78]. Elimination of just this one type of conformation drastically changes the distribution of polymer behavior in the downstream contraction. Interestingly, the more extended polymers are a mix of "folded" and "stretched" conformations. "Folds" are only excluded in the high-preconditioning deformation limit. For applications such as Direct Linear Analysis [47, 172], which rely on the absence of folds, the preconditioning step appears to require U/J collisions in this device. However, significant increases in the stretch of the polymer occur for most collisions.

Figure 7.8 also points to possible methods to increase the effectiveness of the device. Since the resulting stretch in the contraction after a U/J collision is very near the infinite-strain stretch for the higher De the most straightforward method to increase the stretch is to increase the probability of an optimal preconditioning event. Hence, it is worthwhile to investigate these effects further.

The hooking probability of T4 DNA as a function of De and De_{obst} is given in Figure 7.9. Previous studies [11, 177] have found that the hooking probability on isolated, insulating posts depends on two parameters, De_{obst} and a ratio of length scales b/R_g where b is an offset parameter and R_g is the polymer equilibrium radius of gyration in the directions orthogonal to the cylinder axis. b describes the distance of nearest approach of the center of mass of the polymer to the center of the post without the field deformation effects due to the post. The field dependence (De_{obst}) originates in the fact that the DNA is actually deformed as it moves through the field gradients prior to the obstacle, dynamically increasing the polymer collision radius. At high field strengths, this effect saturates since the amount of pre-deformation cannot grow indefinitely in the finite strain prior to the post. In this high-field limit the problem becomes geometrically defined, as polymers on trajectories nearest to the center of the obstacle (low b) are more likely to hook. This trend is observed in the hooking probability for T4 DNA over all three rows of obstacles. At low fields, the hooking probability increases with increasing field strength, while at higher applied fields the probability reaches a plateau.

In a post array, the maximum offset parameter (b_{max}) is limited by the array geometry. Specifically, the offset parameter cannot exceed half of the spacing between obstacles transverse to the direction of the applied field. In the observation region of the current device, $b_{max} \approx 2\mu$m making $b_{max}/R_g \approx 2/1.4 \approx 1.4$ for T4 DNA. The collision probability due to a single post has nearly completely decayed at this value of the dimensionless offset parameter for $De_{obst} < 100$ [177] and

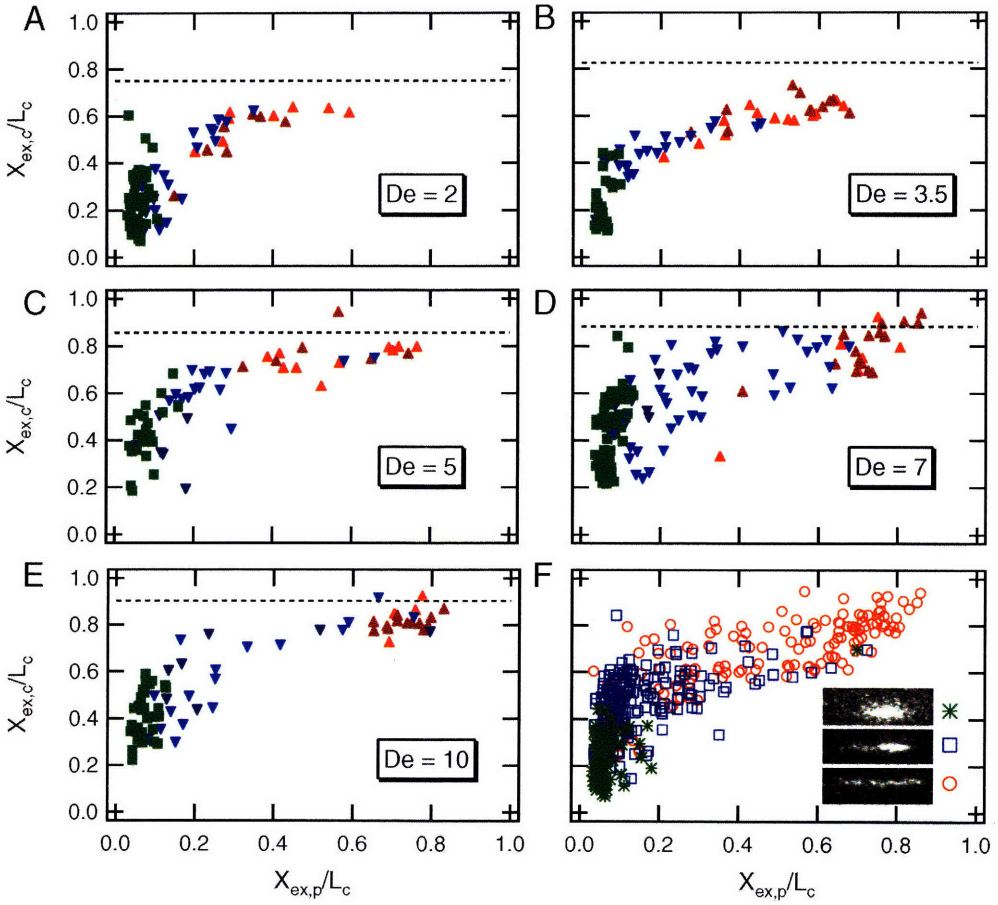

Fig. 7.8: *Scatter plots of the relative stretch at the end of the contraction versus the relative stretch at the end of the obstacle array for De denoted on plots in panes a-e where* ■ *denotes non-hooking collisions,* ▲ *U/J collisions and* ▼ *X/W collisions. Horizontal dotted lines are the stretch at infinite-strain from Eq 7.1. Pane f shows the same scatter plot broken down by conformation in the contraction for all De investigated with an inset definition of the coil/fold/stretch (top to bottom) categorization. Images taken from the De = 2 data set.*

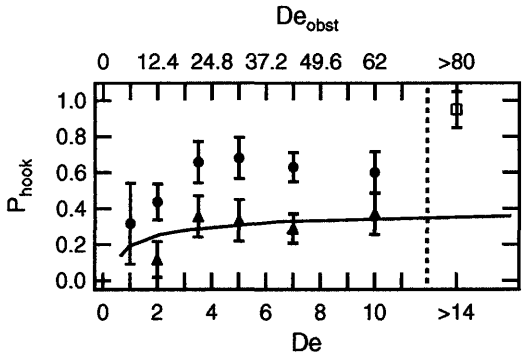

Fig. 7.9: *Measured hooking probability in the obstacle array (•) and on the first row of obstacles (▲) versus De and De_{obst}. Also shown is a calculated hooking probability for T4 DNA versus De and De_{obst} on the first row of posts using the results of single-post simulations [177]. The effect of changing the geometric parameters of the problem is shown by the collision probability of ligated λ-DNA in the same device (□).*

we therefore assume that the the presence of an obstacle does not effect the collision probability on neighboring obstacles. Further, if the DNA is equally distributed among electric field lines, the collision probability on the first row of posts can be computed as the average hooking probability on a single post from $b/R_g = 0$ to b_{max}/R_g. The first-row hooking probability as well as the calculated hooking probability (using quadrature from the results of Brownian dynamics hooking simulations in ref [177]) are also presented in Figure 7.9 and agree quite well considering the experimental scatter and the nature of the assumptions used.

We now take advantage of our understanding of these geometric considerations to increase the hooking probability in our device. If the collision radius of the polymer becomes large relative to the post spacing ($b_{max}/R_g \to 0$), one can expect higher, nearly unity, collision probabilities [177]. In our study, we ligated the single-stranded ends of λ-DNA to create polymers with an equilibrium size greater than the spacing between the posts (> 250 kbp, $R_{g,bulk} > 2.2\mu$m). These molecules are observed at an effective $De > 14$ for these ligated DNA, calculated through a simple scaling argument ($\tau \sim M_w^{1.8}$) [58]. It should be noted that these polymers are near the limit of strong confinement ($R_{g,bulk} \sim h$) where scalings with molecular weight become steeper [155]. Thus, the scalings used represent a lower bound for the *De*.

Of the 100 molecules observed, 95 hook on the obstacle array and more than 30 completely unravel before exiting the field of view (these polymers fully stretched exceed the dimensions of our observable field of view, see Figure 7.10). The dramatically increased hooking probability shows promise for a next-generation device. Since the only relevant length scales are the radius of gyration and the maximum offset parameter, the current results suggest that a more refined obstacle array may provide the same increased collision probability with smaller molecular weight polymers.

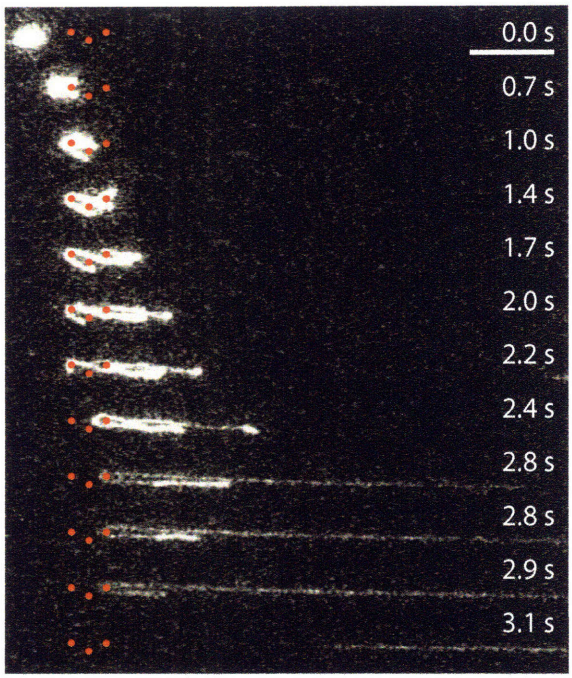

Fig. 7.10: *Time series image of a long DNA molecule (contour length ≈ 150 μm) moving through the obstacle array-contraction device. The width of each frame is the entire experimental field of view. The scale bar is 20 μm. Obstacles are drawn in as a frame of reference. The molecule collides with multiple posts before completely unraveling in the field of view.*

7.6 Conclusions

We have shown in this study that the presence of the obstacle array does increase the stretch of DNA through the contraction. We have used the existing collision categorization framework with small adjustments to characterize the effectiveness of different collision types. We have also characterized the effectiveness of varying extents of preconditioning and found that coiled conformations are excluded after approximately 20% pre-deformation. Exclusion of folds does not occur except for the most preconditioned molecules (U/J collisions), which nearly reach the steady-state stretch (infinite strain limit) in the contraction at high applied fields. Polymers which do not hook on the posts do not significantly differ in final stretch from polymers which translate through the same contraction without a obstacle array, implying that the preconditioning is due to hooking collisions alone. The probability of forming a hook in the obstacle array is shown to follow the same trends with electric field as for a single-post collision. The hooking probability increases for small applied fields and saturates at high fields. We also find that the hooking probability in the post array depends greatly on the ratio of the polymer equilibrium size and the array post spacing. Also, the hooking probability on the first row of the array is shown to agree well with extrapolations of the single-post problem.

This is the first experimental study to quantitatively link DNA pre-configuration by collision with an obstacle to later polymer stretching in an electric field gradient. These results are of importance for devices attempting to control the conformation of single molecules, where deterministic behavior is desired in a low-strain, flow-through device. The device itself is better suited for multi-sample use and is more scalable in design than previous contraction-flow preconditioning devices.

CHAPTER 8

Outlook

8.1 Conclusions and Impact on Field

The work presented in this thesis will have a significant impact on studies characterizing confined polymer dynamics as well as in the design of new devices using confinement to manipulate DNA molecules. If the future path of research follows current trends, that is single-molecule processing in channels of decreasing size, the groundwork laid out here will hold a significant place in the literature. We report experimental results providing a basis of comparison for future experiments and simulations concerning polymers in confinement. We also point out several limitations of current theory, and provide models and physical interpretations of our results, making possible the prediction of general polymer behavior.

The first major result of this work is evidence that hydrodynamic interactions are not important for molecular motion at scales larger than the channel height in slit-like confinement. Experimentally, this is shown through scalings of diffusivity with molecular weight. We attain the same result using a mathematical Zimm-inspired preaveraging analysis. Importantly, the transition to free-draining dynamics occurs precisely when the radius of gyration equals the channel height. This length scale had been assumed to be the hydrodynamic screening length scale for many years without rigorous proof. While these results are not surprising (they are rather relieving), these are the first studies reporting experimental evidence of the effects of hydrodynamic screening on long-length scale polymer motion in slit-like confinement.

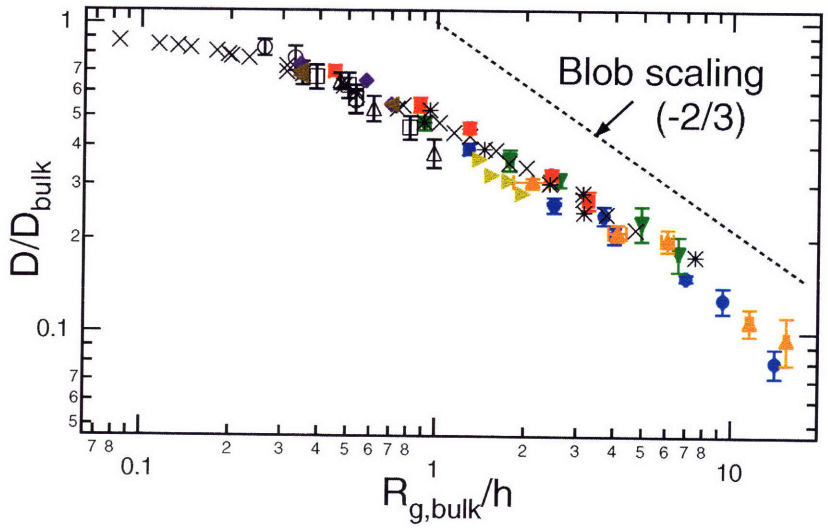

Fig. 8.1: *Compilation of diffusivity measurements in confinement.* ■, ▼, ●, *and* ▲ *represent M13mp18,* $1/2\lambda$, λ, *and* 2λ *DNA from Chapter 3 of this thesis.* × *and open symbols represent data from reference [142].* ∗ *represent data from Chapter 4 of this thesis.* ♦ *represent data from reference [14].* ◄ *represent unpublished data in our group.* ► *represent data from Chapter 5 of this thesis.*

A complete comparison and validation of de Gennes' blob theory is also provided. Aside from allowing the *a priori* calculation of DNA transport coefficients in confinement, we show that blob theory does not correctly account for hydrodynamic interactions within a blob (at short length scales). This shortfall causes a slightly lesser dependence of the transport coefficients on channel height than theory predicts. The study conclusively shows that blob theory is the appropriate theory to describe dynamics at equilibrium with the understanding that scalings with channel height must be fit from experimental data. We also show, however, that there is room for theoreticians to continue to investigate confinement effects on individual polymers, or rather, individual blobs within polymers. The detailed information of flows between plates on length scales shorter than the channel has yet to be incorporated correctly into theories predicting either the movement of colloids or polymers on these length scales.

Importantly, the work in this thesis demonstrates the fact that the dynamics of deformed polymers in slit-like confinement can vary drastically from those at equilibrium. The notion that a significantly deformed polymer would not interact with the confining walls had been put forward previously [73], but we experimentally determine the effects of these conformationally-dependent dynamics on the relaxation and stretching of single polymers. Relaxation of DNA from a stretched state in slit-like confinement displays two characteristic time scales, depending on the polymer extension, in the linear force regime. In terms of stretching DNA, we find that the *second longest*

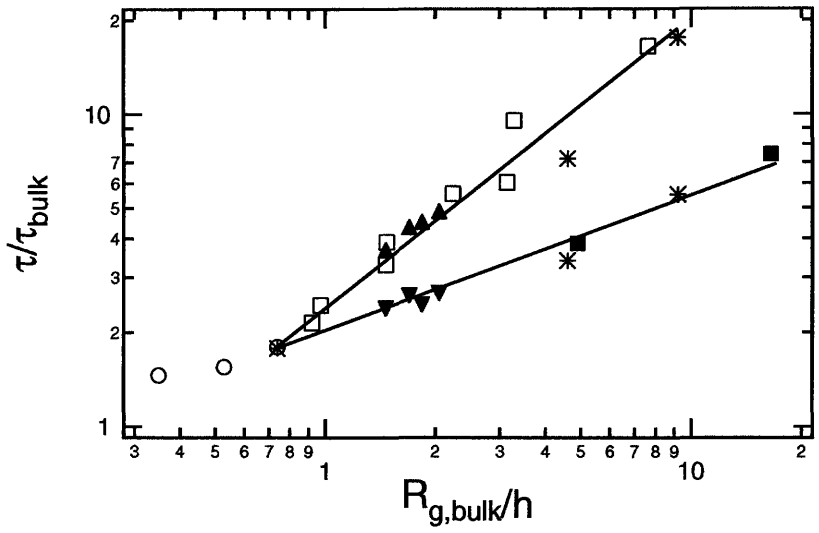

Fig. 8.2: *Compilation of relaxation time measurements in confinement.* ○ *represent data from reference [14].* □ *represent data from Chapter 4 of this thesis.* ▲ *and* ▼ *represent data from Chapter 5 of this thesis.* ■ *represent data from reference [92].* ∗ *represent data from Chapter 6 of this thesis.*

relaxation time governs a more moderate coil-to-stretch transition. The true longest relaxation time only governs small departures from equilibrium behavior, very different from bulk dynamics where the longest relaxation time is used to describe data to nearly full extension.

Finally, we demonstrate that other aspects of micro-fabrication have important uses when the level of detail in the structures made reaches that of the DNA molecule itself. We have demonstrated the effectiveness of the collision process to preconfigure DNA molecules for downstream stretching. At a more basic level, we have demonstrated the notion that the effects of the processing history of single molecules on downstream behavior are measurable and useful in terms of making the typically very individualistic behavior much more uniform.

As a whole, this thesis presents a major step forward in both the characterization of polymers in confinement and the tool set now available for the design of new devices. We hope to have set a strong fundamental foundation upon which future studies of polymeric behavior in confinement can be built. At the very least, we hope to have illustrated that polymer dynamics, especially deformed polymer dynamics, is nontrivial in confinement and the possibility of new time scales and length scales must be accepted. We also demonstrate the effects of processing history on downstream polymer dynamics, and one method for its use in increasing the efficiency of stretching devices. The ability to predict these effects and design devices to exploit (or avoid) them will greatly aid future single molecule analysis.

8.2 Future Work

As in any research, our results raise as many questions as they answer. The following sections describe some interesting, from my point of view, future studies ranging in scope from extensions of the parameter space investigated here to more applied aspects of DNA manipulation.

Odijk regime characterization

A simple suggestion to extend the work done here is to continue the characterization of DNA dynamics into smaller channels. Two pioneering studies in this area do exist [85, 86] but the results are not well understood and a complete experimental characterization of Odijk theory is not currently available.

One issue that remains to be resolved is the application of Odijk theory to slits. The original scalings were derived for polymers in pores with $r_{pore} \ll L_p$ (r_{pore} being the radius of the channel). Extrapolations of the theory to slits is interesting and highly nontrivial. For instance, in pores the relaxation time is predicted (and found) to decrease (relaxation speeds up) with decreasing channel height [85]. This oddity can be explained through the fact that the chain conformation is typically highly extended along the channel direction, with the amount of extension highly dependent on the channel radius. With such a large deviation from equilibrium conformation and force-extension behavior it is not completely surprising that the resulting dynamics are vastly different. However, in slits, the polymer is free to attain a 2d self-avoiding walk in the plane of the channel (see Figure 2.2). Since the channel height does not largely affect these quasi 2d configurations (i.e. the free energy with extension in the plane) one would not expect a large dependence of the ensuing long length and time scale dynamics on the channel height. However, short length and time scale motion (motions which do not require rearrangement of the entire molecule in the plane) should be highly dependent on the level on confinement. Thus, I expect short length and time scale motion to

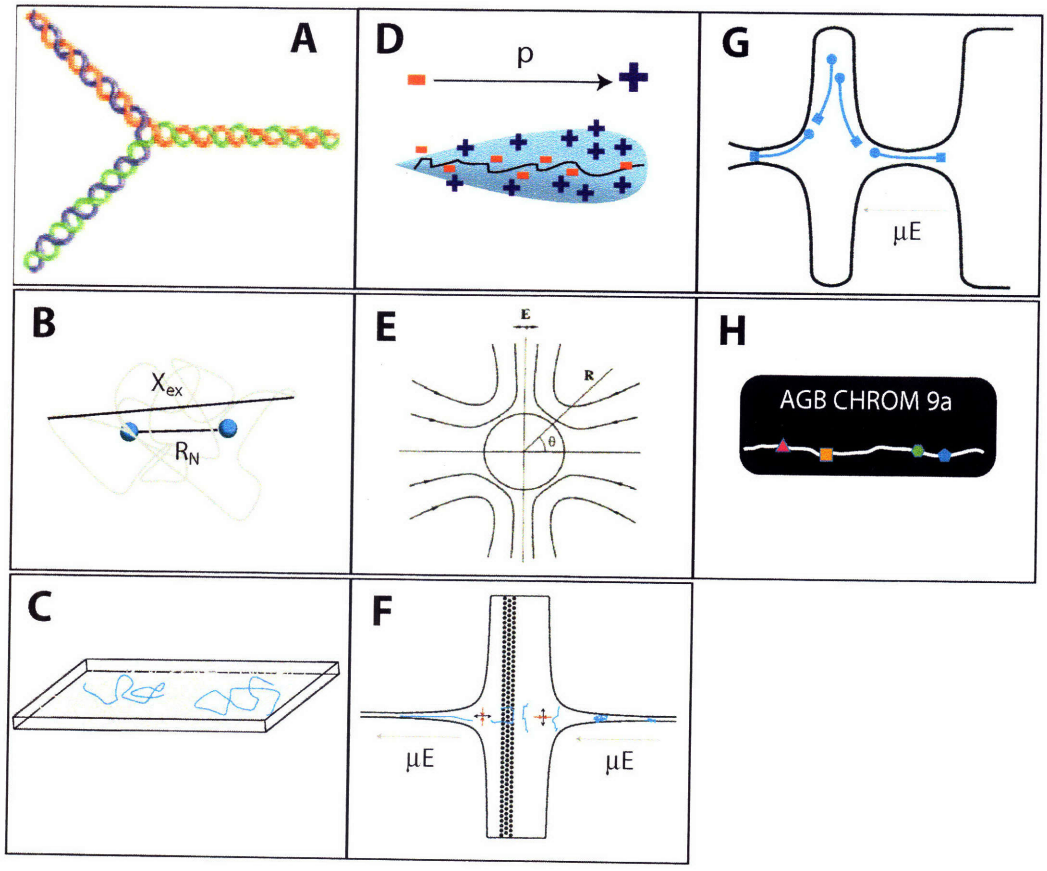

Fig. 8.3: *Schematics of future experimental setups, measurements, and physical mechanisms. A. Oligomers designed by Guo and co-workers to form Y-shaped branch points. Image from [185]. B. DNA end-labeled with quantum dots allows direct measurement of the end to end vector* $\boldsymbol{R_N}$*. C. Schematic of experimental setup for the study of individual polymers in a concentrated polymer solution. The blue line represents stained DNA and the gray lines unstained DNA. D. Schematic of a polarized double layer in an electric field. E. Figure of the streamlines of second-order EOF around a polarizable particle. Image from [186]. F. Schematic of pre-conditioning DNA to increase collision probability. Red and black arrows represent axes of compression and elongation, respectively. Increasing the extension of the DNA transverse to the posts increases the collision probability. G. Schematic of "turning around" phenomenon in contraction/expansion channels. H. A schematic of a labeled, DNA-laden solid tablet created with our stop-flow-lithography set up.*

follow vastly different scalings than the long length-scale and timescale motion. It should be noted here that in the limit of a two-dimensional system, a single relaxation time is expected to govern dynamics. Thus, at some point (presumably in the Odijk regime) the two timescales discussed in this work must converge and revert to a single timescale.

Challenges particular to working in the Odijk regime are the fact that the dynamics are expected to slow down greatly. If sufficiently long observation times are not used, long length and time scale motion is not observed and the dynamics may be assumed to be faster than they actually are. For instance, we find that an observation time on the order of 20 to 30 times longer than the timescale of interest is needed to be able to discern physics at those scales. The rotational relaxation time for T4-DNA is $\sim 15 - 20$s requiring observation times of ~ 10 minutes to accurately measure the longest mode of polymer motion [58]. Also, Odijk [187] has predicted the possible existence of several regimes between Odijk and blob theory, making comparison to the correct theory more difficult.

End-tagged and branched chain dynamics

Recently, researchers have developed single-stranded DNA oligomers that self-assemble into branched structures (three and four points of functionality, see Figure 8.3A) [185]. This development, in conjunction with our experimental setup, would allow the visualization of branched polymer dynamics as well as a host of other studies. While the direct applications to DNA mapping would be lost (i.e. DNA in nature is not branched), the direct observation of the dynamics of single branched polymers in rheological flows could benefit that field immensely. Currently branch point and molecular weight control is still limited by industrial polymerization techniques, which have been much improved recently, but still lag behind biological polymers and recombinant syntheses.

The level of molecular control may also be applied to "sticking" colloids and other measurable entities (tags) to the DNA molecule itself. Slater has shown that appending colloids or even polymers or proteins to the end of DNA drastically alters its dynamics in electric fields. Even if the tag is significantly small (say a quantum dot, $r \sim 5 - 20$nm), if the charge density on that object is different than that on DNA, tension in the chain may result. This effect can be a complication for studies using tags to selectively monitor certain sections of DNA, however, turning lemons into sweeter lemons, these effects may lead to insights on the dynamics of block co-polymers and general polyampholytes in electric fields.

In the absence of electric fields, observation of individual polymer segments may provide a more direct comparison to polymer theory. Polymer theory, as seen in Chapter 2, is largely derived in terms of the end-to-end vector of the chain, which is yet to be directly measured. Appending quantum dots to the end of DNA molecules may allow the direct observation of these ends (see Figure 8.3B) without significantly altering the dynamics of the polymer (testable, for instance, by comparing the diffusivity of the tagged and untagged polymer). The dots can then be tracked in all three dimensions (using calibrations of the power spectral function of the objective lens used), allowing time correlations of the end to end vector to be calculated and evaluated. These results would provide the most direct comparison to polymer theory.

Concentrated solutions in confinement

While the work in this thesis is mainly concerned with the dynamics of single molecules in confinement, the dynamics of polymers in a sea of other polymers is an interesting area of research.

Recently, researchers have used mixtures of stained and unstained DNA molecules to observe single DNA in concentrated solutions (see Figure 8.3C). Multiple timescales are observed in these systems as relaxation within the reptative tube occurs simultaneously with relaxation and rearrangement of the tube itself [146, 148, 188]. Mixing of these timescales with the separation of time scales based on extension in confinement may generate interesting long timescale physics with four possible slow modes of motion. Flow properties of these solutions in small spaces, then, should be interesting and non-trivial. Dynamics of more concentrated polymers in thin layers and pores may have applications in oil drilling as well as in the paints and coatings fields. The ability to observe single DNA within high-concentration solutions in controllable geometries can provide the basis for very systematic rheological studies with unprecedented experimental control.

Nonlinear and second-order electrophoretic effects

At high electric fields (O(kV/cm)), a host of effects stemming from the polarizability of the electrical double layer surrounding the DNA may become important 8.3D. All non-linear electrophoretic effects are lumped into the term "dielectrophoresis" (DEP). While these forces tend to be small relative to electrophoretic forces at small fields, higher fields and use of alternating current devices may make them important. These forces have been shown to stretch DNA on their own accord and therefore may be used to manipulate the DNA conformation. A complete understanding of the forces and their origins at this point is somewhat lacking due to the high number of mechanisms that could possibly be at play. For instance, the EDL polarization can generate forces in electric field gradients, but can also create non-uniform electro-hydrodynamic effects [189] and associated instabilities.

Also, second order electro-osmotic flow effects may become important to study in their own right. For instance, arrays of conducting obstacles have been used as electroosmotic pumps, but insulating obstacles are theorized to disturb the regular EOF flow pattern as well [186, 190] (see Figure 8.3E). While we do not observe these effects in our experiments, more detailed studies may want to consider them as they may alter DNA dynamics in post and post-array devices. Also, recent studies have considered eddy formation [191] and pressure-driven back-flow [192] in electroosmotic flow through microchannel contractions.

Recent evidence suggests that there may be a conformation-dependent DNA mobility. While these effects are not measurable in current experiments, they have been observed, for instance, just after DNA collisions (with polymers in my experience) in a constant electric field. There, the velocity is observed to increase by a factor of 2 to 4 [19]. The change in DNA mobility may be very important in design applications if it is indeed an artifact of the conformation. Unpublished data in microchannel contractions does exist at this point (see http://www.nsec.ohio-state.edu/briefs/Instantaneous.pdf as of the publication date of this thesis), but difficulties in the measurement cause me to doubt the results. In my opinion, isolation of the conformation as the cause of the increase in mobility (i.e., DEP effects are not treated, precise descriptions of the calculation of the local electric field and forces on the DNA are not described, and the possibility of EOF effects is not considered) as well as statistical proof of the correlation have yet to be shown. In my opinion, measurement of the mobility in a microchannel contraction is not the optimal experiment in which to measure this phenomenon as it may introduce several complicating factors. A simpler experiment is to simply extend the DNA on a post in a uniform electric field and compare the average velocity of molecules after leaving the post (in the uniform field) to those that did not

contact the post.

Optimization of post array devices: length scales and multiple preconditioning steps

In a more applied direction, there is room for optimization of the current post-array preconditioning device. The preconditioning (collision) matrix is one area of improvement. The possibility of using laser interference lithography or a bead-patterned hydrogel may provide a higher collision probability while retaining the open-ness of the post array. Here we hypothesize that a more refined meshing of the post array will improve collision probability, but the shape and organization of the posts are other design parameters that may alter collision probabilities. The location of the post array relative to the contraction is another variable not focused upon in the current work. Modulation of this distance can be quite interesting as a method to test the time-dependence of the preconditioning effect, i.e., how quickly the molecule looses memory of the collision. Work here will experimentally prove the existence of separate timescales for stress and conformational relaxation.

With the current obstacle array, dynamically increasing the collision radius may improve the efficiency of the device. For instance, stretching the polymer transverse to the direction of travel will greatly increase the likelihood the polymer will interact with a post (the collision length scale of the polymer goes from R_g to the order of L_c, a 30-fold increase for T4 DNA, see Figure 8.3F). This can be attained, for instance, by placing a microchannel expansion directly prior to the obstacle array. In fact, by operating the post-preconditioning device in reverse (as done for the relaxation experiments in Chapter 5 in a 1 micron tall channel), we see a greatly enhanced collision probability with many polymers hooking over multiple posts in a single row of posts. No such collisions were observed for the work in Chapter 7 where the molecules were in an equilibrium conformation before impinging on a post.

The length scale of the contraction is a design variable that has yet to be studied in detail. Currently, the contraction length is on the order of the contour length of T4 DNA, set more out of convenience and compatibility with our imaging setup than any particular design principle. In fact, the contraction length sets the residence time in the contraction at a given De, and as such should affect the stretch observed. It may be an interesting study to measure stretch at the end of several contractions of differing length in an attempt to extrapolate to a step-change in field strength or mobility. Results could then be compared to newly developed theory [176].

An interesting observation

Early in this work, a channel with a repeating contraction-expansion design motif was created. There we noted an interesting phenomenon where extended molecules would enter an expansion and advect into regions of slow streamlines away from the centerline. The polymer would then *turn around* and the tail of the molecule would enter the next contraction first (see Figure 8.3G). The turning around of the molecule points to the fact that the head and tail of the molecule are systematically forced to migrate across streamlines (the head to slower streamlines and the tail to faster streamlines). Cross-streamline migration is an important phenomenon to understand since it forms the basis of microfluidic mixing and separation (H-filter devices) and concentration devices. Recent simulations have found systematic migration occurs toward the channel wall for DNA electrophoretically driven through the device used in Chapter 7 (to a degree not experimentally observable). This migration may be a general phenomenon of deformable objects on curved streamlines and may form the basis for future DNA manipulation and separation devices.

Freezing of DNA conformations

Sometimes research follows somewhat ironic and circuitous paths, and it is fitting here to mention one of those possibilities now being investigated in our lab. The very first direct-analysis study actually "froze" DNA in an agarose gel before observation [30], allowing precise measurement of the location of restriction enzyme active sites along the DNA molecule. The fact that the DNA does not move allows prolonged observation of the "tags," allowing integration of sometimes very small signals and precise location of the tag along the DNA backbone. In our lab, the development of continuous flow lithography [193] and stop-flow lithography [194] may allow the capturing of specific DNA conformations (now with a resolution on the order of ms) in biologically-friendly poly-ethylene glycol hydrogels. In essence these experiments are an attempt to repeat the freezing motif, but with greatly enhanced time resolution and throughput. Since we now know, to a better extent, the behavior of DNA in microfluidic devices, it may be possible to design devices that allow the "freezing" of DNA molecules in highly extended configurations. The product of the reaction is a solid micro-tablet, capable of carrying a label to identify the extended DNA molecule held within (see Figure 8.3H). If it can be shown that enzymatic activity can occur within these tablets (so that DNA can be tagged after being "frozen"), our ability to precisely map genetic sequences will be greatly enhanced.

Bibliography

[1] Lander, E. S.; et al., *Nature* **2001**, *409*, 860.

[2] Mikkelsen, T.; Hillier, L.; Eichler, E.; Zody, M.; Jaffe, D.; Yang, S.-P.; Enard, W.; Hellman, I.; Lindblad-Toh, K.; Altheide, T.; Archidiacono, N.; Bork, P.; Butler, J.; Chang, J.; Cheng, Z.; Chinwalla, A.; deJong, P.; Delehaunty, K.; Fronick, C.; Fulton, L.; Gilad, Y.; Glusman, G.; Gnerre, S.; Graves, T.; Hayakawa, T.; Hayden, K.; Huang, X.; Ji, H.; Kent, W.; King, M.-C.; III, E. K.; Lee, M.; Liu, G.; Lopez-Otin, C.; Makova, K.; Man, O.; Mardis, E.; Mauceli, E.; Miner, T.; Nash, W.; Nelson, J.; Pbo, S.; Patterson, N.; Pohl, C.; Pollard, K.; Prfer, K.; Puente, X.; Reich, D.; Rocchi, M.; Rosenbloom, K.; Ruvolo, M.; Richter, D.; Schaffner, S.; Smit, A.; Smith, S.; Suyama, M.; Taylor, J.; Torrents, D.; Tuzun, E.; Varki, A.; Velasco, G.; Ventura, M.; Wallis, J.; Wendl, M.; Wilson, R.; Lander, E.; Waterston, R., *Nature* **2005**, *437*, 69.

[3] Olive, D. M.; Bean, P., *J. Clin. Microbiol.* **1999**, *37*, 1661.

[4] Barron, A.; Soane, D.; Blanch, H., *J. Chromatogr. A* **1993**, *25*, 3.

[5] Beale, S., *Anal. Chem.* **1998**, *70*, 279R.

[6] Albarghouthi, M. N.; Barron, A. E., *Electrophoresis* **2000**, *21*, 4096.

[7] Meagher, R. J.; Won, J. I.; McCormick, L. C.; Nedelcu, S.; Bertram, M. B. J.-L.; Drouin, G.; Barron, A.; Slater, G., *Electrophoresis* **2005**, *26*, 331.

[8] Volkmuth, W. D.; Austin, R. H., *Nature* **1992**, *358*, 600.

[9] Volkmuth, W. D.; Duke, T.; Wu, M. C.; Austin, R. H., *Phys. Rev. Lett.* **1994**, *72*, 2117(4).

[10] Nixon, G. I.; Slater, G. W., *Phys. Rev. E* **1994**, *50*, 5033.

[11] Saville, P. M.; Sevick, E. M., *Macromolecules* **1999**, *32*, 892.

[12] Sevick, E. M.; Williams, D. R. M., *Phys. Rev. E* **1994**, *50*, 3357.

[13] Sevick, E. M.; Williams, D. R. M., *Phys. Rev. Lett.* **1996**, *76*, 2595.

[14] Randall, G. C., *PhD Thesis, Massachusetts Institute of Technology* **2006**.

[15] Randall, G. C.; Doyle, P. S., *Macromolecules* **2006**, *39*, 7734.

[16] Turner, S. W.; Perez, A. M.; Lopez, A.; Craighead, H. G., *J. Vac. Sci. Technol. B* **1998**, *16*, 3835.

[17] Kaji, N.; Tezuka, Y.; Takamura, Y.; Ueda, M.; Nishimoto, T.; Nakanishi, H.; Horiike, Y.; Baba, Y., *Anal. Chem.* **2004**, *76*, 15.

[18] Doyle, P. S.; Bibette, J.; Bancaud, A.; Viovy, J.-L., *Science* **2002**, *295*, 2237.

[19] Minc, N.; Fütterer, C.; Dorfman, K.; Bancaud, A.; Gosse, C.; Goubault, C.; Viovy, J.-L., *Anal. Chem.* **2004**, *76*, 3770.

[20] Dorfman, K. D., *Phys. Rev. E* **2006**, *73*, 061922.

[21] Minc, N.; Viovy, J.-L.; Dorfman, K. D., *Phys. Rev. Lett.* **2005**, *94*, 198105.

[22] Bakajin, O.; Duke, T. A. J.; Tegenfeldt, J.; Chou, C.-F.; Chan, S. S.; Austin, R. H.; Cox, E. C., *Anal. Chem.* **2001**, *73*, 6053.

[23] Cross, J. D.; Strychalski, E. A.; Craighead, H. G., *J. Appl. Phys.* **2007**, *102*, 024701.

[24] Han, J.; Turner, S.; Craighead, H., *Phys. Rev. Lett.* **1999**, *83*, 1688.

[25] Han, J.; Craighead, H., *Science* **2000**, *288*, 1026.

[26] Han, J.; Craighead, H., *Anal. Chem.* **2002**, *74*, 394.

[27] Oana, H.; Ueda, M.; Washizu, M., *Biochem and Biophys. Res.* **1999**, *265*, 140.

[28] Chan, T.-F.; Ha, C.; Phong, A.; Cai, D.; Wan, E.; Leung, L.; Kwok, P.-Y.; Xiao, M., *Nucleic Acids Research* **2006**, *34*, e113.

[29] Latreille, P.; Norton, S.; Goldman, B. S.; Hankhaus, J.; Miller, N.; Barbazuk, B.; Bode, H. B.; Darby, C.; Du, Z.; Forest, S.; Gaudriault, S.; Goodner, B.; Goodrich-Blair, H.; Slater, S., *BMC Genomics* **2007**, *8*, 321.

[30] Schwartz, D. C.; Li, X.; Hernandez, L. I.; Ramnarain, S. P.; Huff, E. J.; Wang, Y.-K., *Science* **1993**, *262*, 110.

[31] Davenport, R. J.; Wuite, G. T. J.; Landick, R.; Bustamante, C., *Science* **2000**, *287*, 2497.

[32] Wang, M. D.; Yin, H.; Landick, R.; Gelles, J.; Block, S. M., *Biophys. J.* **1997**, *72*, 1335.

[33] Maier, B.; Bensimon, D.; Croquette, V., *Proc. Natl. Acad. Sci.* **2000**, *97*, 12002.

[34] Strick, T. R.; Allemand, J.-F.; Bensimon, D.; Bensimon, A.; Croquette, V., *Science* **1996**, *271*, 1835.

[35] Perkins, T.; Smith, D.; Larson, R.; Chu, S., *Science* **1995**, *268*, 83.

[36] Feree, S.; Blanch, H., *Biophysical Journal* **2003**, *85*, 2539.

[37] Kabata, H.; Kurosawa, O.; nd M. Washizu, I. A.; Margarson, S. A.; Glass, R. E.; Shimamoto, N., *Science* **1993**, *262*, 1561.

[38] Namasivayam, V.; Larson, R. G.; Burke, D. T.; Burns, M. A., *Anal. Chem.* **2002**, *74*, 3378.

[39] Xiao, M.; Phong, A.; Ha, C.; Chan, T.-F.; Cai, D.; Leung, L.; Wan, E.; Kistler, A. L.; DeRisi, J. L.; Selvin, P. R.; Kwok, P.-Y., *Nucleic Acids Research* **2006**, *35*, e16.

[40] Bensimon, D.; Simon, A. J.; Croquette, V.; Bensimon, A., *Phys. Rev. Lett.* **1995**, *74*, 4754.

[41] Crut, A.; Lanse, D.; Allemand, J.-F.; Dahan, M.; Desbiolles, P., *Phys. Rev. E* **2003**, *67*, 051910.

[42] Smith, S.; Cui, Y.; Bustamante, C., *Science* **1996**, *271*, 795.

[43] Dukkipati, V.; Kim, J. H.; Pang, S. W.; Larson, R. G., *Nano Letters* **2006**, *6*, 2499.

[44] Douville, N.; Huh, D.; Takayama, S., *Anal. Bioanal. Chem.* **2008**.

[45] Riehn, R.; Lu, M.; Wang, Y.-M.; Lim, S. F.; Cox, E. C.; Austin, R. H., *Proc. Nat. Acad. Sci. USA* **2005**, *102*, 10012.

[46] Jo, K.; Dhingra, D. M.; Odijk, T.; de Pablo, J. J.; Graham, M. D.; Runnheim, R.; Forrest, D.; Schwartz, D. C., *Proc. Nat. Acad. Sci. USA* **2007**, *104*, 2673.

[47] Larson, J. W.; Yantz, G. R.; Zhong, Q.; Charnas, R.; DAntoni, C. M.; Gallo, M. V.; Gillis, K. A.; Neely, L. A.; Phillips, K. M.; Wong, G. G.; Gullans, S. R.; Gilmanshin, R., *Lab Chip* **2006**, *9*, 1187.

[48] Randall, G. C.; Schultz, K. M.; Doyle, P. S., *Lab Chip* **2006**, *6*, 516.

[49] Kim, J. M.; Doyle, P. S., *Lab Chip* **2007**, *7*, 213.

[50] Chan, E. Y.; Goncalves, N. M.; Haeusler, R. A.; Hatch, A. J.; Larson, J. W.; Maletta, A. M.; Yantz, G. R.; Carstea, E. D.; Fuchs, M.; Wong, G. G.; Gullans, S. R.; Gilmanshin, R., *Genome Res.* **2004**, *14*, 1137.

[51] Perkins, T.; Smith, D.; Chu, S., *Science* **1997**, *276*, 2016.

[52] Smith, D.; Chu, S., *Science* **1998**, *281*, 1335.

[53] de Gennes, P. G., *Science* **1997**, *276*, 1999.

[54] Squires, T.; Quake, S., *Rev. Mod. Phys.* **2005**, *77*, 977.

[55] Rubenstein, M.; Colby, R. H., *Polymer Physics*, Oxford University Press, New York 2003.

[56] Flory, P. J., *Statistical Mechanics of Chain Molecules*, Hanser/Gardner Publications, New York 1969.

[57] Smith, D. E.; Perkins, T. T.; Chu, S., *Macromolecules* **1996**, *29*, 1372.

[58] Doi, M.; Edwards, S. F., *The Theory of Polymer Dynamics*, Oxford University Press, Oxford, New York 1986.

[59] Marko, J. F.; Siggia, E. D., *Macromolecules* **1995**, *28*, 8759.

[60] Underhill, P. T.; Doyle, P. S., *J. Rheol.* **2005**, *49*, 963.

[61] Underhill, P. T.; Doyle, P. S., *J. Rheol.* **2006**, *50*, 513.

[62] Deen, W. M., *Analysis of Transport Phenomena*, Oxford University Press, New York 1998.

[63] Lee, J. S.; Shaqfeh, E. S. G.; Muller, S. J., *Phys. Rev. E* **2007**, *75*, 040802(R).

[64] Schroeder, C. M.; Teixeira, R. E.; Shaqfeh, E. S. G.; Chu, S., *Phys. Rev. Lett.* **2005**, *95*, 018301.

[65] Hur, J.; Shaqfeh, E. S. G.; Babcock, H. P.; Smith, D. E.; Chu, S., *J. Rheology* **2001**, *45*, 421.

[66] Beck, V. A.; Shaqfeh, E. S. G., *J. Rheol.* **2007**, *51*, 561.

[67] Larson, R. G.; Hu, H.; Smith, D. E.; Chu, S., *J. Rheol.* **1999**, *43*, 267.

[68] Hur, J. S.; Shaqfeh, E. S. G.; Babcock, H. P.; Chu, S., *Phys. Rev. E* **2002**, *66*, 011915.

[69] Hoffman, B. D.; Shaqfeh, E. S. G., *J. Rheol.* **2007**, *51*, 947.

[70] Magda, J. J.; Larson, R. G.; Mackay, M. E., *J. Chem. Phys.* **1988**, *89*, 2504.

[71] Larson, R. G.; Magda, J. J., *Macromolecules* **1989**, *22*, 3004.

[72] Brochard-Wyart, F., *Euro. Phys. Lett.* **1995**, *30*, 387.

[73] Brochard-Wyart, F., *EuroPhys. Lett.* **1993**, *23*, 105.

[74] Brochard-Wyart, F.; Hervet, H.; Pincus, P., *Euro. Phys. Lett.* **1994**, *26*, 511.

[75] Manneville, S.; Cluzel, P.; Viovy, J.-L.; Chatenay, D.; Caron, F., *Europhys. Lett.* **1996**, *36*, 413.

[76] Schroeder, C.; Babcock, H.; Shaqfeh, E.; Chu, S., *Science* **2003**, *301*, 1515.

[77] de Gennes, P. G., *J. Chem. Phys* **1974**, *60*, 5030.

[78] Larson, R. G., *J. Non-Newtonian Fluid Mech.* **2000**, *94*, 37.

[79] Brochard, F.; de Gennes, P. G., *J. Chem. Phys.* **1977**, *67*, 52.

[80] Daoud, M.; de Gennes, P. G., *J. Phys. (Paris)* **1977**, *38*, 85.

[81] Brochard, F., *J. Phys. (Paris)* **1977**, *38*, 1285.

[82] Liron, N.; Mochon, S., *J. Eng. Math.* **1976**, *10*, 287.

[83] Happel, J.; Brenner, H., *Low Reynolds number hydrodynamics*, Kluwer, Boston 1983.

[84] Odijk, T., *Macromolecules* **1983**, *16*, 1340.

[85] Reisner, W.; Morton, K. J.; Riehn, R.; Wang, Y. M.; Yu, Z.; Rosen, M.; Sturn, J. C.; Chou, S. Y.; Frey, E.; Austin, R. H., *Phys. Rev. Lett.* **2005**, *94*, 196101.

[86] Dekker, C.Personal Communication.

[87] Evans, D. F.; Wennerström, H., *The Colloidal Domain: where physics, chemistry, biology, and technology meet, Second Edition*, Wiley-VCH, New York 1999.

[88] Hsieh, C.-C.; Balducci, A.; Doyle, P., *Nano Letters* **2008**, *8*, 1683.

[89] Long, D.; Dobrynin, A. V.; Rubenstein, M.; Ajdari, A., *J. Chem. Phys.* **1998**, *108*, 1234.

[90] Long, D.; Viovy, J.-L.; Ajdari, A., *J. Phys.: Condens. Matter* **1996**, *8*, 9741.

[91] Long, D.; Ajdari, A., *Eur. Phys. J. E* **2001**, *4*, 29.

[92] Bakajin, O. B.; Duke, T. A. J.; Chou, C. F.; Chan, S. S.; Austin, R. H.; Cox, E. C., *Phys. Rev. Lett.* **1998**, *80*, 2737.

[93] Cao, H.; Yu, Z.; Wang, J.; Tegendfelt, J. O.; Austin, R. H.; Chen, E.; Wu, W.; Chou, S. Y., *App. Phys. Lett.* **2002**, *81*, 174.

[94] Mao, P.; Han, J., *Lab Chip* **2005**, *5*, 837.

[95] Tegenfedlt, J. O.; Prinz, C.; Cao, H.; Chou, S.; Reisner, W.; Riehn, R.; Wang, Y. M.; Cox, E. C.; Sturm, J. C.; Silberzan, P.; Austin, R. H., *Proc. Nat. Acad. Sci.* **2004**, *101*, 10979.

[96] Inatomi, K.; Izuo, S.; Lee, S.; Ohji, H.; Shiono, S., *Microelectronic Engineering* **2003**, *70*, 13.

[97] Tegenfeldt, J. O.; Prinz, C.; Cao, H.; Huang, R. L.; Austin, R. H.; Chou, S. Y.; Cox, E. C.; Sturm, J. C., *Anal. Bioanal. Chem.* **2004**, *378*, 1678.

[98] P. S. Doyle *et al.*, *Science* **2002**, *295*, 2237.

[99] Pennathur, S.; Santiago, J. G., *Anal. Chem.* **2005**, *77*, 6772.

[100] Pennathur, S.; Santiago, J. G., *Anal. Chem.* **2005**, *77*, 6782.

[101] Y.-L. Chen *et al.*, *Phys. Rev. E* **2004**, *70*, 060901(4).

[102] O. B. Bakajin *et al.*, *Phys. Rev. Lett.* **1998**, *80*, 2737.

[103] Burkhardt, T. W., *J. Phys. A: Math. Gen.* **1997**, *30*, L167.

[104] Deen, W. M., *AIChE J.* **1987**, *33*, 1409.

[105] Wall, F. T.; Seitz, W. A.; Chin, J. C.; de Gennes, P. G., *Proc. Natl. Acad. Sci. USA* **1978**, *75*, 2069.

[106] Maier, B.; Radler, J. O., *Macromolecules* **2000**, *33*, 7185.

[107] Maier, B.; Radler, J. O., *Phys. Rev. Lett.* **1999**, *82*, 1911.

[108] Flory, P. J., *Principles of Polymer Chemistry*, Cornell University Press, Cornell University 1953.

[109] Choi, M. C.; Santangelo, C. D.; Pelletier, O.; Kim, J. H.; Kwon, S.; Wen, Z.; Li, Y.; Pincus, P. A.; Safinya, C. R.; Kim, M. W., *Macromolecules* **2005**, *38*, 9882.

[110] Koster, S.; Steinhauser, D.; Pfohll, T., *J. Phys.: Condes. Matter* **2005**, *17*, S4091.

[111] Morse, D. C., *Macromolecules* **1998**, *31*, 7044.

[112] Alvarez, A.; Soto, R., *Phys. Fluids* **2005**, *17*, 093103.

[113] Diamant, H.; Cui, B.; Lin, B.; Rice, S. A., *J. Phys.: Condes. Matter* **2005**, *17*, S2787.

[114] Lin, Y.-W.; Huang, C.-C.; Chang, H.-T., *Anal Bioanal Chem* **2003**, *376*, 379.

[115] Cui, B.; Diamant, H.; Lin, B.; Rice, S. A., *Phys. Rev. Lett.* **2004**, *92*, 258301.

[116] Perkins, T. 1997, *Exploring Polymer dynamics with single DNA molecules*, Ph.D. thesis, Stanford University.

[117] Stellwagen, N. C.; Gelfi, C.; Righetti, P. G., *Biophys. J.* **2000**, *54*, 137.

[118] Goodman, A.; Tseng, Y.; Wirtz, D., *J. Mol. Biol.* **2002**, *323*, 199.

[119] Savin, T.; Doyle, P. S., *Biophys. J.* **2005**, *88*, 623.

[120] Hsu, H.-P.; Grassberger, P., *J. Chem. Phys.* **2004**, *120*, 2034.

[121] Jendrejack, R. M.; Schwartz, D. C.; Graham, M. D.; de Pablo, J. J., *J Chem. Phys.* **2003**, *119*, 1165.

[122] Harden, J. L.; Doi, M., *J. Phys. Chem* **1992**, *96*, 4046.

[123] Dechadilok, P.; Deen, W. M., *Ind. Eng. Chem. Res.* **2006**, *45*, 6953.

[124] Woo, N. J.; Shaqfeh, E. S. G.; Khomami, B., *J. Rheol.* **2004**, *48*, 281.

[125] Tlusty, T., *Macromolecules* **2006**, *39*, 3927.

[126] van Vliet, J. H.; ten Brinke, G., *J. Chem. Phys.* **1990**, *93*, 1436.

[127] Haber, C.; Ruiz, S. A.; Wirtz, D., *Proc. Natl. Acad. Sci.* **2000**, *97*, 10792.

[128] Bird, R. B.; Curtiss, C. F.; Armstrong, R. C.; Hassager, O., *Dynamics of Polymeric Liquids, Volume 2: Kinetic Theory*, Wiley-Interscience, New York 1987, 2 edn.

[129] Graessley, W. M., *Polymeric Liquids and Networks: Structure and Properties*, Garland Science, New York 2004.

[130] de Gennes, P.-G., *Scaling Concepts in Polymer Physics*, Cornell University Press, New York 1979.

[131] Pozrikidis, C., *Introduction to Theoretical and Computational Fluid Dynamics*, Oxford University Press, New York 1997.

[132] Wang, Y.-C.; Choi, M. H.; Han, J., *Anal. Chem.* **2004**, *76*, 4426.

[133] Lagerqvist, J.; Zwolak, M.; Ventra, M. D., *Nanoletters* **2006**, *6*, 779.

[134] Fu, J.; Schoch, R. B.; Stevens, A. L.; Tannenbaum, S. R.; Han, J., *Nature Nanotechnology* **2006**, *2*, 121.

[135] Stein, D.; van der Heyden; W. A. Koopmans, F. H. J.; Dekker, C., *Proc. Nat. Acad. Sci.* **2006**, *103*, 15853.

[136] Jendrejack, R. M.; Dimalanta, E. T.; Shwartz, D. C.; Graham, M. D.; de Pablo, J. J., *Phys. Rev. Lett* **2003**, *91*, 038102.

[137] Odijk, T., *J. Chem. Phys.* **2006**, *125*, 204904.

[138] Stigter, D., *Biophys. Chem.* **2002**, *101-102*, 447.

[139] Woo, N. J.; Shaqfeh, E. S. G.; Khomami, B., *J. Rheol.* **2004**, *48*, 299.

[140] Randall, G. C.; Doyle, P. S., *Macromolecules* **2005**, *38*, 2410.

[141] Hagita, K.; Koseki, S.; Takano, K., *J. Phys. Soc. Japan* **1999**, *68*, 2144.

[142] Chen, Y.-L.; Graham, M. D.; de Pablo, J. J.; Randall, G. C.; Gupta, M.; Doyle, P. S., *Phys. Rev. E* **2004**, *70*, 060901(4).

[143] Usta, O. B.; Ladd, A.; Butler, J. E., *J. Chem. Phys.* **2005**, *122*, 094901.

[144] Balducci, A.; Mao, P.; Han, J.; Doyle, P. S., *Macromolecules* **2006**, *39*, 6273.

[145] Larson, R. G., *J. Rheol.* **2005**, *49*, 1.

[146] deGennes, P. G., *Macromol.* **1976**, *9*, 587.

[147] van Vliet, J. H.; Luyten, M. C.; ten Brinke, G., *Macromolecules* **1992**, *25*, 3802.

[148] deGennes, P. G., *Macromol.* **1976**, *9*, 594.

[149] Milchev, A.; Binder, K., *J. Phys. II France* **1996**, *6*, 21.

[150] Fang, L.; Hu, H.; Larson, R. G., *J. Rheol.* **2005**, *49*, 127.

[151] Adachi, K.; Kotaka, T., *Prog. Polym. Sci.* **1993**, *18*, 585.

[152] Wang, Y. C.; Stevens, A. L.; Han, J., *Anal. Chem.* **2005**, *77*, 4293.

[153] Doi, M.; Nakajima, H., *Chem. Phys.* **1974**, *6*, 124.

[154] Jendrejack, R. M.; Schwartz, D. C.; de Pablo, J. J.; Graham, M. D., *J. Chem. Phys.* **2004**, *120*, 2513.

[155] Hsieh, C.-C.; Balducci, A.; Doyle, P. S., *Macromolecules* **2007**, *40*, 5196.

[156] Shaqfeh, E. S. G., *J. Non-Newtonian Fluid Mech.* **2005**, *130*, 1.

[157] Perkins, T.; Quake, S.; Smith, D.; Chu, S., *Science* **1994**, *264*, 822.

[158] Y. Bohbot-Raviv *et al.*, *Phys. Rev. Lett.* **2004**, *92*, 098101(4).

[159] Dimitrakopoulos, P., *J. Fluid Mech.* **2004**, *513*, 265.

[160] P. S. Doyle *et al.*, *J. Non-Newtonian Fluid Mech.* **1998**, *76*, 79.

[161] Guo, L. J.; Cheng, X.; Chou, C. F., *Nano Letters* **2004**, *4*, 69.

[162] Mannion, J. T.; Reccius, C. H.; Cross, J. D.; Craighead, H. G., *Biophys. J.* **2006**, *90*, 4358.

[163] Zhang, C.; Zhang, F.; van Kan, J. A.; van der Maarel, J. R. C., *J. Chem. Phys.* **2008**, *128*, 225109.

[164] Lin, P. K.; Fu, C. C.; Chen, Y. L.; Chen, Y. R.; Wei, P. K.; Kuan, C. H.; Fann, W. S., *Phys. Rev. E* **2007**, *76*, 8.

[165] Krishnan, M.; Monch, I.; Scwille, P., *Nano Letters* **2007**, *7*, 1270.

[166] Balducci, A.; Hsieh, C.-C.; Doyle, P. S., *Phys. Rev. Lett.* **2007**, *99*, 238102.

[167] Hsieh, C.-C.; Doyle, P. S., *Korea-Australia Rheology Journal* **in press**.

[168] Tang, J.; Doyle, P. S., *App. Phys. Lett.* **2007**, *90*, 224103.

[169] Juang, Y.-J.; Wang, S.; Hu, X.; Lee, L. J., *Phys. Rev. Lett.* **2004**, *93*, 268105.

[170] Randall, G. C.; Doyle, P. S., *Proc. Nat. Acad. Sci. USA* **2005**, *102*, 10813.

[171] Steinburg, V., *Phys. Rev. Lett.* **submitted**.

[172] Chan, E. Y.; Goncalves, N. M.; Haeusler, R. A.; Hatch, A. J.; Larson, J. W.; Maletta, A. M.; Yantz, G. R.; Carstea, E. D.; Fuchs, M.; Wong, G. G.; Gullans, S. R.; Gilmanshin, R., *Gen. Res.* **2004**, *14*, 1137.

[173] Chun-Chen, Z.; Feng, J.; Qian-Qian, C.; Jing-Song, Y., *Polymer* **2008**, *49*, 809.

[174] Kim, J. M.; Doyle, P. S., *Macromolecules* **2007**, *40*, 9151.

[175] Mohan, A.; Doyle, P. S., *Phys. Rev. E* **2007**, *76*, 040903(R).

[176] Underhill, P. T.; Doyle, P. S., *Phys. Rev. E* **2007**, *76*, 011805.

[177] Randall, G. C.; Doyle, P. S., *Phys. Rev. Lett.* **2004**, *93*, 05812(4).

[178] Mohan, A.; Doyle, P. S., *Macromolecules* **2007**, *40*, 4301.

[179] Wong, P.; Lee, Y.-K.; Ho, C.-M., *J. Fluid Mech.* **2003**, *497*, 55.

[180] Lumley, J. L., *Phys. Fluids* **1977**, *20*, s64.

[181] Long, D.; amd A. Ajdari, J.-L. V., *Phys. Rev. Lett.* **1996**, *76*, 3858.

[182] Deutsch, J. M.; Madden, T. L., *J. Chem. Phys.* **1989**, *90*, 2476.

[183] Patel, P. D.; Shaqfeh, E. S. G., *J. Chem. Phys.* **2003**, *118*, 2941.

[184] Teclcmariam, N. P.; Beck, V. A.; Shaqfeh, E. S. G.; Muller, S. J., *Macromolecules* **2007**, *40*, 3848.

[185] Li, Y.; Tseng, Y. D.; Kwon, S. Y.; d'Espaux, L.; Bunch, J. S.; McEuen, P. L.; Luo, D., *Nat. Mater.* **2004**, *3*, 38.

[186] Murtsovkin, V. A., *Colloid Journal* **1996**, *58*, 341.

[187] Odijk, T., *arXiv:0802.2724v2 [cond-mat.soft]* **2008**.

[188] Texiera, R. E.; Dambal, A. K.; Richter, D. H.; Shaqfeh, E. S. G.; Chu, S., *Macromolecules* **2007**, *40*, 2461.

[189] Isambert, H.; Ajdari, A.; Viovy, J.-L.; Prost, J., *Phys. Rev. E* **1997**, *56*, 5688.

[190] Simonova, T. S.; Shilov, V. S.; Shramko, O. A., *Colloid Journal* **2001**, *63*, 108.

[191] Park, S. Y.; Russo, C. J.; Branton, D.; Stone, H. A., *J. Coll. Int. Sci.* **2006**, *297*, 832.

[192] Zhang, Y.; Gu, X.-J.; Barber, R. W.; Emerson, D. R., *J. Coll. Int. Sci.* **2004**, *275*, 670.

[193] Dendukuri, D.; Pregibon, D. C.; Collins, J.; Hatton, T. A.; Doyle, P. S., *Nat. Mater.* **2006**, *5*, 365.

[194] Dendukuri, D.; Gu, S. S.; Pregibon, D. C.; Hatton, T. A.; Doyle, P. S., *Lab Chip* **2007**, *7*, 818.